

DISSERTATION
SUBMITTED TO THE
COMBINED FACULTY OF
NATURAL SCIENCES AND MATHEMATICS
OF THE
RUPERTO-CAROLA-UNIVERSITY OF HEIDELBERG,
GERMANY
FOR THE DEGREE OF
DOCTOR OF NATURAL SCIENCES

PUT FORWARD BY

JOANNA DRAŹKOWSKA
BORN IN: LIDZBARK WARMIŃSKI, POLAND

ORAL EXAMINATION: 17 DECEMBER 2014

FROM DUST TO PLANETESIMALS

REFEREES:

PROF. DR. CORNELIS P. DULLEMOND

PROF. DR. MARIO TRIELOFF

To my husband

ZUSAMMENFASSUNG

Man weiß heute, dass jeder Stern der Milchstraße im Schnitt mindestens einen Planeten besitzt. Planetenentstehung scheint also unvermeidlich mit Sternentstehung einherzugehen. Es existieren jedoch einige Probleme, die es schwierig machen zu verstehen, wie aus dem primordialen, mikrometergroßen Staub, der in protoplanetaren Scheiben beobachtet wird, Planeten wachsen können. Eines dieser Probleme, welches das Thema dieser Dissertation ist, ist die Bildung von kilometergroßen Planetesimalen.

Wir entwickeln zuerst ein neues numerisches Code zur Evolution von Staub in protoplanetaren Scheiben, welches auf der Monte-Carlo-Methode basiert. Mit diesem Code modellieren wir verschiedene mögliche Szenarien zur Entstehung von Planetesimalen. Wir simulieren die Planetesimalentstehung sowohl durch Koagulation von Staub, als auch durch gravitativen Kollaps von dichten Klumpen, welche durch die Strömungsinstabilität gebildet wurden. Wir überprüfen welche Bedingungen notwendig sind, damit diese Szenarien ablaufen und vergleichen ihre Effizienz bei der Entstehung von Planetesimalen. Unsere Ergebnisse legen nahe, dass die Planetesimalentstehung durch Staub-Koagulation im inneren Teil der protoplanetaren Scheibe möglich ist, wohingegen die Strömungsinstabilität womöglich nur außerhalb der Eislinie effizient ist. Unsere Vorhersagen können dazu benutzt werden, die späten Phase der Planetenentstehung zu modellieren.

ABSTRACT

It is now clear that on average every star in the Milky Way has at least one planet. Planet formation seems to be an inevitable side effect of the star formation process. However, there are several problems that make it difficult to understand how the primordial micrometer dust grains observed in protoplanetary disks are turned to planets. One of them is the formation of kilometer-sized planetesimals, which is the topic of this dissertation.

We first develop a new code for dust evolution in protoplanetary disks, which is based on the Monte Carlo approach. The code is then used to model several possible planetesimal formation scenarios. We test planetesimal formation by both dust coagulation and gravitational collapse of dense pebble clumps formed by the streaming instability. We examine what conditions are necessary for these scenarios to proceed and compare their planetesimal formation efficiencies. Our results suggest that planetesimal formation via dust coagulation is possible in the inner part of the protoplanetary disk, whereas the streaming instability may only be efficient beyond the snow line. Our predictions can be used to model the late stages of planet formation.

PUBLICATIONS AND AUTHORSHIP

The work presented in this dissertation has previously appeared or will appear in the following publications:

Refereed publications:

- **J. Drażkowska**, F. Windmark & C. P. Dullemond, *Planetesimal formation via sweep-up growth at the inner edge of dead zones*, 2013, *A&A*, 556, A37
- **J. Drażkowska**, F. Windmark & C. P. Dullemond, *Modeling dust growth in protoplanetary disks: the breakthrough case*, 2014, *A&A*, 567, A38
- **J. Drażkowska** & C. P. Dullemond, *Can dust coagulation trigger the streaming instability?*, accepted for publication in *A&A*
- F. Windmark, S. Okuzumi & **J. Drażkowska**, *Local planetesimal formation and pile-up in the inner protoplanetary disk*, in prep.

Conference proceedings:

- **J. Drażkowska**, F. Windmark & C. P. Dullemond, *Sweep-up growth at the inner edge of dead zones*, poster presented at the Protostars & Planets VI held in Heidelberg, July 15-20, 2013
- **J. Drażkowska**, F. Windmark & S. Okuzumi, *Rapid planetesimal formation in the inner protoplanetary disk*, accepted for publication in Complex Planetary Systems, Proceedings of the International Astronomical Union, Volume 310, eds.: Z. Knezevic & A. Lemaître

The details of authorship are listed individually for each thesis chapter:

- Chapter 1: Everything was written by me and I made all the figures, except for Fig. 1.3, which is reproduced from [Cuzzi et al. \(2010\)](#) with suitable permission.
- Chapter 2: Everything was written by me and I made all the figures. I am the only author of the numerical code presented in the chapter.

- Chapter 3: Everything was written by me, but Fredrik Windmark contributed to the final form of the text significantly. All the figures were made by me. I came up with the presented planetesimal formation scenario and Fredrik Windmark provided the collision model used in the chapter and helped with its implementation.
- Chapter 4: Everything was written by me, but Fredrik Windmark contributed to the final form of the text. All the figures were made by me, but part of necessary data was provided by Fredrik Windmark, who performed runs with the Smoluchowski code. Section 4.6.3 is based on the concept developed by Satoshi Okuzumi and numerical models performed by Fredrik Windmark.
- Chapter 5: Everything was written by me and I made all the figures.

CONTENTS

1	Introduction	1
1.1	Extrasolar planets	2
1.2	The Solar System	6
1.3	Current planet formation theory	11
1.3.1	Protoplanetary disk structure	11
1.3.2	Dust evolution	13
1.3.3	Growth barriers	23
1.3.4	Planetesimal formation scenarios	26
1.3.5	Planetesimal evolution and planet formation	29
1.4	Numerical models of dust evolution	31
1.4.1	Solving the Smoluchowski equation	31
1.4.2	Monte Carlo methods	34
1.5	Overview of this dissertation	35
2	A new Monte Carlo code for dust evolution	37
2.1	Introduction	37
2.2	Code structure	38
2.2.1	Gas description	40
2.2.2	Dust description	40
2.2.3	Advection of dust particles	41
2.2.4	Collisions	45
2.2.5	Time step	47
2.3	Test cases	47
2.3.1	Tests of the coagulation model	49
2.3.2	Vertical settling and turbulent diffusion of the particles	49
2.3.3	Trapping of the dust particles in a pressure bump	51
2.3.4	Sedimentation driven coagulation	55
2.4	Summary	62

3	Planetesimal formation at the inner edge of dead zones	65
3.1	Introduction	65
3.2	Motivation	66
3.3	Simulation setup	68
3.3.1	Collision models	69
3.4	Results	70
3.4.1	Resolution study	76
3.5	Discussion and conclusions	77
4	Planetesimal formation triggered by the impact velocity distribution	81
4.1	Introduction	81
4.2	Motivation	82
4.3	The numerical models	83
4.4	Comparison of results obtained with both methods	85
4.5	Resolution dependence	88
4.5.1	Growth timescales	88
4.5.2	Breakthrough probability	91
4.6	Discussion	94
4.6.1	Coagulation codes	94
4.6.2	Planetesimal formation efficiency	97
4.6.3	Sweep-up growth in a global disk	99
4.7	Conclusions	102
5	Planetesimal formation via the streaming instability	105
5.1	Introduction	105
5.2	Motivation	107
5.3	Numerical methods	108
5.3.1	Dust evolution	108
5.3.2	Streaming instability	110
5.4	Preliminary estimates	114
5.5	Results	116
5.5.1	Fiducial run	117
5.5.2	Parameter study	121
5.5.3	Analytical model	125
5.6	Discussion	127
5.7	Conclusions	130
6	Summary	133

1

INTRODUCTION

As of October 2014, there are more than 1800 known exoplanets. Using a statistical analysis of the microlensing data, [Cassan et al. \(2012\)](#) showed that every star in the Milky Way is orbited by at least one planet, and similar result was obtained by [Youdin \(2011b\)](#) who analyzed the *Kepler* mission data. Planet formation is ubiquitous, but we lack convincing models of how the planets form. Even formation of the Solar System, which we are able to explore much better than any other planetary system, is not yet well explained.

Planet formation is undoubtedly a very complex process that covers many orders in magnitude in mass. It happens in disks surrounding young stars, called *protoplanetary disks*, where micron sized *monomers*, that are already present in the interstellar medium and enter the disk at the point of its formation, stick together to form ever larger *aggregates*. Many intermediate stages must happen before the thousands of kilometers sized planets are formed.

The process of turning dust to planets is most likely not very efficient. Although any primordial dust which was not used to form the planets, would be removed from the planetary system by processes such as the radiation pressure, we still observe some larger leftovers of the planet formation process: for example the asteroids in the Solar System. The craters seen on many of the Solar System bodies also prove that a great number of the intermediate sized objects did exist once upon a time. These bodies, which are too small to be called planets but large enough to be held together by self-gravity rather than material strength, are called *planetesimals* in the planet formation theory. This dissertation deals with the problem of planetesimal formation, which is hindered by so-called *growth barriers*.

In this chapter, we first introduce basic information about the known extrasolar planets (Sect. 1.1) and the Solar System (Sect. 1.2), which set constraints on the planet formation process. In Sect. 1.3, we review the current planet formation theory, focusing on its first stages, as they are the topic of this dissertation. In Sect. 1.4, we briefly introduce two dust coagulation modeling approaches, which are then used in subsequent chapters.

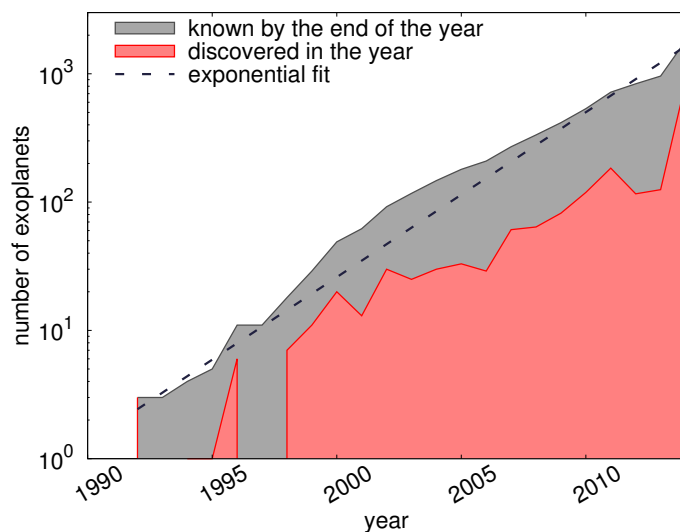


Figure 1.1: Number of exoplanets discovered in each year and known by the end of the year (in the case of 2014: until the 31st of July). The time dependence can be fitted by an exponential function (dashed line). Data to make this plot was obtained from the Open Exoplanet Catalogue (<http://www.openexoplanetcatalogue.com/>).

1.1 EXTRASOLAR PLANETS

A new era in the history of modern astrophysics started with the discovery of the first exoplanets by [Wolszczan & Frail \(1992\)](#). The number of known exoplanets increases roughly exponentially with time (Fig. 1.1). The discovery of a millionth exoplanet will be announced in the year 2036 if this rate is kept. In this section, we discuss the detection methods and basic properties of the currently known exoplanet population.

Figure 1.2 shows masses and semi-major axes of all the exoplanets known by the end of July 2014 as well as the eight planets of the Solar System. Masses are given in the units of Jupiter mass, M_J , and the distance is measured in astronomical units, where 1 AU is a mean distance between the Earth and the Sun. As can be seen, massive exoplanets close to their central stars are preferentially found. This is because of biases in the methods used to detect them.

It is exceedingly hard to directly image an exoplanet. This is because the planets are very faint sources that get drowned in the light emitted by their host stars. Only a few planets have been directly observed and these are mostly young, massive objects far away from their hosts ([Neuhäuser & Schmidt 2012](#)). Several indirect methods are however more successful in

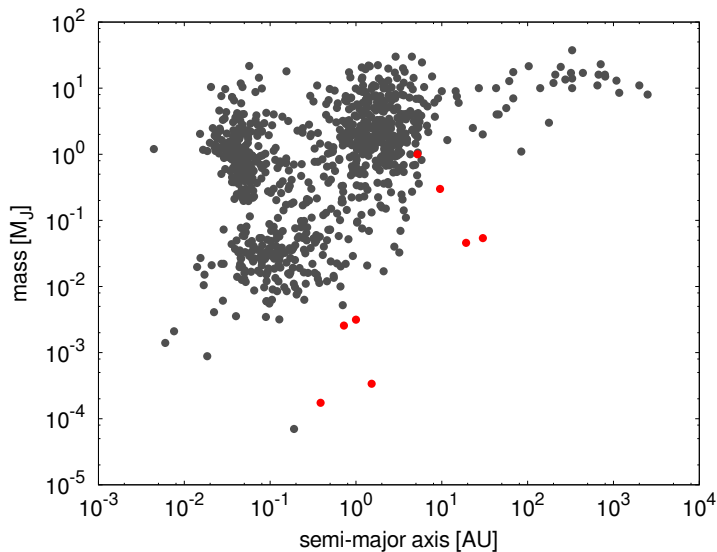


Figure 1.2: Exoplanets known by the 31st of July 2014 (grey dots) and planets of the Solar System (red dots). Due to observational biases, we are still not able to discover planets that are small and far away from their host stars. Data to make this plot was obtained from the Open Exoplanet Catalogue (<http://www.openexoplanetcatalogue.com/>).

detecting planets orbiting other stars.

The most fruitful exoplanet finding campaign until now is the *Kepler* mission. It has detected more than half of all the known exoplanets and there are still more than 3000 planet candidates found by this mission that await confirmation. The *Kepler* is a space observatory monitoring stars of the Milky Way. From May 2009 to May 2013, it observed a fixed field of view and constantly monitored the brightness of over 145000 main sequence stars. The light curves were then analyzed in search for periodic changes that could indicate presence of planets passing in front of the stars. The stars with light curves exhibiting such changes are then observed with large ground-based telescopes in order to confirm that the signal indeed comes from planets.

The method used by the *Kepler* mission is called transit photometry. Although it turned out to be an efficient way of detecting planets, the method has several disadvantages. A signal that is similar to the planetary transit can be produced by many astrophysical processes, such as starspots or unresolved binaries. Thus, this method suffers from a high rate of false-positives. Another disadvantage is that one needs to observe several transit events in order to confirm the existence of a planet. Thus, the star needs to be observed through many orbital periods of the planet. It is of course relatively

easy to detect the close-in planets, which have short orbital periods, but even finding a planet with a semi-major axis corresponding to the Earth requires several years of observations. Similar constraints apply to the size of planets: the larger the planet is, the stronger dip in the star's brightness it produces and thus the easier it is to find it. These two problems directly translate into the observational bias visible in Fig. 1.2: we cannot detect small planets that are far away from their host stars.

Another successful exoplanet detection method, called the radial velocity method or Doppler spectroscopy, suffers from similar limitations. The method is based on the Doppler effect: lines in the stellar spectrum have different wavelengths when the star moves with respect to the observer. Such a movement can be caused by the star and planet orbiting around the common center of gravity. The more massive the planet is, the stronger the effect. The main disadvantage of the radial velocity method is that it can only estimate a minimum mass of the planet. This is because the orientation of the planet orbit is unknown. Thus, many of the candidates found with this method may be in fact brown dwarfs: objects with masses above $\sim 13 M_J$, which are able to burn deuterium.

Early discoveries of the exoplanets brought a lot of surprise as they did not fit the planet formation theories, which were focused on the formation of the Solar System. The first discovered exoplanets orbited a millisecond pulsar: a quickly rotating neutron star that is an endpoint of massive star evolution. It is still a mystery how these planets got there: did they survive the violent supernova explosion, were they captured afterwards, or did they form in a secondary disk? Then, a massive planet (minimum mass of $\sim 0.5 M_J$) very close to its host star (semi-major axis of ~ 0.05 AU) was found (Mayor & Queloz 1995). This planet was the first hot Jupiter: massive planet orbiting surprisingly close to its host star and thus having a high surface temperature.

The hot Jupiters can not form in situ as the inner part of the protoplanetary disk does not have enough mass. To explain this, planet migration theory was developed. This is a relatively straightforward process but with an exact outcome that is very hard to predict. Due to the planet-disk interaction, a net torque is exerted on the planet and it migrates inwards in most cases, but an outward migration is also possible (Masset & Papaloizou 2003; Baruteau et al. 2013). Another possible scenario for the hot Jupiter formation is the gravitational planet-planet scattering followed by tidal orbit circularization (Naoz et al. 2011; Beugé & Nesvorný 2012). In other words: one of the planets in a multiple system is placed on a very eccentric orbit due to its gravitational interaction with the other planets. Its eccentricity is then reduced over time because of a complicated interaction with the host star, and the planet is fixed on a very close-in orbit. The fact that many of the

observed hot Jupiters are orbiting counter to the spin direction of the star (Triaud et al. 2010) is certainly in favour of the second scenario, because the planet-planet scattering does not only produce the high eccentricity but also a random inclination.

Another class of extrasolar planets are the super-Earths. These are planets of a few Earth masses orbiting inside of 1 AU. Their origin is still very much debated. They may, similarly as the hot Jupiters, be formed in the outer disk and then migrate inwards (Terquem & Papaloizou 2007; Rein 2012). However, the properties of some of the known multiple systems are not necessarily consistent with this scenario. The *Kepler* mission found many multiple exoplanet systems with three to five planets, all located inside of 0.5 AU, that possess very low mutual inclinations (Fang & Margot 2012). Of course, finding systems with such a low inclination scatter is a result of the observational bias: we could not detect all the planets with the transit method if they were not in the same orbital plane. These systems are called the multi-transiting systems with tightly-packed inner planets (STIPs). The inward migration scenario predicts that there should be mean-motion resonance chains in such systems (Goldreich 1965; Kley & Nelson 2012), but these are not observed as a general rule. Thus, the in situ formation scenario is feasible as an explanation of the STIPs formation (Lithwick & Wu 2012; Chiang & Laughlin 2013; Chatterjee & Tan 2014). We come back to this point in Chapter 4.

Besides the two most efficient indirect methods: the transit photometry and the Doppler spectroscopy, there are a few more in use. In particular, the first exoplanets were discovered using the so-called timing method. Existence of a planet causes variations in periodic phenomena such as the signal coming from the pulsar in the case of the planets discovered by Wolszczan & Frail (1992). Similar variations can be observed in the time or duration of the planetary transits (Nesvorný & Morbidelli 2008) or binary star eclipses (Lee et al. 2009). Another method is to search for variations in microlensing events introduced by a planet orbiting the lens star (Gaudi 2012; Giannini & Lunine 2013). This method is sensitive to Earth-mass planets up to 10 AU from the star. However, the lensing is a one-time event because the probability that such alignment occurs again is extremely low. Follow-up observations with other methods are not possible as the detected objects are typically very distant: some of them even in another galaxy (Ingrosso et al. 2009).

It is known that a significant fraction of stars reside in multiple star systems (Duquennoy & Mayor 1991; Lada 2006). Thus, it may not seem surprising that more than 40% of the exoplanet host stars may be in binary systems (Horch et al. 2014). Planets were discovered both around a single star of a binary (e.g. Haghighipour 2010) and the entire binary systems (e.g. Doyle et al. 2011; Welsh et al. 2012). Planet formation around one star in

a wide binary system is believed to proceed the same as around a single star, as properties of such planets are similar (Quintana et al. 2007; Desidera & Barbieri 2007). However, there are also planets around stars in tight binaries observed (e.g. Queloz et al. 2000; Correia et al. 2008; Zuckerman et al. 2008). There are several effects that make it hard to form planets in such systems. The lifetime of a protoplanetary disk in a binary system is shorter than around a single star (Cieza et al. 2009). This gives less time to accomplish the planet formation. Additionally, interaction with the host star companion exerts high impact speeds both on dust aggregates (Zsom et al. 2011b) and planetesimals (Th ebault et al. 2006). Thus, planet formation in such systems seems to be more complicated and challenging than around single stars, and we therefore focus on the latter (which is challenging enough) in this dissertation.

To sum up, we know that planets are ubiquitous: they are found around stars of all types. Even though our knowledge is limited by the observational biases, we already know that there are many architectures of planetary systems possible and that a significant fraction of them do not resemble our own Solar System. Regardless of how frequent our own system is, studying the Solar System is vital to understand more about the planet formation process.

1.2 THE SOLAR SYSTEM

The Solar System has eight planets: four small rocky bodies in the inner part and four gas giants in the outer part. Additionally, there are many smaller bodies: satellites of the planets, dwarf planets, asteroids, and comets. The Solar System is dynamically full, meaning that there are no more locations that would be stable for at least 10^9 years and that are not already occupied (Holman & Wisdom 1993). All of these bodies orbit around the Sun, which is classified as a G-type main-sequence star. The Sun contains more than 99% of all the Solar System mass. The second most massive body is Jupiter, which contains more than twice the mass of all the remaining bodies. Although the Sun is a dominant object considering the mass, it contains only 1% of the total angular momentum of the Solar System. This means that a substantial segregation of mass and angular momentum happened during the star and/or planet formation process.

The current architecture and properties of the Solar System gives us insights into its possible formation. Particularly, the dramatic difference between the inner and the outer planets hints towards a significant jump in the properties of the disk in which they formed. This jump is most likely connected with the temperature structure of the protoplanetary disk: the temperature should decrease with the distance from the star, as the inner

parts are naturally more exposed to the radiation coming from the central star (Weidenschilling 1977a). Thus, some chemical species may exist in the solid state in the outer disk and in the gas state in the inner disk. Hayashi (1981a) pointed out that for water, this transition region, or *snow line*, should be located at around 3 AU, dividing the inner and outer planets. They estimated that the surface density of solids should be around four times higher outside the snow line than in the inner region, where the solid water ice cannot exist. The enhanced abundance of solids in the outer disk would help to form the giant planet cores quickly, and thus allow them to accrete their massive atmospheres before the gas disk is dispersed.

The bodies of the Solar System, although they may seem distant, are still much closer to us than any other planetary system. There are many methods used for their exploration. For over 50 years, spacecrafts have been used to take photos and make measurements, and even return samples from the Moon but also from a comet, an asteroid and of the fine interplanetary dust. Cosmic material is also delivered to the Earth by meteorites, which are mostly fragments of the asteroids orbiting between Mars and Jupiter.

Dating of the material obtained from the outer space shows that the oldest objects in the Solar System are the calcium-aluminum-rich inclusions (CAIs) found in some meteorites. Their absolute age is currently determined with the lead isotopic dating to be 4567.30 ± 0.16 Myrs (Connelly et al. 2012). The CAIs are considered to be formed soon after the formation of the Sun.

Chondrules are another interesting feature found in most of the meteorites, called chondrites. These are mm-sized grains composed primarily of the silicate minerals: olivine and pyroxene (Jacquet 2014). Some of them were formed around the same time as the CAIs, but the chondrule formation lasted around 3 Myrs (Connelly et al. 2012). The formation process of the CAIs and chondrules is still debated. It is certain that there must have been some flash-heating event followed by relatively quick cooling of the material, because the chondrules show evidence of being molten and then cooled down and solidified within hours (Hewins et al. 2005; Alexander et al. 2008). This is because they contain a significant amount of volatile elements that would have been gone if the chondrules had been molten for any longer time. Such heating might have been caused by large-scale shocks (Desch & Connolly 2002; Ciesla & Hood 2002; Boss & Durisen 2005), bow shocks caused by eccentric planetary embryos (Hood 1998; Morris et al. 2012), nebular lightnings (Pilipp et al. 1998; Güttler et al. 2008), and high impact speed planetesimal collisions (Yamamoto et al. 1991; Dullemond et al. 2014). However, each of these scenarios has severe problems and we cannot consider the chondrule formation to be explained yet (see e.g. Alexander et al. 2008; Stammer & Dullemond 2014). The sizes and composition of chondrules are also intriguing.

ing: there are chondrules of different ages but only one size found in one meteorite (Kuebler et al. 1999; Mostefaoui et al. 2002). These facts suggest that there was some size-sorting mechanism operating in the solar nebula and that the parent bodies of the meteorites were formed only after all the chondrules were present (Cuzzi et al. 2010). The existence of chondrules and CAIs proves that the coagulation of the primordial micron-sized dust grains had to proceed to at least cm-sized aggregates. However, the structure of meteorites, which consist not only of the chondrules, but also of smaller dust grains, suggests that the coagulation process resulted in a quite wide size distribution. It is worth to mention that there are also meteorites, called achondrites, that do not include any chondrules.

Thanks to the chondrules in meteorites, we know that most of their parent bodies, asteroids, consist of relatively primordial matter (Binzel et al. 2002). This is important, as it is known that asteroids larger than a few kilometers would be melted and differentiated due to the radiogenic heating by short-lived nuclides, mainly ^{26}Al , if they formed early when the abundances were still high (Gail et al. 2013). Thus, most of the planetesimals must have formed significantly later than the CAIs and chondrules.

As mentioned earlier in this section, most of the meteorites originate from the asteroid belt located between Mars and Jupiter. The collision timescale of the present-day asteroid belt is very long. Thus, the observed size distribution can be treated as a relic of the primordial one (Bottke et al. 2005). Fig. 1.3 presents the size distribution observed by different instruments in the asteroid belt as summarized by Cuzzi et al. (2010). It exhibits a pronounced peak at ~ 140 km. This size distribution of the asteroids is commonly interpreted as an evidence for existence of one typical size of ~ 100 km of the primordial planetesimals. Planet formation via gravitational collapse of dense dust clumps is therefore often favored, as it would consistently lead to such a characteristic size (Morbidelli et al. 2009; Cuzzi et al. 2010), but the possibility of forming the size distribution via subsequent coagulation cannot be excluded (Weidenschilling 2011; Lithwick 2014).

The dynamical state of the asteroid belt suggests that it was significantly depleted in mass, presumably during the migration of Jupiter (Morbidelli et al. 2010). The depletion of the asteroid belt and, more generally, the early dynamical evolution of the Solar System planets, are connected to the interesting issue of the water on the Earth origin. As mentioned previously, the water ice could not exist in the solar nebula at the present location of the Earth. The icy comets have been initially suggested as the most likely source of the Earth's water (see e.g. Delsemme 1991). However, the isotopic constraints, namely the ratio between deuterium (heavy hydrogen, ^2H) and the "normal" hydrogen measured for the Earth and, mainly by the spectro-

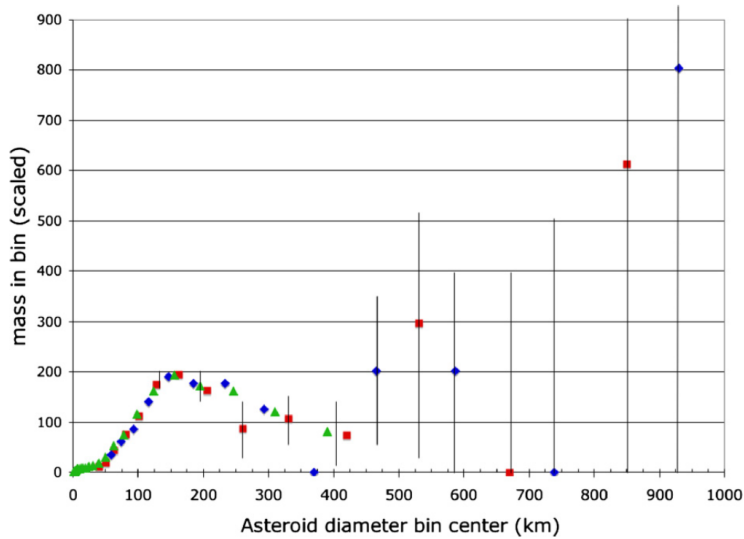


Figure 1.3: The current size distribution of the asteroid belt as observed by different instruments. Reprinted from *Icarus*, Vol. 208, No. 2, Cuzzi et al., "Towards initial mass functions for asteroids and Kuiper Belt Objects", Pages No. 518-538, Copyright 2010, with permission from Elsevier.

scopic observations, for comets, contradict this hypothesis (Dauphas et al. 2000; Albertsson et al. 2014). It is now commonly accepted that these were rather water-rich asteroids scattered by migrating Jupiter that delivered the water (Izidoro et al. 2013; O'Brien et al. 2014).

The delivery of water can be related to a dramatic event in the early history of the Solar System known as the Late Heavy Bombardment. From the data obtained by the lunar missions, it seems that there was a period between 4.1 to 3.8 Gyrs ago when the Moon was intensively bombarded by asteroids (Tera et al. 1973). This is interesting, because explaining the Late Heavy Bombardment helps us to understand more about the Solar Systems conditions at the time when it occurred. The reason for this bombardment was most likely dynamics of the giant planets, which caused perturbations of the orbits of the surrounding smaller bodies, causing some of them to get thrown into the inner Solar System (Wetherill 1975; Levison et al. 2001). One of the most widely accepted scenarios to explain this is the Nice model, which predicts that the giant planets were initially much more packed and on resonant orbits. A violent gravitational instability led to the current orbits, destabilizing the asteroids at the same time (Gomes et al. 2005; Tsiganis et al. 2005; Levison et al. 2011).

The giant planets instability presumably scattered the small bodies not

only inwards but also outwards, delivering some objects to the Kuiper belt, which extends from the orbit of Neptune (30 AU) to approximately 50 AU from the Sun, and the Oort cloud, which surrounds the Sun up to 50000 AU. The Kuiper Belt is known to consist of two different populations (Tegler & Romanishin 1998, 2003). One of the populations is dynamically excited with surface colors suggesting that it was formed in the vicinity of Jupiter. These are the objects that were presumably scattered by the giant planets. The other population is dynamically cold and has surface albedos suggesting that it is made out of ice (Brucker et al. 2009). These are most likely the objects that were formed in situ. Their size distribution is similar to the one of the asteroid belt and analogically, both the formation via gravitational collapse (Cuzzi et al. 2010; Johansen et al. 2012), and coagulation (Schlichting & Sari 2011; Schlichting et al. 2013) are considered.

The Kuiper Belt is a source of short-period comets that visit the inner Solar System from time to time (Schlichting et al. 2012). One of them is the comet 81P/Wild that was a target of the *Stardust* mission, which collected dust samples from the coma of the comet and returned them to the Earth. A big surprise was that chondrules and CAIs were found, which are thought to be formed in the inner Solar System (Flynn 2008; Matzel et al. 2010). The comet turned out to be covered in impact craters and very active, with numerous water vapour jets (Brownlee et al. 2004). The *Stardust* was a fly-by mission, able to observe only the comet's surface. Another mission, the *Deep Impact*, released an impactor into the comet 9P/Tempel that collided with its nucleus. The comet turned out to be more dusty, porous and of lower tensile strength than expected (A'Hearn et al. 2005; Richardson et al. 2007; A'Hearn 2008). Most recently, the mission *Rosetta* has approached the comet 67P/Churyumov-Gerasimenko. The first pictures of the comet revealed that it consists of two distinct parts: it may be even a contact binary. The properties revealed by the space missions revised our view of comets. The low tensile strength of these objects suggests that they have been formed by gravitational instability (Skorov & Blum 2012).

These are only some of the facts about the Solar System that are useful in constraining the planet formation process. We come back to some of these points in the following chapters. In Chapter 3, we investigate significance of the snow line for the planet formation process. In Chapter 4, we present a planetesimal formation scenario that can explain the low mass of Mars. In Chapter 5, we show that planetesimal formation via gravitational collapse of dense dust clumps formed by the streaming instability preferentially works in the outer part of the disk, which is consistent with the observed properties of comets.

1.3 CURRENT PLANET FORMATION THEORY

1.3.1 PROTOPLANETARY DISK STRUCTURE

Planets form in disks surrounding young stars. The protoplanetary disks are observed mainly at infrared to millimeter wavelengths. Some basic properties, such as their sizes and masses, can be constrained using these observations. Thanks to the measurements of disks occurrence rate around stars of different ages, we know that a typical lifetime of a disk around a solar-mass star is on the order of 10^6 yrs (Hernández et al. 2007; Wyatt 2008). It is shorter for more massive stars (Williams & Cieza 2011). The average mass of the disk is estimated to be 1% of mass of the central star (Andrews & Williams 2007a), however, as we discuss in Chapter 6, this may be underestimated. It is generally assumed that the initial dust-to-gas ratio in the disk is the same as measured in the interstellar medium: on the order of 1% (Ferrière 2001). The main issue of the current protoplanetary disk observations is that they are not able to look into the inner region of the disks: only the regions outside of ~ 20 AU can be resolved with the current instruments (Williams & Cieza 2011). Thus, the structure of the inner regions, where the terrestrial planets of the Solar System exist and the exoplanets are detected, is not well constrained.

In the planet formation models, we typically use analytical disk models. One of the most known is called the *Minimum Mass Solar Nebula* (MMSN). From the current mass distribution in the Solar System, Weidenschilling (1977b) and Hayashi (1981a) reconstructed the radial profile of the primordial solar nebula that would be just massive enough to allow the assembly of the planets. The vertically integrated gas density in this model follows

$$\Sigma_{\text{g}} = 1700 \times \left(\frac{r}{\text{AU}} \right)^{-1.5} \text{ g cm}^{-2}, \quad (1.1)$$

where r is the radial distance from the central star. This model was later updated, taking into account that the giant planets might have been initially more compact, as is suggested by the Nice model described in the previous section. Taking this into account, Desch (2007) obtained a much steeper gas surface density profile

$$\Sigma_{\text{g}} = 50500 \times \left(\frac{r}{\text{AU}} \right)^{-2.168} \text{ g cm}^{-2}. \quad (1.2)$$

However, the observed disks appear to have more flat surface density profiles (Andrews & Williams 2007b), at least in the outer regions. Brauer et al. (2008a) therefore used yet another disk model with the surface density of

$$\Sigma_{\text{g}} = 20 \times \left(\frac{r}{\text{AU}} \right)^{-0.8} \text{ g cm}^{-2}. \quad (1.3)$$

1.3. CURRENT PLANET FORMATION THEORY

The mass of this disk

$$M_{\text{disk}} = 2\pi \int_{r_{\text{in}}}^{r_{\text{out}}} \Sigma_{\text{g}}(r)r \, dr, \quad (1.4)$$

integrated between $r_{\text{in}} = 0.1$ AU and $r_{\text{out}} = 100$ AU is on the order of 1% of the solar mass, the same as in the MMSN model, but the disk profile is much shallower, with significantly less mass in the inner region.

Assuming that the disk is in vertical hydrostatic equilibrium, resulting from a balance between the vertical component of star gravity and the gas pressure (the gravity from the disk can be neglected if we assume a low-mass disk, i.e. $M_{\text{disk}} \ll M_{\star}$), we can derive the vertical density structure

$$\rho_{\text{g}} = \rho_{\text{g}}^{z=0} \exp\left(\frac{-z^2}{2H_{\text{g}}^2}\right), \quad (1.5)$$

where $\rho_{\text{g}}^{z=0}$ is the gas density in the midplane, which can be computed as

$$\rho_{\text{g}}^{z=0} = \frac{\Sigma_{\text{g}}}{\sqrt{2\pi}H_{\text{g}}}, \quad (1.6)$$

and H_{g} is the pressure scale height of gas. The vertical scale height of gas is given by

$$H_{\text{g}} = \frac{c_{\text{s}}}{\Omega_{\text{K}}}, \quad (1.7)$$

where c_{s} is the sound speed in the gas and

$$\Omega_{\text{K}} = \sqrt{\frac{GM_{\star}}{r^3}} \quad (1.8)$$

is the orbital frequency. G is the gravitational constant and M_{\star} is mass of the central star. The sound speed is related to the temperature

$$c_{\text{s}} = \sqrt{\frac{k_{\text{B}}T}{m_{\text{g}}}}, \quad (1.9)$$

where k_{B} is the Boltzmann constant and m_{g} is mass of the gas molecule, which we take to be $m_{\text{g}} = 2.3 \times m_{\text{p}}$.

The shape of the disk, i.e. the H_{g}/r ratio, is dependent on the temperature structure of the disk. Deriving the thermal disk structure is a complicated task. In the models presented in this dissertation, we assume that the disk is isothermal, meaning that the temperature is only dependent on the distance

from the star, which is a significant simplification, because in reality the temperature changes with the height above the midplane. [Kenyon & Hartmann \(1987\)](#) found that a flaring disk geometry, meaning that the vertical height of the disk increases rapidly with the distance from the star, is needed to explain the spectral energy distribution observed in the protoplanetary disks. A consistent temperature profile, which we use in our models, is

$$T \propto r^{-1/2}. \quad (1.10)$$

Although the real disks are evolving and finally dissipate on a few Myrs timescale, in our models we assume steady state disks. This is because the timescale of planetesimal formation, which we are interested in, is much shorter than 10^6 yrs. The radial force balance in such disk includes contributions from centrifugal force, gravity, and radial pressure gradient:

$$\frac{v_{\phi,g}^2}{r} = \frac{GM_\star}{r^2} + \frac{1}{\rho_g} \frac{dP_g}{dr}, \quad (1.11)$$

where $v_{\phi,g}$ is the orbital speed of the gas and $P_g = \rho_g c_s^2$ is the pressure. The difference between the gas speed $v_{\phi,g}$ and the Keplerian speed v_K can be parametrized with η , such that

$$v_{\phi,g} = v_K \sqrt{1 + 2\eta}, \quad (1.12)$$

with

$$\eta = \frac{1}{2\rho_g r \Omega_K^2} \frac{dP_g}{dr}. \quad (1.13)$$

The pressure gradient is negative, thus $\eta < 0$ and the gas rotates with a sub-Keplerian speed. As visible in [Fig. 1.4](#), the difference between the gas and Keplerian rotation is typically on the order of $10^{-3} - 10^{-2} \times v_K$, and it increases with the distance from the star. This tiny difference becomes very important for the motion of solids.

1.3.2 DUST EVOLUTION

The evolution of solids in a protoplanetary disk is driven by their interaction with gas. Velocities of dust grains are important to determine how often the grains collide, and therefore how quickly they grow, and also to determine what happens to two grains when they collide. As shown in the previous section, the gas disk is pressure supported and thus rotates with a slightly sub-Keplerian speed. The difference between the gas rotation and the Keplerian rotation is very small, but it influences the dust evolution significantly. The gas disk may also be turbulent, which causes diffusion of dust and adds a random velocity component, enhancing the collision speeds further. A sketch of effects we include in our dust evolution models is presented in [Fig. 1.5](#).

1.3. CURRENT PLANET FORMATION THEORY

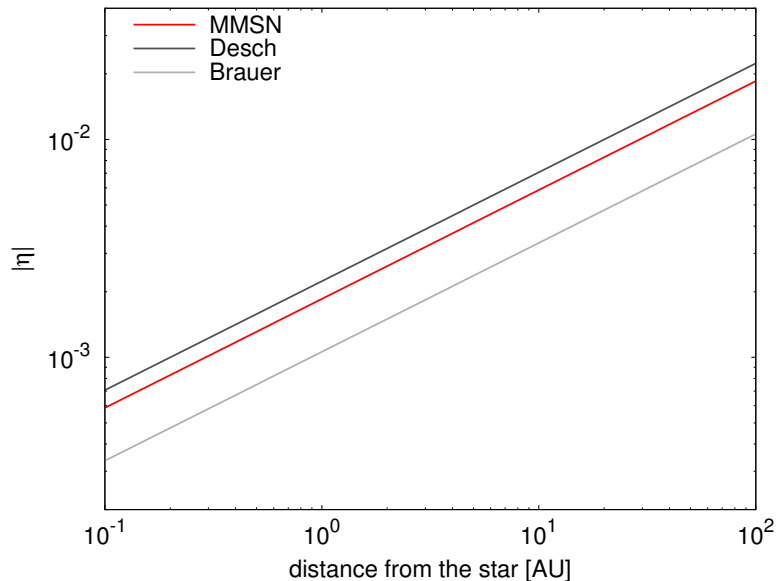


Figure 1.4: The value of the parameter η (Eq. 1.13) describing the difference between the gas and Keplerian rotation in three different disk models described with Eqs. (1.1) – (1.3).

STOKES NUMBER

The interaction between the dust and gas can be parametrized with the *Stokes number*

$$\text{St} = t_s \Omega_K, \quad (1.14)$$

where t_s is stopping time of the particle and Ω_K is the orbital frequency. The stopping time of a particle corresponds to the time in which the particle adjusts its velocity to the velocity of surrounding gas. The stopping time is on the order of seconds for tiny μm -sized monomers and gets longer for larger aggregates. The small aggregates have $\text{St} \ll 1$ and are tightly coupled to the gas, meaning that they basically follow the gas movement. On the other hand, bodies with $\text{St} \gg 1$ are decoupled from the gas and move on Keplerian orbits. Bodies corresponding to $\text{St} \approx 1$ are called *pebbles*, and are influenced by the interaction with gas the most: they acquire the highest drift and impact speeds.

There are two drag regimes determining the aggregate motion: the Epstein (Epstein 1924) and the Stokes (Whipple 1972) regime. The Epstein regime applies to small grains, when their size is smaller than the mean free path in

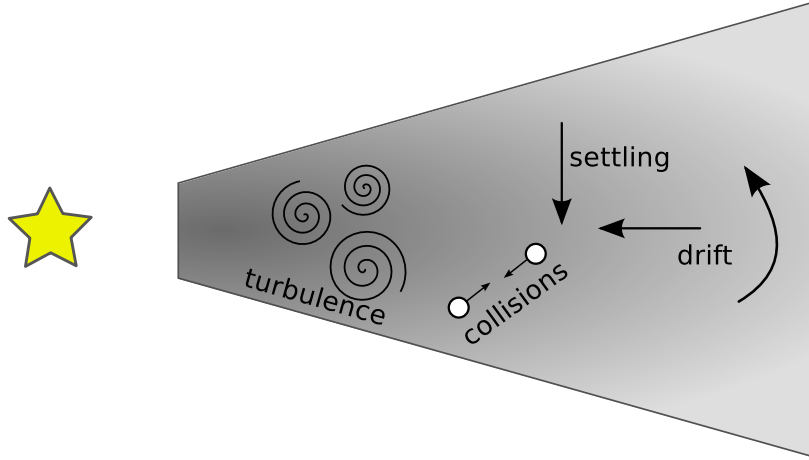


Figure 1.5: Pictographic representation of the processes we include in the dust evolution models presented in this dissertation. All of them are caused by the interaction between dust and gas.

the gas. The mean free path is defined as

$$\lambda_{\text{mfp}} = \frac{m_g}{\rho_g \sigma_g}, \quad (1.15)$$

where ρ_g is gas density, m_g is mass of the gas molecule, and σ_g is cross section for collisions between the gas molecules. For particles with radii $a < \frac{9}{4} \lambda_{\text{mfp}}$, the stopping time can be calculated as (Weidenschilling 1977a)

$$t_s^{\text{Ep}} = \frac{a \rho_p}{v_{\text{th}} \rho_g}, \quad (1.16)$$

where ρ_p is the internal density of the particle and $v_{\text{th}} = \sqrt{8/\pi} \times c_s$ is the thermal velocity of the gas. This can be rewritten as

$$t_s^{\text{Ep}} = \frac{\pi}{2} \frac{a \rho_p}{\Sigma_g \Omega_K}, \quad (1.17)$$

and thus the Stokes number in the Epstein regime is

$$\text{St}^{\text{Ep}} = \frac{\pi}{2} \frac{a \rho_p}{\Sigma_g}. \quad (1.18)$$

As can be seen in the above equations, the aerodynamics of a grain is in principle determined by the product of the radius a and internal density ρ_p . Thus, a small but dense grain follow the same behavior as a larger but porous grain as long as radii of both of them are smaller than $\frac{9}{4} \lambda_{\text{mfp}}$, meaning that both the grains are in the Epstein drag regime.

1.3. CURRENT PLANET FORMATION THEORY

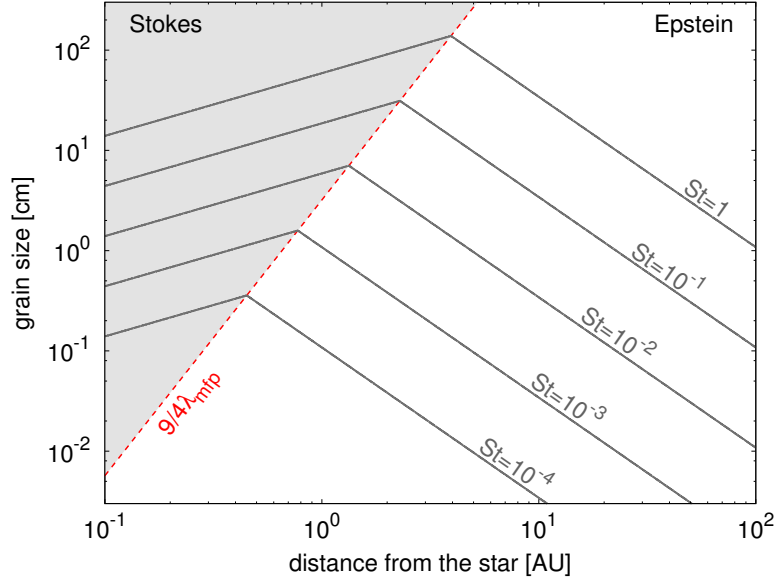


Figure 1.6: Dust grain sizes corresponding to the given Stokes number parameter values (grey lines) in the MMSN disk model. We assume internal density of grains of $\rho_p = 1 \text{ g cm}^{-3}$. The red dashed line corresponds to the size of $\frac{9}{4}\lambda_{mfp}$, where the drag regime changes from Epstein (outer disk) to Stokes (inner disk, shaded region).

Grains with $a > \frac{9}{4}\lambda_{mfp}$ are in the Stokes regime. The Stokes regime consists of three sub-regimes that are distinguished by the Reynolds number defined as

$$Re = \frac{2a\Delta v_{pg}}{\nu_{mol}}, \quad (1.19)$$

where Δv_{pg} is the relative velocity between the gas and particle and $\nu_{mol} = v_{th}\lambda_{mfp}/2$ is molecular viscosity of the gas. The stopping time in the three regimes is

$$t_s^{St} = \begin{cases} \frac{2a^2\rho_p}{9\nu_{mol}\rho_g} & \text{for } Re < 1 \\ \frac{2^{0.6}a^{1.6}\rho_p}{9\nu_{mol}^{0.6}\Delta v_{pg}^{0.4}\rho_g^{1.4}} & \text{for } 1 < Re < 800 \\ \frac{6a\rho_p}{\Delta v_{pg}\rho_g} & \text{for } Re > 800 \end{cases} \cdot \quad (1.20)$$

The Stokes number in the Stokes regime can be computed by multiplying the t_s by the orbital frequency Ω_K (Eq. 1.14). The dependence on particle

radius changes in each of the regimes.

Figure 1.6 presents the dependence of dust grain size corresponding to the given Stokes number on the distance from the central star in the MMSN disk model. The transition from Epstein to Stokes drag regime that happens when a dust grain is drifting inwards in the disk can have interesting consequences for dust evolution, as described in Chapter 4.

It is worth noting that the above formulas were derived for compact spherical grains and not much research has been made to test how important these assumptions are. Porous, irregular aggregates, which are expected to exist in the protoplanetary disk as an outcome of dust coagulation, certainly have different aerodynamic properties than the spherical grain (Meakin & Donn 1988; Nakamura & Hidaka 1998). Thus, it may be useful to build more advanced drag formulas taking into account the shape or internal structure of aggregates.

DRIFT

Due to the aerodynamic interaction with the sub-Keplerian gas, the dust grains lose their angular momentum and drift toward the star. The velocity of the radial drift is computed as (Weidenschilling 1977a)

$$v_{r,d} = \frac{2\eta v_K}{St + St^{-1}}, \quad (1.21)$$

where η is describing the difference between the gas and Keplerian rotation (Eq. 1.13). The usual $\eta < 0$ means inward drift. The drift speed $|v_{r,d}|$ reaches the maximum value for pebbles with $St = 1$, and in the MMSN disk is as high as 55 m s^{-1} .

The interaction with the gas leads to the grains acquiring orbital speeds different from Keplerian. These are also regulated by the pressure gradient and the Stokes number:

$$v_{\phi,d} = \frac{\eta v_K}{1 + St^2}. \quad (1.22)$$

The dust particles present in the protoplanetary disk are settling towards the midplane due to the interplay between gravity from the central star and the centrifugal force. The settling velocity is regulated by the gas drag. Results obtained by Carballido et al. (2011) suggest the settling velocity of

$$v_{z,d} = -z\Omega_K \frac{St}{1 + St^2}. \quad (1.23)$$

This formula includes the orbital oscillations of grains with $St > 1$, where the stopping times are too long for the grains to get stopped in the midplane.

1.3. CURRENT PLANET FORMATION THEORY

Equations (1.21) – (1.22) were derived with an assumption that the dust density is much lower than the gas density ($\rho_d \ll \rho_g$). However, it is known that the drift speeds are modified if the dust density is enhanced such that $\rho_d \gtrsim \rho_g$ (Nakagawa et al. 1986). It was recently found that, in the case of strong dust-to-gas ratio enhancement, the drift speeds are becoming dependent on the size distribution in a complicated way and even an outward drift is possible for the smallest aggregates (Bai & Stone 2010a; Laibe & Price 2014).

As all the systematic drift speeds depend on the Stokes number and thus on the size of particles, the particles of different sizes acquire relative velocities that drive their collisions. However, the drift described with Eqs. (1.21) – (1.23) are not the only sources of the impact speeds. A significant contribution is also made by the turbulence.

TURBULENCE

The dissipation of protoplanetary disk is usually explained by accretion of gas onto the central star. In order to enable the accretion, the disk have to transport the angular momentum outwards, and from the angular momentum distribution in the Solar System we know that such transport indeed happens (Sect. 1.2). Thus, some source of viscosity is needed. The molecular viscosity is not sufficient to cause the disk accretion on the observed timescale of a few Myrs. The magnetorotational instability (MRI) was proposed as a source of turbulence that could cause a significant viscosity (Balbus & Hawley 1991).

The turbulent viscosity is usually parametrized with the α parameter (Shakura & Sunyaev 1973), such that

$$\nu = \alpha c_s H_g. \quad (1.24)$$

The α parameter describes the strength of the turbulence. In case of the MRI turbulence, this parameter has values of $10^{-6} < \alpha < 10^{-2}$. The turbulence is usually assumed to follow the Kolmogorov prescription (Kolmogorov 1941). It is a cascade model in which the energy flows from the largest eddies (corresponding to the typical length of $\sqrt{\alpha} H_g$) to ever smaller eddies, down to so-called Kolmogorov length scale, where the energy is thermally dissipated.

The turbulent motions of gas influence the dynamics of dust grains. The turbulent diffusion does not allow the dust particles to form an infinitely thin midplane layer and the balance between the settling and diffusion leads to the following scale height of dust:

$$H_d = H_g \sqrt{\frac{\alpha}{\alpha + \text{St}}}. \quad (1.25)$$

CHAPTER 1. INTRODUCTION

Small particles with $St < 1$ stay well mixed with the gas, whereas the pebbles settle down quite efficiently: in a disk of solar metallicity with grains of $St > 10^{-2}$ and with $\alpha < 10^{-4}$, the dust-to-gas ratio in the midplane exceeds unity.

The contribution of turbulence to the impact speeds of the grains is constantly investigated. Assuming the Kolmogorov turbulence, [Ormel & Cuzzi \(2007\)](#) derived expressions for the impact velocities induced by turbulence that we use in our models. The impact speeds are also investigated by direct numerical simulations ([Pan & Padoan 2013](#); [Pan et al. 2014a,b](#)), which found a general agreement of their results with the [Ormel & Cuzzi \(2007\)](#) formulas, however suggested that they may overestimate the true values by a factor of a few.

Most of the dust evolution models include turbulence as an inevitable process that happens in the disk. However, it was postulated that disks may include substantial parts that are free from the MRI: these are called *dead zones* ([Ostriker & Shu 1995](#)). The MRI turbulence requires the gas to be sufficiently ionized, which may be not possible if small dust grains are present ([Okuzumi & Hirose 2012](#); [Dzyurkevich et al. 2013](#)). Recent research, that include even more advanced magnetohydrodynamics models, leads to the conclusion that the magnetic stresses caused by so-called Hall effect can transport the angular momentum without inducing turbulence ([Lesur et al. 2014](#); [Bai 2014](#)): it may be that disks are entirely "dead".

COLLISIONS

The relative velocities of dust grains drive their mutual collisions. The collision rate, i.e. the number of collisions per second that a single particle undergoes, is

$$\mathcal{R} = N_d \Delta v \sigma, \quad (1.26)$$

where N_d is number density of dust particles, Δv is the impact speed, and σ is the cross section for collision between the colliding particles: $\sigma = \pi (a_1 + a_2)^2$, where a_1 and a_2 are the particles' radii.

The impact speed Δv depends on the disk properties and the colliding grain sizes. [Fig. 1.7](#) shows typical impact speeds for grains of different sizes calculated for a MMSN disk with turbulence of $\alpha = 10^{-3}$ at 1 AU from the central star. The collisions between smallest grains are driven mainly by the Brownian motion. The corresponding velocity can be calculated as

$$\Delta v_B = \sqrt{\frac{8k_B T (m_1 + m_2)}{\pi m_1 m_2}}, \quad (1.27)$$

where m_1 and m_2 are masses of the colliding particles. As visible in [Fig. 1.7](#),

1.3. CURRENT PLANET FORMATION THEORY

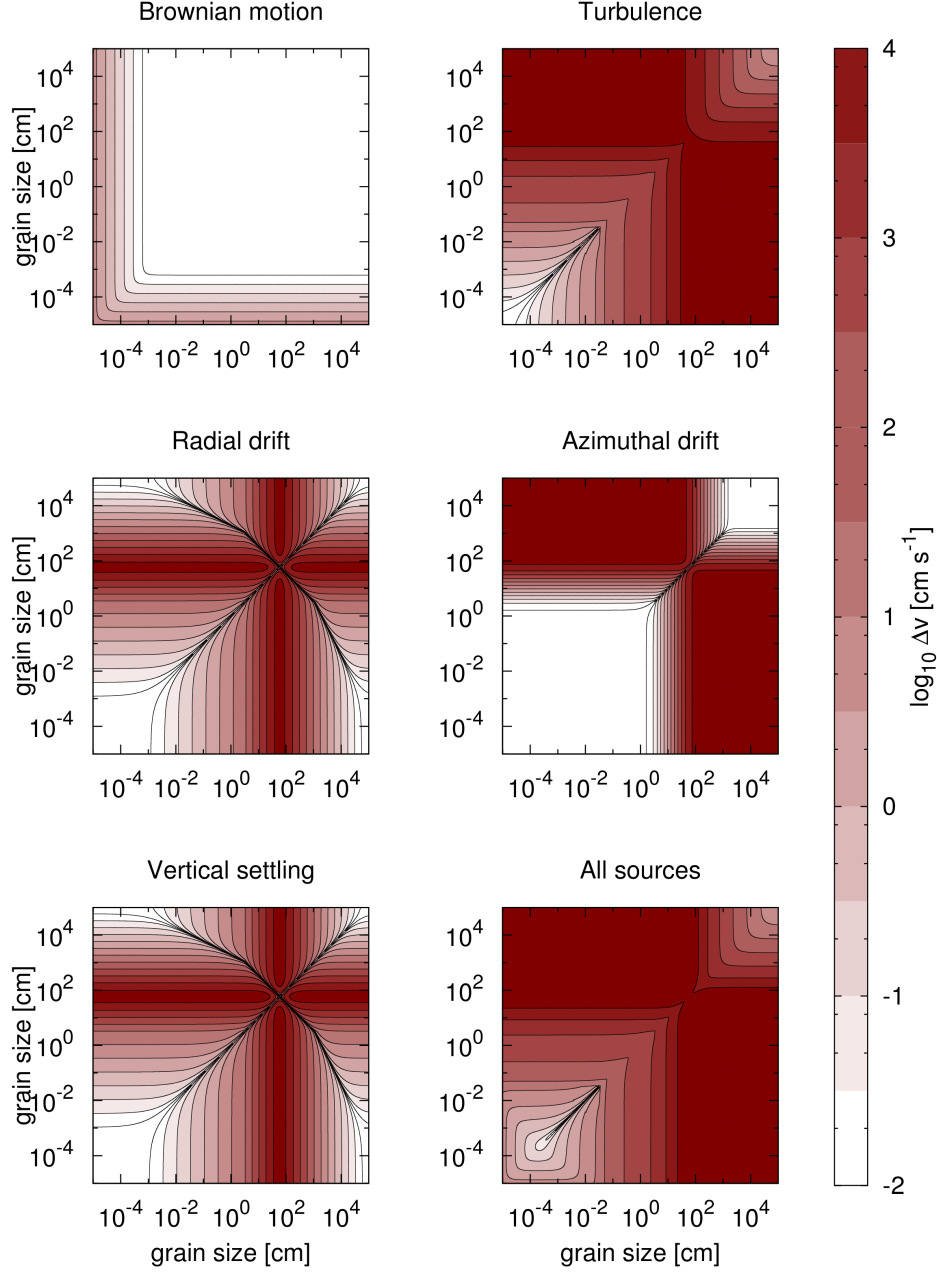


Figure 1.7: Impact speeds between grains of different sizes calculated for the different sources and summed up in the last panel. The speeds were calculated for a MMSN disk with turbulence of $\alpha = 10^{-3}$ at 1 AU from the central star. The grain size corresponding to $St = 1$ in this model is around 70 cm and this is where the the impact speeds are the highest.

the Brownian motion is only important for the smallest aggregates and quickly decreases with the grain size.

The turbulent velocities plotted in Fig. 1.7 were calculated from the closed-form expressions derived by Ormel & Cuzzi (2007), which we also use in our models. Ormel & Cuzzi (2007) found three regimes of the relative velocities coming from turbulence. In the first regime, which corresponds to the small grains, the impact speeds are proportional to the difference in the Stokes number of particles, and thus the relative velocity between the equal-sized particles vanishes. However, in the second regime, corresponding to slightly larger grains, the impact speeds are proportional to the square-root of the Stokes number of the larger particle:

$$\Delta v_T = \sqrt{2\alpha St} \times c_s. \quad (1.28)$$

Thus, even the equal-sized particles acquire high impact speeds, on the order of 100 m s^{-1} . The second regime is the most interesting in planetesimal formation context. In the third regime, for the largest grains, the turbulent velocities decrease again.

The systematic radial and azimuthal drift, and the vertical settling also contribute to the impact speeds. The contributions are calculated using the Eqs. (1.21) – (1.23). For example, for the radial drift

$$\Delta v_r = |v_{r,1} - v_{r,2}|, \quad (1.29)$$

where $v_{r,1}$ and $v_{r,2}$ are the radial drift speeds for each of the colliding particles calculated from the Eq. (1.21). Contributions from the azimuthal drift Δv_ϕ and vertical settling Δv_z are calculated analogically.

Finally, the total impact speed is calculated as

$$\Delta v = \sqrt{\Delta v_B^2 + \Delta v_T^2 + \Delta v_r^2 + \Delta v_\phi^2 + \Delta v_z^2}, \quad (1.30)$$

corresponding to a vector sum of all the contributions.

The outcome of a collision between two grains is a complex issue that is extremely difficult to predict analytically, and is therefore subject to laboratory research. A recent review of the experiments done on this problem is given by Güttler et al. (2010). The collision outcome was proven to depend on many parameters, such as: the impact speed, masses of the colliding particles, their composition and internal structure, and the impact angle. Güttler et al. (2010) divided the collision outcomes observed in the experiments into nine groups. Implementing that collision model into a dust evolution code, Zsom et al. (2010) found that the growth is halted by bouncing collisions. In order to perform robust numerical models of dust coagulation in this dissertation,

1.3. CURRENT PLANET FORMATION THEORY

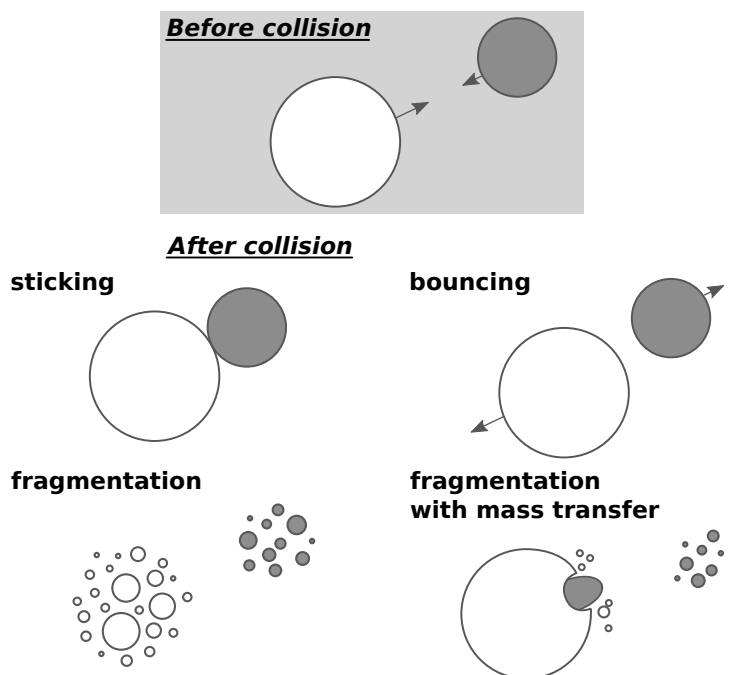


Figure 1.8: Sketch of the four possible collision outcomes included in our simplified models. The sticking, bouncing and fragmentation collisions happen for any mass ratio of the colliding particles, whereas the mass transfer collisions need large difference in the projectile and target masses to occur.

we build simplified models that usually take into account only the impact speed and the mass ratio of colliding aggregates, and only the basic collision outcomes: sticking, bouncing, fragmentation, and fragmentation with mass transfer.

The four possible collision outcomes that we include are schematically shown in the Fig. 1.8. In the case of sticking, the two particles stick together thanks to the weak van der Waals interactions (for silicates) or the stronger dipole force (for ices). For such an event to occur, it requires a relatively low impact energy. The corresponding growth mode is called hit-and-stick growth and it leads to porous, fractal aggregates, because the grains stick at the first contact and the impact energy is too low to cause restructuring (Ossenkopf 1993; Wurm & Blum 1998; Blum et al. 2006). Such a simple sticking is impossible at high impact velocities, when the excess energy leads to compaction of grains. Compact grains do not stick well anymore, because there is no way for them to get rid of the excess energy, and the collisions lead to bouncing or fragmentation (Weidling et al. 2009; Zsom et al. 2010). However, it was found that there is a channel to growth even at high impact

speeds. It relies on collisions with high mass ratio of the particles. Such collisions can lead to a net growth of the more massive aggregate and are called fragmentation with mass transfer (Wurm et al. 2005; Teiser & Wurm 2009; Meisner et al. 2013). In such collisions, the small particle is fragmented but part of it sticks to the large one forming a dust cone. The corresponding growth mode is called *sweep-up growth* (Windmark et al. 2012a) and we investigate its efficiency in Chapters 3 and 4.

1.3.3 GROWTH BARRIERS

The mutual collisions can have a positive, negative or neutral effect on the mass of the colliding dust aggregates. The coagulation models show a general pattern: small aggregates grow until they reach a critical size and then the growth stops because of the growth barriers.

The growth barriers can in principle be divided in two groups. The first of them are the barriers resulting from the collisional physics of the dust aggregates. As mentioned in the previous section, under some conditions the mutual collisions do not lead to growth. These conditions are: high impact speeds (Blum & Münch 1993), compacted grains (Zsom et al. 2010), and electrostatic charge of the aggregates (Okuzumi 2009; Okuzumi et al. 2011a,b). Due to these problems, the growth is inhibited or even completely stopped. The maximum size of aggregates with respect to these barriers depends on the critical velocity above which particles do not stick v_{th} . The fragmentation of silicate aggregates takes place above a few tens cm s^{-1} to a few m s^{-1} , while bouncing collisions already happen at velocities of a few cm s^{-1} (Blum & Wurm 2008; Güttler et al. 2010; Kelling et al. 2014). Comparing these values with the impact speeds indicated in last panel of Fig. 1.7, we see that bouncing stops the growth already at mm-sizes and fragmentation comes into play for cm-sized particles. Assuming that the dominant impact speed source at the interesting sizes is the turbulence and using Eq. (1.28), we may derive the Stokes number corresponding to the maximum size of grains possible to obtain via sticking:

$$\text{St}_{\text{growth}} \approx \frac{v_{\text{th}}^2}{\alpha c_s^2}. \quad (1.31)$$

The second kind of barriers corresponds to the interplay between the growth and radial drift timescales. When the drift is more efficient than the growth, no large aggregates can be present, because they are removed from a given location faster than they can be replenished. The radial drift velocity $v_{\text{r,d}}$ can be calculated from Eq. (1.21). The drift timescale of a particle can be calculated as

$$\tau_{\text{drift}} = r \left(\frac{dr}{dt} \right)^{-1} = \frac{r}{|v_{\text{r,d}}|}, \quad (1.32)$$

1.3. CURRENT PLANET FORMATION THEORY

where r is radial distance from the central star. On the other hand, the growth timescale is

$$\tau_{\text{growth}} = a \left(\frac{da}{dt} \right)^{-1} = \mathcal{R}^{-1}, \quad (1.33)$$

where \mathcal{R} is the growth rate described with Eq. (1.26). In order to overcome the drift barrier, the condition

$$\tau_{\text{growth}} < \gamma \tau_{\text{drift}} \quad (1.34)$$

has to be fulfilled, where the parameter γ was determined by Brauer et al. (2008a) to be around 12. Birnstiel et al. (2012) derived the maximum Stokes number of particles that can be obtained with respect to the radial drift barrier to be

$$\text{St}_{\text{drift}} \approx \frac{Z}{2\eta}, \quad (1.35)$$

where $Z = \Sigma_{\text{d}}/\Sigma_{\text{g}}$ is vertically integrated dust-to-gas ratio (which we call metallicity), and η is a measure of the maximum drift speed described with Eq. (1.13).

The different barriers dominate in different regions of the disk. A rule of thumb is that the inner disk is dominated by the fragmentation (or bouncing) barrier, and the outer disk is dominated by the drift barrier. Fig. 1.9 shows the growth barrier maps in three different protoplanetary disk models, which were presented in Sect. 1.3.1. The fragmentation barrier (yellow region), where the high impact speeds lead to fragmentation instead of growth, is centered around the $\text{St} = 1$ line (red solid line), because as visible in Fig. 1.7 these grains acquire the highest relative velocities. It is present through the entire disk. The drift barrier (grey region), resulting from the short drift timescale, is only present in the outer disk. This is possible to understand by comparing Eq. (1.35) and Fig. 1.4: as the difference between the Keplerian rotation and the gas increases with the distance from the star, the outer regions are more affected by the radial drift problem. Additionally, as visible in Fig. 1.6, the same Stokes number corresponds to smaller grains in the outer disk than in the inner disk. Thus, the further away in the disk we are, the smaller aggregates are removed by the drift.

Additionally, in the Fig. 1.9 we show evolution of a few test particles (grey lines). We follow their growth and drift simultaneously solving the equations describing evolution of their size and location in the disk:

$$\begin{cases} a(t + \Delta t) = a(t) + \frac{da}{dt} \Delta t \\ r(t + \Delta t) = r(t) + \frac{dr}{dt} \Delta t \end{cases}. \quad (1.36)$$

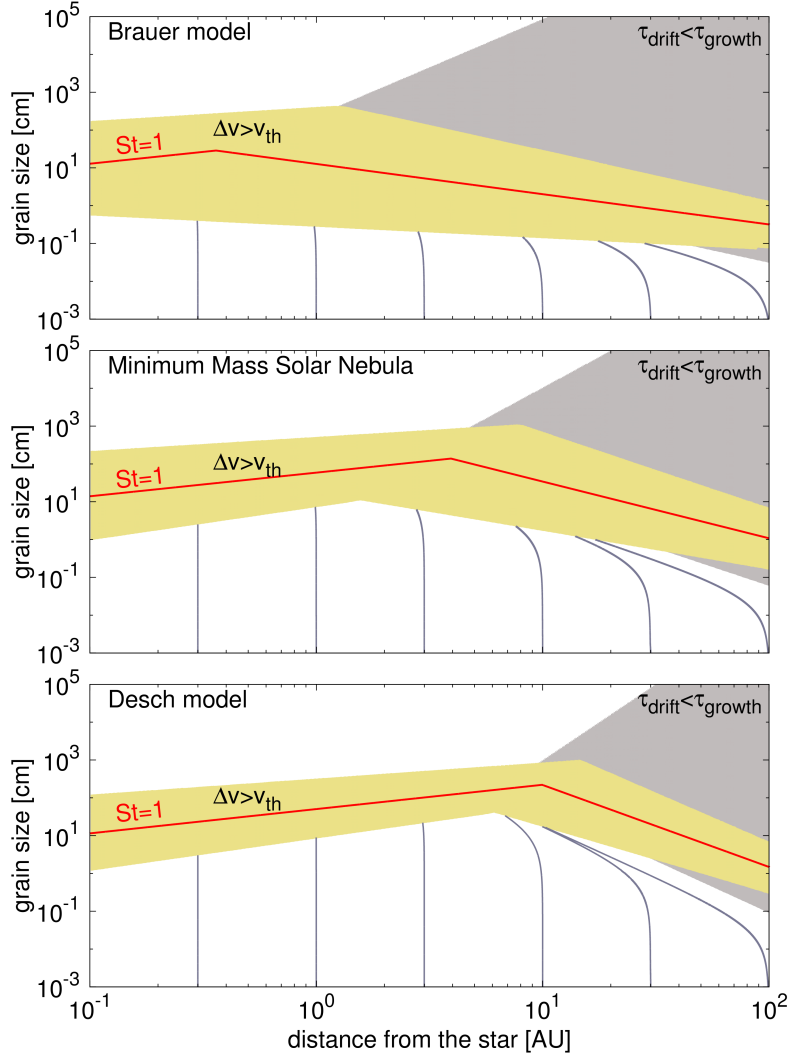


Figure 1.9: The growth barriers in three different disk models: the model proposed by Brauer et al. (2008a), the Minimum Mass Solar Nebula, and the Desch model. The red line shows grain size corresponding to the Stokes number of unity. The change of slope of this line comes from the change of drag regime: from Epstein in the outer disk to Stokes in the inner disk. The yellow shaded region corresponds to the fragmentation barrier, where impact speeds are higher than $v_{th} = 10 \text{ m s}^{-1}$. The grey shaded region corresponds to the drift barrier, where the radial drift timescale τ_{drift} is shorter than the growth timescale τ_{growth} . The grey lines show evolution of test particles that were initially placed in different places in the disk. In all the cases, the test particles are removed by the radial drift from the outer disk and fragment due to high impact speeds in the inner disk.

1.3. CURRENT PLANET FORMATION THEORY

The growth speed is calculated assuming that all the grains are the same size (*equal-sized growth*) and that every collision with impact speed Δv which is lower than some threshold value of v_{th} leads to a perfect sticking, otherwise the growth stops:

$$\frac{da}{dt} = \begin{cases} \rho_d \Delta v / \rho_p & \text{if } \Delta v < v_{\text{th}} \\ 0 & \text{if } \Delta v \geq v_{\text{th}} \end{cases}, \quad (1.37)$$

where ρ_p is the internal density of grains. The relative velocities Δv change with size and distance from the star (Fig. 1.7). While the dust grows, the dust density ρ_d increases, because the larger grains settle more efficiently towards the midplane (Eq. 1.25). The inward drift speed $dr/dt = v_{r,d}$ is described with Eq. (1.21). Its value is also dependent on the grain size, thus the interplay between drift and growth may not seem very intuitive. As visible in Fig. 1.9, the evolution typically leads to redistribution of the solids and a significant change of the dust density profile: the outer disk is depleted and the solids pile-up in the inner disk (Birnstiel et al. 2012). We come back to this point in Chapter 4.

1.3.4 PLANETESIMAL FORMATION SCENARIOS

In the previous section, we discussed the growth barriers that pose major problems in forming any bodies larger than cm-sized pebbles. Since the barriers are so strong, how can the planets form? This is the question we try to answer in this dissertation. Below, we introduce some concepts that have been presented in the literature and that might be capable of forming planetesimals. The number of such scenarios have increased in recent years, but they are still unsettled and some of them are very much conceptual only.

PRESSURE BUMPS

The growth barriers are in principle caused by the sub-Keplerian rotation of the gas that enforces the radial drift of dust, which also significantly contributes to the impact speeds. Thus, it was proposed that if the disk structure is locally modified such that the pressure gradient is reduced and the turbulence is weak, the growth barriers could be overcome (see e.g. Whipple 1972; Barge & Sommeria 1995; Klahr & Henning 1997; Haghhighipour & Boss 2003b; Kretke & Lin 2007). Pressure bumps are required to explain the existence of mm-sized grains observed in the outer parts of protoplanetary disks (Pinilla et al. 2012b, 2013). In such favorable places, planetesimals could form even via direct coagulation (Haghhighipour & Boss 2003a; Haghhighipour

CHAPTER 1. INTRODUCTION

2005; Brauer et al. 2008b). We study the dust dynamics in the vicinity of a pressure bump in Chapter 3.

SWEEP-UP GROWTH

As we already mentioned in Sect. 1.3.2, growth of aggregates is possible even at high impact speeds. However, a high mass ratio between the colliding particles is required. Thus, if only a few grains that are sufficiently larger than the average manage to form, they could keep growing by sweeping up the rest (Windmark et al. 2012a). Windmark et al. (2012b) and Garaud et al. (2013) suggested that such grains can be formed due to stochastic impact velocities contributed by turbulence. Around 1 in 10^{30} grains may be "lucky" enough to collide only in low velocity collisions 100 times in a row. Such a grain is then 100 times more massive than the average grain, and the following high speed collisions will lead to growth via the fragmentation with mass transfer effect. We investigate this scenario in Chapter 4. In Chapter 3, we propose another possibility of providing the large grains: the radial mixing of large aggregates formed in a dead zone of the disk.

STREAMING INSTABILITY

The complicated interplay between dust and gas leads to development of a powerful instability that is causing local enhancements of dust-to-gas ratio (Goodman & Pindor 2000; Youdin & Goodman 2005). Such local enhancements, or clumps, behave like large aggregates and orbit with Keplerian speed. Single grains move with a sub-Keplerian speed and thus are swept by the clumps, which increase their mass. Under some conditions: existence of sufficiently large pebbles and an enhanced total metallicity, this process may lead to formation of clumps that are massive enough to gravitationally collapse and form roughly 100 km-sized planetesimals (Johansen et al. 2007, 2011). We test this scenario in Chapter 5.

TURBULENT CONCENTRATION

The turbulent concentration scenario is somewhat similar to the streaming instability. However, the formation mechanism of the clumps in this case is the turbulence. It was known for a long time that dust aggregates with stopping times corresponding to an eddy turnover time are ejected from the eddies and concentrate in between them (Fessler et al. 1994). Cuzzi et al. (2001, 2008, 2010) and Chambers (2010) proposed that this mechanism can be used to form dense clumps of mm-sized particles (for example the chondrules) that will collapse to planetesimals. Although usual dust density enhancement caused by this process is on the order of 100, a low probability exists that it will reach 10^4 and the clump will become self-gravitating.

1.3. CURRENT PLANET FORMATION THEORY

SECULAR GRAVITATIONAL INSTABILITIES

One of the problems of the turbulent concentration scenario is that the probability of reaching densities allowing for fast collapse of the dust clumps is very low. Nevertheless, the collapse can happen even at lower dust densities, because it is mediated by the gas drag. However, its timescale may be long and thus the collapse may be prevented by the orbital shear or turbulence. Nevertheless, the idea of planetesimal formation via secular gravitational instabilities has been recently investigated by [Youdin \(2011a\)](#), [Michikoshi et al. \(2012\)](#), and [Takeuchi & Ida \(2012\)](#). The conclusions are that dust can collapse directly to planetesimals on timescale shorter than disk dissipation only in massive disks with enhanced dust abundance.

FLUFFY ICE AGGREGATES

Part of the problems with forming planetesimals (described in Sect. 1.3.3) comes from the fact that the initially fluffy dust aggregates get compacted and do not stick anymore. The aggregates consisting of water ice may avoid these problems ([Suyama et al. 2012](#)): they stay very porous, do not bounce, and fragment only at impact velocities that are not even reached in the protoplanetary disk. [Okuzumi et al. \(2012\)](#) and [Kataoka et al. \(2013a\)](#) showed that evolution of icy aggregates leads to rapid planetesimal formation in the inner disk. However, these planetesimals would be destroyed by evaporation of the ice inside the snow line unless they grow large enough to get gravitationally compacted.

ICE CONDENSATION

The ice properties facilitate growing large bodies. [Ros & Johansen \(2013\)](#) investigated evaporation and re-condensation of ice in the vicinity of the snow line and concluded that this mechanism can lead to planetesimal formation. However, this model does not take into account the possibility of ice condensation on the silicate grains and thus overestimate the growth of the icy cores. Planetesimal formation in this model is only local and restricted to the snow line region.

1.3.5 PLANETESIMAL EVOLUTION AND PLANET FORMATION

Assuming that the km-sized planetesimals formed despite the growth barriers, there is still a long way to go until formation of > 1000 km-sized planets. In this section, we briefly describe the concepts that are useful in growing ever larger bodies in the gravitational regime.

RUNAWAY GROWTH

The growth of planetesimals is accelerated by gravitational focusing, which enhances the cross section for collisions. The nominal geometrical value

σ we used for collisions between dust aggregates in Sect. 1.3.2 now becomes

$$\sigma_{\text{GF}} = \pi (a_1 + a_2)^2 \left[1 + \left(\frac{v_{\text{esc}}}{\Delta v} \right)^2 \right], \quad (1.38)$$

where a_1 and a_2 are sizes of the colliding bodies, v_{esc} is escape velocity and Δv is relative velocity. The escape velocity from a planetesimal is

$$v_{\text{esc}} = \sqrt{\frac{2Gm}{a}}, \quad (1.39)$$

where m and a are the its mass and radius. The collisional cross section increases with mass, meaning that a more massive planetesimal will be able to gain even more mass faster than the less massive ones. This leads to *runaway growth*, where a few bodies grow much faster than the other ones. The runaway growth stops because the massive bodies gravitationally stir their environment and the velocity dispersion Δv increases (Ormel et al. 2010). In a traditional scenario, the growth mode changes to so-called oligarchic growth, when one dominant body sweeps up its neighbourhood. However, an intermediate stage is also possible, when the runaway growth is already over but more than one competing pre-planetary cores grow in the same region (Lithwick 2014). Recent developments also show that the runaway growth may be inhibited by the velocity dispersion induced by turbulence (Ormel & Okuzumi 2013).

PEBBLE ACCRETION

The cores of giant planets in the Solar System had to form quickly, in order to accrete their gaseous atmospheres: the timescale for gas disk dispersion is on the order of 1 Myr. The minimum core mass for an efficient gas accretion is $\sim 10 M_{\oplus}$ ($1 M_{\oplus} = \text{Earth mass}$) (Hubickyj et al. 2005). The traditional runaway and oligarchic growth scenario may be not efficient enough to reach such embryo mass in this short time (Chambers 2006; Levison et al. 2010; Ormel & Kobayashi 2012). A solution for this problem may be accretion of smaller solids: the pebbles. The gas flow around the growing core enhances accretion rate of cm-sized pebbles such that giant planets cores can be formed on timescales shorter than 1 Myr (Ormel & Klahr 2010; Lambrechts & Johansen 2012; Chambers 2014). This scenario requires an existence of large amounts of these pebbles, that were not turned to planetesimals directly, which as we show in the following chapters, is consistent with the current planetesimal formation models.

1.3. CURRENT PLANET FORMATION THEORY

CORE ACCRETION AND PLANET MIGRATION

Giant planets are qualitatively different from the terrestrial planets because they possess significant gaseous atmospheres. There are two basic theories of the formation of giant planets: *core accretion* and gravitational disk instability. The second one requires a massive disk that is unstable, meaning that the Toomre parameter defined as

$$Q = \frac{c_s \Omega_K}{\pi G \Sigma_g} \quad (1.40)$$

is less than unity. If the gas is able to cool on sufficiently short timescale, the gravitational instability leads to formation of roughly Jupiter mass bound objects (Boss 1997; Mayer et al. 2002). The instability works very quickly and the planets form on orbital timescale. The main problems of this scenario are that the gas cooling is not necessarily as efficient in the real disks (Rafikov 2005) and that it forms planets only at distances larger than ~ 50 AU (Chabrier et al. 2014).

We base our work on the core accretion framework, where the solid cores of the giant planets are formed first and the gas envelope is accreted only afterwards (Pollack et al. 1996). As mentioned in the previous section, the cores can only accrete the gas efficiently if they are more massive than $\sim 10 M_\oplus$ and thus they have to form quickly. Another issue is that if a core stays in place, the reservoir of gas that it can accrete is limited: even a low mass planet opens a gap in the disk and this stops the accretion (Bryden et al. 1999; Rafikov 2001; Duffell & MacFadyen 2013). However, it is known that due to the planet-disk interactions, the planets migrate in the disk and thus can possibly accrete gas from different places (D'Angelo & Lubow 2008).

There are in principle two main regimes of the planet migration (Kley & Nelson 2012). Terrestrial mass planets migrate in so-called Type I migration. This is caused by gravitational torque from the spiral waves generated in the gas by the planet. Due to this interaction, planets usually lose angular momentum and drift inwards. The timescale of the drift may be very short, posing a major problem on keeping the planets in the disk (Tanaka et al. 2002), which is similar to the radial drift barrier to dust growth. However, the low mass planets are fully embedded in gas and can grow by accretion of gas and solids. More massive planets, starting at $\sim 10 M_\oplus$, perturb the gas disk strongly and migrate in Type II migration. In this regime, the motion of the planet follows the viscous evolution of the disk: if the gas is flowing inward, the planet also moves inward, however the timescale is much longer than the Type I migration.

1.4 NUMERICAL MODELS OF DUST EVOLUTION

In the previous section, we described the current theory of planet formation, focusing on its first stages. Now, we briefly introduce the numerical methods used to model dust evolution in protoplanetary disks. There are two main approaches to model dust growth: one of them is based on solving the *Smoluchowski equation* and the other is based on the *Monte Carlo* algorithms. In Chapter 4, we directly compare the approaches in the context of planetesimal formation and discuss their pros and cons in more details.

1.4.1 SOLVING THE SMOLUCHOWSKI EQUATION

Time evolution of the dust mass distribution can be followed with the Smoluchowski coagulation equation, originally presented by [Smoluchowski \(1916\)](#). In the simplest form, only describing coagulation, and with a rate dependent only on the mass of the particles, the Smoluchowski equation has the following form:

$$\begin{aligned} \frac{\partial f(m)}{\partial t} = & -f(m) \int K(m, m') f(m') dm' + \\ & + \frac{1}{2} \int K(m', m - m') f(m') f(m - m') dm', \end{aligned} \quad (1.41)$$

where $f(m)dm$ is density of particles with masses in range $[m, m + dm]$. The first term on the right side of the equation accounts for the loss of particles in this range of mass as they coagulate with other grains. The second term describes gain of the density $f(m)dm$ because of the coagulation of particles with the complementary masses $m - m'$ and m' . The factor of $\frac{1}{2}$ is to avoid counting the same particle twice: as there are two particles merging into one. $K(m, m')$ is the collision kernel that describes how likely is an interaction between particles of masses m and m' .

The Smoluchowski equation, in the simplest form presented here, has analytical solutions only for three idealized collision kernels: the constant kernel $K(m, m') = 1$, the linear kernel $K(m, m') = m + m'$, and the product kernel $K(m, m') = m \times m'$. These kernels do not reflect realistic physical conditions in protoplanetary disk, but are useful to test numerical codes (see Sect. 2.3.1).

Numerical integration of the Smoluchowski equation requires setting mass grid. The code then follows the amount of dust in each mass bin defined by a mass range $[m, m + dm]$. A schematic picture of this process is presented in Fig. 1.10. In order to follow the mass distribution evolution over many orders of magnitude, the mass bins are logarithmic in the real codes. This causes

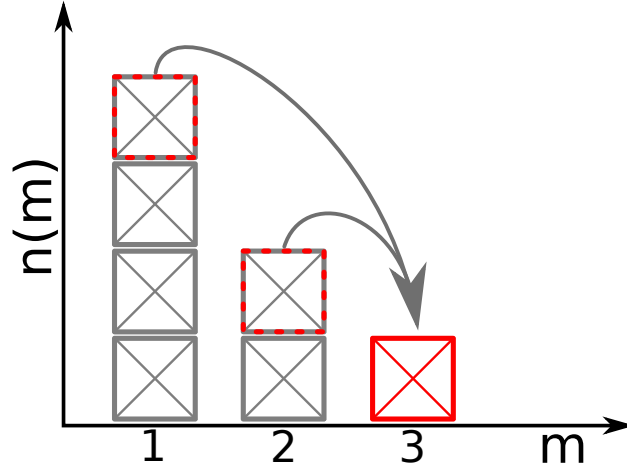


Figure 1.10: Illustration of the Smoluchowski approach to dust coagulation modeling: the two highlighted particles from mass bins 1 and 2 stick together and form the red particle of mass 3. The two original grey particles are removed from the corresponding bins and a new particle is added to the mass distribution.

the problem that after coagulation, the mass of the newly formed particle m does not exactly match any single mass bin. Thus, an interpolation is necessary. Part of the corresponding density is inserted to a bin of a slightly lower mass $m_i < m$, and the remaining part is inserted to a bin representing a slightly higher mass $m_j > m$. Unfortunately, this procedure causes diffusion of the mass distribution, as inserting mass to the bin $m_j > m$ produces more massive particles than the collision in reality leads to. Severe consequences of the numerical problems may arise, which are discussed in Chapter 4.

Modeling the dust coagulation in the protoplanetary disk requires extending the simple Smoluchowski equation from Eq. (1.41) such that it covers multiple collisions outcomes: not only sticking but also bouncing, fragmentation, and mass transfer (see Fig. 1.8). Additional terms are also necessary to include effects like the radial drift or turbulent diffusion and model dust evolution in a global disk. The equation then becomes quite complicated and solving it is a true computational challenge. Implementations of the Smoluchowski approach in the planet formation context were described among others by Weidenschilling (1980); Ohtsuki et al. (1990); Dullemond & Dominik (2005); Brauer et al. (2008a); Okuzumi et al. (2009), and Birnstiel et al. (2010).

1.4.2 MONTE CARLO METHODS

The Monte Carlo approach was proposed by a Polish-American mathematician Stanisław Ulam to model processes that are too complicated to be described with closed-form expressions: originally it was used to model the nuclear fission (Metropolis & Ulam 1949). The method is based on combining the statistical sampling with the capabilities of modern computers. Using this method means performing numerical experiments in which we draw a random number every time when there is an event that can have several outcomes. By performing the same experiment many times, each time with different random numbers, we learn about different possible scenarios of the process under investigation and we can draw conclusions about its typical outcome.

In the dust coagulation context, the Monte Carlo approach means that we follow "lives" of some number of dust particles. We model how their properties change when they collide with each other. How do we know which of them should collide? We draw random numbers. However, we take into account that collisions between some particles are more probable than with the others: this is what the coagulation kernel $K(m, m')$ mentioned in the previous section describes. The impact speeds can be calculated depending on an adopted protoplanetary disk model and the outcome of the collision is known basing on a model created thanks to the laboratory experiments (see Sect. 1.3.2). A great advantage of this approach is that it is easy to add new properties of the particles: like their internal structure or composition. This approach does also allow to include more parameters of the collision, like for example the impact angle, as every collision is modeled separately. This is very tough with the Smoluchowski equation approach, where one deals with the mass distribution function. However, the Monte Carlo methods are generally computationally expensive and thus the number of particles we can follow is limited.

Implementations of the Monte Carlo approach to dust coagulation in protoplanetary disk were described by Ormel et al. (2007) and Zsom & Dullemond (2008). A new implementation of the Monte Carlo approach is described in Chapter 2. This implementation is based on the representative particle approach, where instead of dealing with single particles, we group them into so-called representative bodies and thus the amount of dust we can include in our models increases. However, this approach limits the mass dynamic range, as discussed in Chapter 4.

1.5 OVERVIEW OF THIS DISSERTATION

This dissertation focuses on the planetesimal formation problem. We investigate different scenarios of overcoming the growth barriers, check what conditions are necessary for these scenarios to operate, and test their capability of turning dust to planetesimals. This dissertation is organized as follows:

In Chapter 2, we develop a new code for dust evolution in protoplanetary disk. The code allows us to investigate the radial and vertical evolution of dust grains, joining their dynamics and growth. This code is based on the Monte Carlo approach and treats dust as representative particles. A significant development over previous codes is made by introduction of an adaptive grid routine, which allows us to obtain a very high spatial resolution in the disk midplane, and extending this approach to 2 spatial dimensions. We describe the code and present its basic tests. The code is then used in the following chapters.

In Chapter 3, we test the possibility of planetesimal formation in a privileged location in the disk: in a vicinity of the inner edge of dead zone, which corresponds to the snow line in our model. We investigate planetesimal formation via sweep-up growth that is driven by radial mixing of dust aggregates. We perform 2-D models of the snow line region with the new code presented in Chapter 2. We investigate whether large aggregates formed in the dead zone, where the lack of turbulence reduces the impact speeds, can continue to grow via the sweep-up of the small particles in the active zone and check the efficiency of this process.

In Chapter 4, we focus on planetesimal formation triggered by the impact speeds distribution contributed by turbulence. We investigate this scenario in local models performed both with our Monte Carlo code and a Smoluchowski equation solver. The comparison of results obtained with both the approaches leads to restricting outcome of this process and additionally shows the advantages and disadvantages of the two computational approaches. The possibility of sweep-up growth allows us to overcome the collisional barriers, but we are still left with the radial drift problem. We show that the interplay between growth and drift leads to local planetesimal formation in the inner part of the disk.

In Chapter 5, we investigate planetesimal formation via gravitational collapse of dense pebble clumps formed because of the streaming instability.

CHAPTER 1. INTRODUCTION

This scenario allows us to overcome both the collisional and drift barrier, but relatively large pebbles are needed to trigger it. We check whether sufficiently large aggregates can form via dust coagulation, and develop a method to model the interplay of dust growth and the streaming instability. We also develop an analytical model that quantifies the amount of planetesimals formed in this scenario.

Chapter 6 summarizes all the work described in this dissertation. Some future prospects are also discussed.

1.5. OVERVIEW OF THIS DISSERTATION

A NEW MONTE CARLO CODE FOR DUST EVOLUTION

Adapted from Drążkowska, Windmark & Dullemond, 2013, A&A, 556, A37¹

2.1 INTRODUCTION

Modeling the planet formation is not only difficult because of the growth barriers at the first stage of the process, which are described in Sect. 1.3.3. Formation of a single planet covers about 40 orders of magnitude in mass, which is not possible to handle with any traditional method, because of a fundamental difference in the physics involved in its different stages. In the small particle regime, there are too many independent particles for an individual treatment. The coagulation is driven by random collisions. Therefore, the statistical methods described in Sect. 1.4.1 are used to model the evolution of the fine dust medium (Weidenschilling 1980; Nakagawa et al. 1981; Brauer et al. 2008a; Birnstiel et al. 2010). In this approach, the dust medium is followed using the grain distribution function $f_d(m, r, t)$, giving the number of dust particles of particular properties at a given time. In the big body regime, the evolution is led by gravitational dynamics. That forces us to treat the objects individually using N-body methods (Kokubo & Ida 2000). A connection between the two methods requires an ad hoc switch. Such a solution has been implemented by Spaute et al. (1991), Bromley & Kenyon (2006) and recently Glaschke et al. (2011).

In addition to the statistical methods mentioned above, there are also Monte Carlo methods used in the small particle regime (Gillespie 1975; Ormel et al. 2007), which are introduced in Sect. 1.4.2. In recent years, a new kind of algorithm has been developed: a Monte Carlo algorithm with the representative particle approach (Zsom & Dullemond 2008). In this method, the huge number of small particles are handled by grouping the (nearly) identical bodies into swarms and representing each swarm by a representative particle. Instead of evolving the distribution function $f_d(m, r, t)$, it is sampling and

¹See page ix for the authorship details.

reproducing it with the use of the representative bodies. This manner should allow a much smoother and more natural transition to the N-body regime. Indeed, this kind of approach is already used in the N-body codes. [Levison et al. \(2010\)](#) applied a superparticle approach to treat planetesimals. They showed that taking the gravitational interactions into account is very important in the case of kilometer size bodies. The gravitational interplay can lead to redistribution of the material and change accretion rates in the disk.

With the work presented in this chapter, we make the very first step toward a new computational model that will connect the small scale dust growth to the large scale planet formation. We develop a 2-D Monte Carlo dust evolution code, able to resolve a protoplanetary disk structure in radial and vertical dimension. We assume that the disk is cylindrically symmetric, thereby ignoring the azimuthal dependence. We use an analytical description for the gas disk. The dust is treated using the representative particle approach. The code is a further development of the work presented by [Zsom et al. \(2011a\)](#). The code is written in Fortran 90 and is parallelized using OpenMP directives.

2.2 CODE STRUCTURE

In each time step the code performs the following steps:

1. Advection velocities of the dust particles are determined taking their current properties and positions into account.
2. The code time step is calculated on the basis on the advection velocities and existing grid, following the Courant condition.
3. Advection of the particles is performed both in radial and vertical direction. The solids undergo the radial drift, vertical settling and turbulent diffusion.
4. The new grid is established according to the updated positions of the particles, using the adaptive grid routine (see [Fig. 2.1](#)).
5. Collisions between the particles are performed in each cell by the Monte Carlo algorithm. The particle properties are updated.
6. The output is saved when required.

An illustration of the code structure presented in [Fig. 2.1](#). More detailed description of the approach used in the code can be found in the following sections.

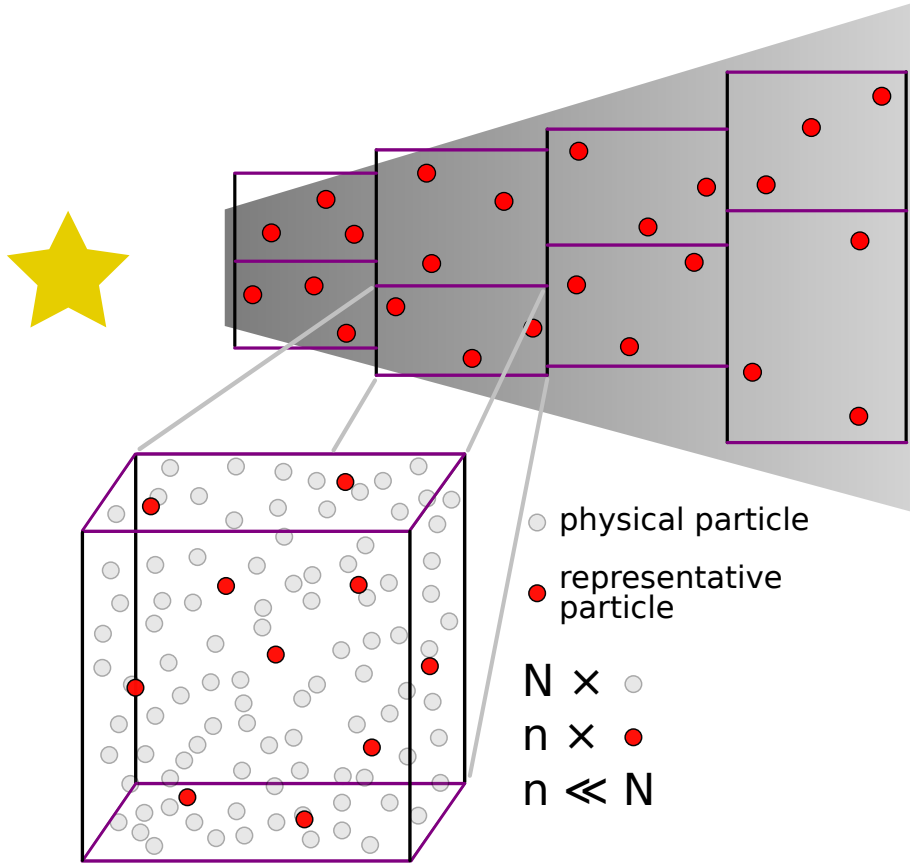


Figure 2.1: Illustration of the code structure: we investigate dust evolution in an axisymmetric protoplanetary disk. We consider the radial and vertical structure of the disk. The gas is treated with analytical approach (Sect. 2.2.1). The dust is described with the representative particle approach (Sect. 2.2.2). The red dots correspond to the representative particles, each of them representing many of the physical (grey) particles. In order to perform collisions, grid is established with the adaptive grid algorithm: first, the vertical (black) walls are established so that the number of the representative particles in each radial zone is equal. Then the horizontal (purple) walls are set up for each radial zone individually in order to preserve equal number of swarms in each cell. Dust coagulation is computed in each cell individually using the Monte Carlo method (Sect. 2.2.4).

2.2.1 GAS DESCRIPTION

The gas structure is implemented in the form of analytical expressions for the gas surface and volume density $\Sigma_g(r)$ and $\rho_g(r, z)$, pressure $P_g(r)$, temperature $T_g(r)$ and turbulent viscosity $D_g(r)$.

For now we assume that the gas in the disk does not evolve, although this is not a fundamental restriction, and the gas evolution is possible to implement without severe changes in the code structure. In a first-order approximation, the time evolution can be implemented analytically by expanding the gas properties description from the function of space $f_g(r)$ to the function of space and time $f_g(r, t)$.

2.2.2 DUST DESCRIPTION

REPRESENTATIVE PARTICLE APPROACH

To describe the dust, we use the approach based on [Zsom & Dullemond \(2008\)](#). We follow the "lives" of n representative particles, which are supposed to be a statistical representation of N physical particles present in an examined domain. Commonly $n \ll N$. For a typical protoplanetary disk, with mass of $0.01 M_\odot$ and a dust to gas ratio of 0.01, consisting of $1 \mu\text{m}$ size dust grains, we would have $N \approx 10^{42}$. For computational feasibility we would have e.g. $n = 10^5$, meaning each representative particle i represents $N_i \approx 10^{37}$ physical particles.

All of the N_i physical particles, represented by a single representative particle i , share identical properties: for now these are mass m_i and location in the disk (r_i, z_i) . As we impose the axial symmetry, we do not include the azimuthal position. We assume that the physical particles belonging to one swarm are homogeneously distributed along an annulus of given location r_i and height above the midplane z_i . The total mass of physical particles contained in one swarm $M_{\text{swarm}} = N_i m_i$ is identical for every representative particle and it does not change with time. This means that the N_i has to drop when the particle mass m_i grows. This is not a physical effect, just a statistical. See [Zsom & Dullemond \(2008\)](#) for details.

With the representative particle approach, it is relatively easy to add further dust properties, in particular the internal structure of aggregates, which was shown to be important by [Ormel et al. \(2007\)](#). We leave the implementation of the porosity for further work.

When performing the advection, we assume that all of the physical particles in the swarm undergo the same change of the position (r_i, z_i) and after the shift, they are still uniformly distributed along the designated annulus. However, when we consider the collisions, we set up a numerical grid in order

to account for the fact that only particles that are physically close can collide. In this case, we assume that the particles are homogeneously distributed inside a grid cell (see Sect. 2.2.4 for description of the grid). This assumption is required by the method used to investigate the collisional evolution of the aggregates (Zsom & Dullemond 2008). The difference between the locations assumed in both of the cases is most often not important and can be treated as a kind of systematic uncertainty.

2.2.3 ADVECTION OF DUST PARTICLES

The location of a representative particle changes because of radial drift and vertical settling as well as turbulent diffusion. The main particle characteristics determining its behavior with respect to gas is so called Stokes number St . It is defined as

$$St = t_s \Omega_K, \quad (2.1)$$

where Ω_K denotes the Kepler frequency and t_s is the so-called stopping time of the particle. The Stokes number can be treated as a particle-gas coupling strength indicator. If $St \ll 1$, the particle is well coupled to the ambient gas and its motion is fully dependent on the motion of the gas. On the other hand, the particles with $St \gg 1$ are practically independent of the gas.

The stopping time of the particle t_s determines a timescale that the particle needs to adjust its velocity to the velocity of the surrounding gas. The exact expression that we use to compute the t_s depends on the particle radius a . The ratio of the mean free path of the gas λ_{mfp} and the particle size a is called Knudsen number Kn :

$$Kn = \frac{\lambda_{\text{mfp}}}{a}. \quad (2.2)$$

If a particle's Knudsen number is $Kn > 4/9$, the particle is in the Epstein drag regime and its stopping time is given by (Weidenschilling 1977a)

$$t_s^{\text{Ep}} = \frac{a \rho_p}{v_{\text{th}} \rho_g}, \quad (2.3)$$

where ρ_p is the internal density of the particle and v_{th} is the thermal velocity of the gas. The latter is expressed as $v_{\text{th}} = \sqrt{8k_B T_g / \pi m_g}$, where k_B is the Boltzmann constant, T_g is the gas temperature and m_g is mass of the gas molecule. On the other hand, when $Kn < 4/9$, the particle is in the Stokes regime. As mentioned in Sect. 1.3.2, the Stokes regime is in general not homogeneous and is often divided into subregimes. The Reynolds number of the particles Re defines which of the subregimes applies (Weidenschilling

1977a). The Re is specified as

$$Re = \frac{2a\Delta v_{pg}}{\nu_g}, \quad (2.4)$$

with a denoting the particle radius, Δv_{pg} the relative velocity between the particle and the gas and ν_g the molecular viscosity of gas that is expressed as $\nu_g = v_{th}\lambda_{mfp}/2$. As long as $Re < 1$, the first Stokes regime applies. In our models $Re > 1$ translates into $a \gtrsim 10^4$ cm ($m \gtrsim 10^{12}$ g). This is larger than we obtain in the models presented in this dissertation. Thus, there is no need to include the other Stokes regimes. For the particles with $Kn < 4/9$ we assume (Weidenschilling 1977a)

$$t_s^{St} = t_s^{Ep} \times \frac{4}{9}Kn^{-1}. \quad (2.5)$$

RADIAL DRIFT

The radial drift of dust particles has two sources. One of them is the gas accretion onto the central star. The gas moves inwards and drags the dust particles with it. This phenomenon is stronger for small particles ($St \ll 1$), and it is not important for big ones ($St \gg 1$). The drift velocity caused by this effect can be expressed as (Brauer et al. 2008a)

$$v_d^{acc} = \frac{v_g^r}{1 + St^2}, \quad (2.6)$$

where v_g^r denotes the accretion velocity of gas. We use a convention in which the $v_g^r < 0$ indicates inward drift.

The other effect is also related to the coupling of the solids to gas, but now the radial drift is a result of orbital movement. In a gas-free environment, the solid particles orbit around the star with the Keplerian velocity v_K , resulting from a balance between the gravity and the centrifugal force. For the gas however, the pressure needs to be considered. Therefore, the gas moves with a sub-Keplerian velocity. Because of the difference in the azimuthal velocity of gas and dust, the dust particles feel a constant head-wind. Interacting with the gas via the drag force, they lose the angular momentum and thus drift inwards with velocity (Weidenschilling 1977a; Brauer et al. 2008a):

$$v_d^{drift} = \frac{2v_\eta}{St + \frac{1}{St}}. \quad (2.7)$$

Hence, this effect is not significant for both very small and very big dust particles, but for the particles with $St \approx 1$ the drift velocity v_d^{drift} can reach even 30 m s^{-1} (Brauer et al. 2008a).

The maximum drift velocity v_η can be expressed as (Brauer et al. 2008b)

$$v_\eta = \frac{\partial_r P_g}{2\rho_g \Omega_K}. \quad (2.8)$$

The v_η is dependent on the gas pressure gradient $\partial_r P_g$, which can be both negative (in most of the standard disk models it is negative over the whole disk) and positive. If we find a disk model, in which locally $\partial_r P_g > 0$ (a so-called *pressure bump*), we get outward radial drift of solids that leads to a local significant enhancement of dust density.

The total radial drift velocity is given by

$$v_d^r = v_d^{\text{acc}} + v_d^{\text{drift}}. \quad (2.9)$$

VERTICAL SETTLING

The dust particles present in the protoplanetary disk are settling down towards the midplane due to gravity from the central star. The settling velocity is regulated by the gas drag. It can be obtained from basic equations as (Dullemond & Dominik 2004)

$$v_d^z = -z\Omega_K^2 t_s, \quad (2.10)$$

where z is the height above the midplane. It can be rewritten using Eq. (2.1) as

$$v_d^z = -z\Omega_K \text{St}. \quad (2.11)$$

For big particles, the velocity calculated from Eq. (2.11) would be higher than the orbital velocity projected on the z axis, so we restrict it to

$$v_d^z = -z\Omega_K \min(0.5, \text{St}), \quad (2.12)$$

following e.g. Birnstiel et al. (2010). This description is not valid for big particles that are completely decoupled from the gas. These particles undergo the orbital oscillations around the midplane. A direct integration of the equations of motion would need to be included in order to account for this effect. We leave it for further work.

TURBULENT DIFFUSION

If there were no other effects in the disk, all the dust would eventually form an infinitely thin layer in the midplane. However, we assume that there is a turbulence present in the disk. We implement the effect of the turbulence on the particles spatial distribution in the same way to Ciesla (2010) and Zsom et al. (2011a). We take the diffusion in both vertical and radial directions into account.

2.2. CODE STRUCTURE

The turbulence generally smears out the density distribution (turbulent diffusion). If we take a point dust distribution after time t it will become a Gaussian distribution with the half width L (in 1-D):

$$L = L(t) = \sqrt{2D_d t}, \quad (2.13)$$

where D_d is the dust turbulent diffusion coefficient, which we can express as

$$D_d = \frac{D_g}{\text{Sc}}, \quad (2.14)$$

where Sc is called the Schmidt number, and the gas diffusion coefficient D_g (turbulent viscosity) is assumed to have the form of so-called α viscosity (Shakura & Sunyaev 1973):

$$D_g = \alpha c_s H_g. \quad (2.15)$$

α is a parameter describing the efficiency of the angular momentum transport with values typically much lower than 1. c_s is the sound speed in gas and H_g is gas pressure scale height, which is expressed as $H_g = c_s/\Omega_K$. The Schmidt number is currently estimated as (Youdin & Lithwick 2007; Carballido et al. 2011)

$$\text{Sc} = 1 + \text{St}^2. \quad (2.16)$$

We implement the turbulent diffusion of the solid particles as random jumps. We add a term corresponding to our turbulence prescription to the velocity resulting from the radial drift and vertical settling. The turbulent velocity resulting from the prescription given above is

$$v_d^{\text{D1}} = \frac{\Delta x}{\Delta t}, \quad (2.17)$$

where Δx is the displacement of the particle during the time step Δt . The displacement is taken as a random number drawn from a Gaussian distribution with the half width L from Eq. (2.13).

This description of the diffusion is however simplified. In fact, there is an additional term in the diffusion equation for a non-homogeneous gas distribution. The velocity component resulting from this effect always points towards the gas density maximum. Therefore, the dust scale height never exceeds the gas scale height. For more details see Zsom et al. (2011a) (their Eqs. 7 and 8). The velocity corresponding to this term can be noted as

$$v_d^{\text{D2}} = D_d \frac{1}{\rho_g} \frac{\partial \rho_g}{\partial x}, \quad (2.18)$$

where x in Eqs. (2.17) and (2.18) can be both r and z , depending on direction along that we consider the diffusion.

2.2.4 COLLISIONS

MONTE CARLO METHOD

We model the dust coagulation using a Monte Carlo algorithm (see Sect. 1.4.2). This approach was already used in the protoplanetary disk context by Ormel et al. (2007). Our implementation is based on an approach presented for the first time by Gillespie (1975). Zsom & Dullemond (2008) described in detail how to use this algorithm with the representative particles approach. Only the main facts are stated here for the reader's convenience.

As mentioned in Sect. 2.2.2, we assume that a limited number n representative particles represent all N physical particles present in the computational domain. Each representative particle i describes a swarm of N_i identical physical particles. Total mass M_{swarm} of every swarm is equal and constant in time.

As we typically have $n \ll N$, we only need to consider the collisions between representative and non-representative particles. The collisions between the representative particles are too rare to be significant. The collisions among the physical particles do not need to be tracked as the basic assumption of the method.

The particles taking part in the subsequent collisions as well as the time step between the events are determined on a basis of random numbers. For each collision we pick one representative particle i and one non-representative particle from the swarm represented by the representative particle k . It is possible that $i = k$. The probability of a collision between particles i and k is determined as

$$\mathcal{R}_{ik} = \frac{N_k K_{ik}}{V}, \quad (2.19)$$

where V is the cell volume and K_{ik} is a coagulation kernel. Apart from some test cases we use

$$K_{ik} = \Delta v_{ik} \sigma_{ik}, \quad (2.20)$$

where Δv_{ik} is the relative velocity between particles i and k and σ_{ik} is the geometrical cross section for their collision. The total collision rate among any of the pairs is

$$\mathcal{R} = \sum_i \sum_k \mathcal{R}_{ik}. \quad (2.21)$$

We first choose the representative particle, and the probability that it is particle i is

$$P_i = \frac{\sum_k \mathcal{R}_{ik}}{\mathcal{R}}. \quad (2.22)$$

Then we choose the non-representative particle with the probability:

$$P_{k|i} = \frac{\mathcal{R}_{ik}}{\sum_k \mathcal{R}_{ik}}. \quad (2.23)$$

The time step between the subsequent collisions is determined as

$$\tau = -\frac{1}{\mathcal{R}} \ln(\text{rand}), \quad (2.24)$$

where the rand is a random number drawn from the uniform distribution between 0 and 1.

As a result of the collision, only the representative particle i changes its properties. For example, in the case of sticking, $m_i \leftarrow m_i + m_k$. Every time the mass of the particle changes, the number of particles represented by the swarm has to be updated as $N_i = M_{\text{swarm}}/m_i$.

ADAPTIVE GRID

The coagulation of dust aggregates depends on the local properties of the ambient gas. This is the reason why, to perform the collisions, we first set up a 2-D $(r + z)$ grid and place our representative particles in the grid cells. The grid cells are assumed to be annuli at a given distance from the star $\{r, r + \Delta r\}$ and height above the midplane $\{z, z + \Delta z\}$. Only particles present inside the same annulus are allowed to collide with each other.

To construct the annuli we developed an adaptive grid routine. The volume of the grid cells varies in order to keep the number of the swarms per cell constant. This procedure is illustrated in Fig. 2.1. In order to set up the grid walls, we first sort the particles by their radial positions. We choose the positions of the vertical walls such that the number of swarms in each radial zone is the same. Then we sort the particles by their vertical positions within every radial zone individually and set up the horizontal walls in order to preserve equal number of swarms in each cell.

Thanks to this approach, we automatically gain higher spatial resolution in the important high dust density regions. Furthermore, keeping the number of the representative particles in one cell constant assures that we always have a sufficient amount of bodies to resolve the physics of the coagulation kernel properly (see Sect. 2.3.1).

As the Monte Carlo algorithm is generally an $O(n^2)$ method, the adaptive grid routine helps us to optimize the computational cost of performing the collisions by a significant factor.

RELATIVE VELOCITIES

As in e.g. [Birnstiel et al. \(2010\)](#), we consider five sources of relative velocities between the dust particles: namely the Brownian motion, turbulence, radial and azimuthal drift as well as differential settling. For the turbulent relative velocities we follow the prescription given by [Ormel & Cuzzi \(2007\)](#).

For calculation of the relative velocities, all the particles are assumed to be in the center of the cell. Due to this, we avoid nonphysically high collision velocities that could occur e.g. In case of a big cell with one particle placed on significantly higher height above the midplane z than the other one. In such a situation, the relative velocity calculated on a basis of Eq. (2.12) is dominated by the difference of the height z . In reality, at the moment of the collision, z is identical for both particles and the relative velocity is set up by the difference of the Stokes numbers.

2.2.5 TIME STEP

In order to resolve both advection and coagulation of the dust particles properly, a limit to the time step of the code is required. A drifting particle should be allowed to interact with every other particle along its way, thus it cannot "jump over" any cell. We implement an adaptive time-stepping method. We limit the time step according to the Courant condition:

$$\Delta t^x < \frac{\Delta x_{\min}}{v_{\max}^x}, \quad (2.25)$$

where x can be both r and z , as we apply this condition to both directions and we finally choose $\Delta t = \min(\Delta t^r, \Delta t^z)$. Δx_{\min} is the length of the shortest cell in the given direction and v_{\max}^x is the drift velocity of the fastest particle in this direction. The final time step we obtain is typically of the order of a fraction of the local orbital period.

Generally, the time step should be limited also by the dust growth timescale. However, in typical cases, the advection timescale is shorter than the growth timescale. This means that within one advection time step, the coagulation does not change the drift properties significantly.

2.3 TEST CASES

In order to validate our code, we perform a set of different tests. We test the advective and collisional parts of the code separately as well as both of them together. In this section we present some of the more educational test results.

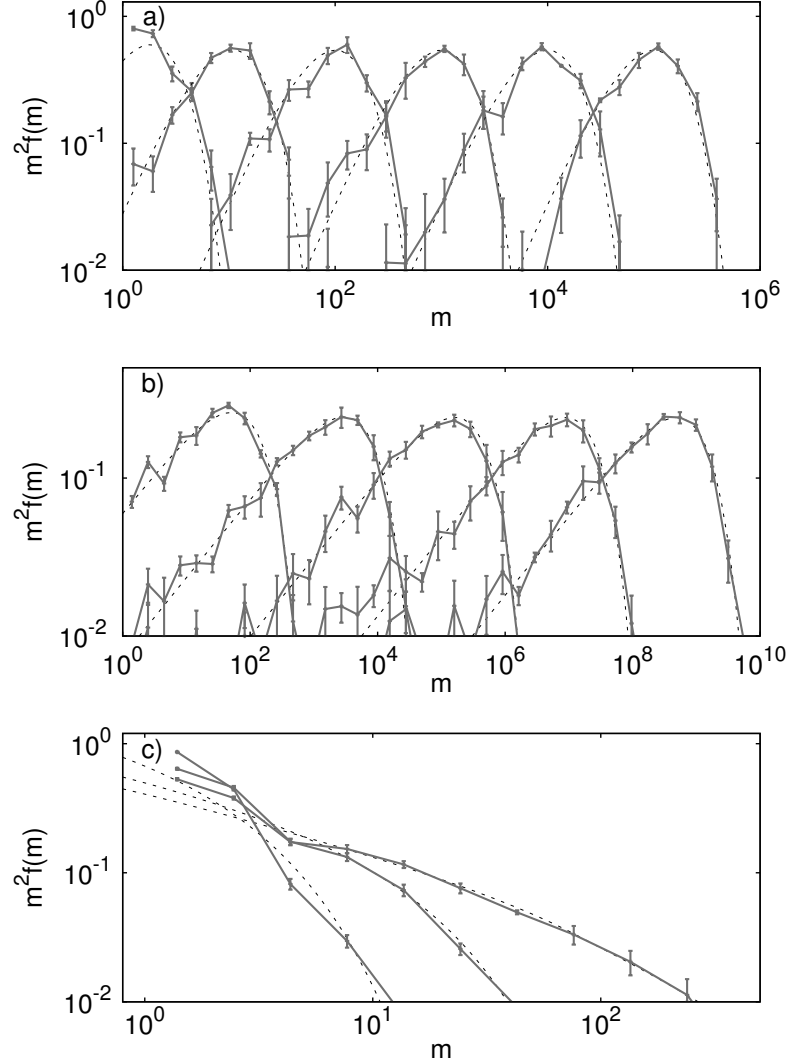


Figure 2.2: The grains mass distribution for the tests against the analytical solutions of the Smoluchowski equations (dashed lines) at different time instants: a) Test against the constant kernel $K_{ik} = 1$, where 50 representative particles are simulated five times. The particles masses are binned and the distribution functions are averaged at dimensionless times $t = 1, 10, 10^2, 10^3, 10^4, 10^5$. b) Test against the linear kernel $K_{ik} = \frac{1}{2}(m_i + m_k)$. There are 150 particles used and the simulation is repeated five times. The distribution function is produced at times $t = 4, 8, 12, 16, 20$. c) Test against the product kernel $K_{ik} = m_i \times m_k$. We use 400 representative particles and repeat the simulation ten times. The outputs are produced at times $t = 0.4, 0.7, 0.9$.

2.3.1 TESTS OF THE COAGULATION MODEL

We test our implementation of the Monte Carlo coagulation method with the representative particle approach. In a 0-dimensional case, the only property of particles is their mass. In such case, the coagulation can be described by the Smoluchowski equation (Smoluchowski 1916, Eq. 1.41). For some coagulation kernels K_{ik} , one can find analytical solution of the Smoluchowski equation. We test our approach against three such kernels, namely the constant kernel $K_{ik} = 1$, the linear kernel $K_{ik} = \frac{1}{2}(m_i + m_k)$ and the product kernel $K_{ik} = m_i \times m_k$. The tests results are presented in Fig. 2.2. We start all the simulations with a homogeneous mass distribution of particles with $m_0 = 1$. The volume density of particles is also equal to unity. The analytical solutions are obtained from Silk & Takahashi (1979) and Wetherill (1990).

We necessarily get similar results as Zsom & Dullemond (2008). We find that the constant kernel can be properly resolved using a very limited number of representative particles. The linear kernel is possible to resolve using at least 100 representative particles. To obtain proper evolution in the case of the product kernel we need about 300 particles. As the mass dependence of the coagulation kernel in physical cases usually lies between the linear and product kernels, we conclude that we should use at least 200 representative particles per cell in our simulations. Thanks to the adaptive grid routine, it is possible to fulfill this requirement at any time during the simulation.

2.3.2 VERTICAL SETTLING AND TURBULENT DIFFUSION OF THE PARTICLES

In the case of absence of the radial drift and coagulation, the vertical structure of dust is modulated by the vertical settling and turbulent diffusion. From the test simulations, we obtain a Gaussian distribution defined by local properties of gas and solids. Its width can be derived comparing the timescales of the vertical settling and turbulent diffusion.

The timescale of the vertical settling can be obtained from Eq. (2.12) as

$$\tau_{\text{sett}} \approx \frac{1}{\Omega_K \min(0.5, \text{St})}, \quad (2.26)$$

The timescale of the turbulent diffusion can be estimated as

$$\tau_{\text{diff}} \approx \frac{L^2}{D_d}, \quad (2.27)$$

where the L is a length scale over which the diffusion takes place and the D_d is defined by Eq. (2.14). Comparing Eqs. (2.27) and (2.26) and transforming

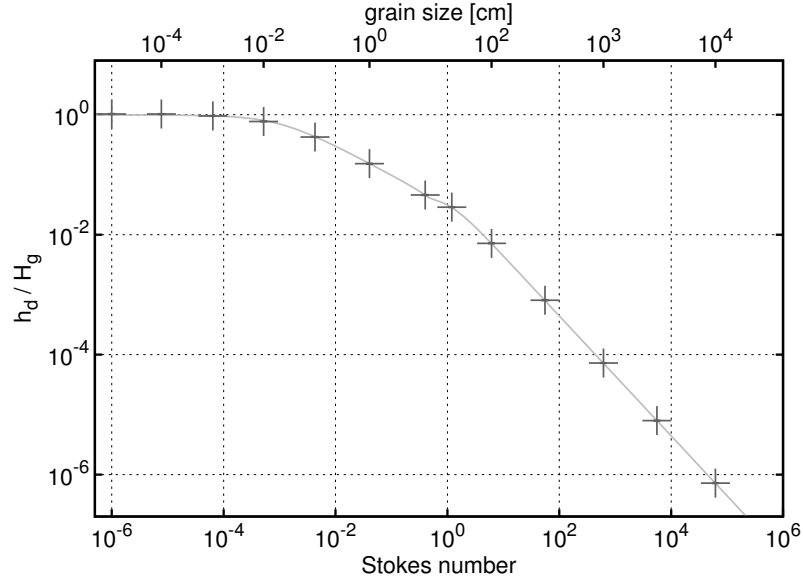


Figure 2.3: The results of the vertical settling and turbulent diffusion test. The theoretical dependence given by Eq. (2.29) is plotted with the solid line. The change of the slope around $St = 0.5$ comes from the Stokes number restriction applied in Eq. (2.12). The test simulations results are marked with points. We find a good agreement between the analytical prediction and the tests results.

the resulting formula using Eqs. (2.14) – (2.16) and taking $L = h_d$ we can estimate the thickness of the dust layer as

$$h_{d,1} = H_g \left(\frac{\alpha}{\min(0.5, St)(1 + St^2)} \right)^{1/2}. \quad (2.28)$$

The above estimate does not take the part of diffusion introduced with Eq. (2.18) into account. This effect prevents the dust layer scale height from exceeding the gas scale height. An analytical solution of the advection-diffusion equation of the gas disk gives a more accurate expression for the height of the dust layer (Dubrulle et al. 1995):

$$h_d = h_{d,1} \left[1 + \left(\frac{h_{d,1}}{H_g} \right)^2 \right]^{-1/2}. \quad (2.29)$$

We perform a set of test runs to check if the dependence given by Eq. (2.29) is reproduced by our code. We place the representative particles in a local column of a disk around a star with mass $M_\star = M_\odot$. The column is located

at $r = 1$ AU and we assume that a gas surface density $\Sigma_g = 100 \text{ g cm}^{-2}$, temperature $T_g = 200 \text{ K}$, and $\alpha = 10^{-3}$ at this location. The initial dust to gas ratio is taken to be 0.01 and the dust material density 1.6 g cm^{-3} . The gas vertical distribution is assumed to be Gaussian with the standard deviation of H_g . Initially we place the representative particles such that we get constant dust to gas ratio at every height above the midplane, so $h_{d,0} = H_g$. We use particles with sizes ranging from 10^{-5} to 10^4 cm , corresponding to the Stokes numbers range of 10^{-6} to 10^5 . The radial drift and collisions are switched off for this test. After the particle distribution reaches a steady state, we measure h_d by fitting a Gaussian. Results of the test are presented in Fig. 2.3. For each of the runs we use 10^4 representative particles distributed over 100 cells. We find a good agreement between the analytical prediction (Eq. 2.29) and the test results.

2.3.3 TRAPPING OF THE DUST PARTICLES IN A PRESSURE BUMP

The trapping of solids in a region with positive pressure gradient is a promising mechanism of overcoming the radial drift barrier and enhancing the growth of dust aggregates (Kretke & Lin 2007; Brauer et al. 2008b). It was already studied theoretically by e.g. Garaud (2007). Pinilla et al. (2012b) investigated trapping of solids in the outer regions of protoplanetary disk. They showed that disk models with pressure bumps give predicted spectral slope in the mm-wavelength range consistent with the observed for typical T-Tauri disks, contrary to disk models without the bumps.

In this section, we present a simple analytical prediction of width of the annulus formed by the trapped particles of given Stokes number and compare it to results of test runs. We use a disk model based on the work of Kretke & Lin (2007), where the α parameter varies with r due to changes in the gas ionization. As the MRI turbulent strength depends on the degree of coupling to the magnetic field, a change in the gas ionization will affect α . The gas ionization fraction depends on the total surface area of dust particles (Okuzumi 2009), and is therefore most affected if there is a significant population of small particles. Kretke & Lin (2007) assumed all particles to be μm -sized, meaning that the gas ionization rate is simply proportional to the dust to gas ratio. Beyond the snow line, the dust density steeply increases as the water vapor condenses into solid grains, causing a decrease in α that builds up a pressure bump on the disk accretion timescale. Kretke & Lin (2007) present a disk model parametrized in the framework of the α -prescription for a steady state obtained via the described mechanism. Our implementation of the model is presented in Fig. 2.4. The α parameter drops down from 10^{-3}

2.3. TEST CASES

inside the snow line to 10^{-6} in the dead zone. This causes the bump in the surface density and the change of the sign of the pressure gradient. In the region where the pressure gradient is positive, the particles drift outwards and can thus be trapped in a so-called pressure trap. [Yang & Menou \(2010\)](#) remarked that in such model the local density maximum is Rayleigh unstable if the bump width is less than the disk scale height. Therefore, we choose the parameters of the model such that the width of the gas density bump measured by fitting a Gaussian is equal to 4 times gas pressure scale height.

The estimation of the trapped dust region width $L(\text{St})$ is done in a similar way as the derivation of the $h_{\text{d},1}(\text{St})$ in the previous section. We compare the timescales of the radial drift τ_{drift} and turbulent diffusion τ_{diff} . As previously, we estimate the τ_{diff} with Eq. (2.27). We assume that to be trapped, the particle has to drift from its current location r to the position of the pressure trap r_0 . Thus, the radial drift timescale can be written as

$$\tau_{\text{drift}} = \left| \frac{r - r_0}{v_{\text{drift}}} \right|, \quad (2.30)$$

where the drift velocity v_{drift} can be obtained from Eqs. (2.7) – (2.8), and it is proportional to the pressure gradient $\partial_r P_g$. We assume that the disk is vertically isothermal, thus the gas pressure in the midplane is given by ([Kretke & Lin 2007](#))

$$P_g = \frac{\Sigma_g c_s \Omega_K}{2\pi}. \quad (2.31)$$

In order to obtain the $L(\text{St})$, we want to get rid of the radial dependence of τ_{drift} . Thus, we approximate the pressure profile $P_g(r)$ with the second order Taylor expansion around the location of the pressure bump r_0 :

$$P_g(r) \approx P_g(r_0) + \frac{1}{2} \frac{d^2 P_g}{dr^2}(r_0) \cdot (r - r_0)^2 = C - A (r - r_0)^2, \quad (2.32)$$

and we find $A \approx 2 \times 10^{-28} \text{ g cm}^{-3} \text{ s}^{-2}$ and $C \approx 2.6 \times 10^{-2} \text{ g cm}^{-1} \text{ s}^{-2}$ for $r_0 \approx 3.16 \text{ AU}$. The Taylor expansion is plotted with the dashed line in the panel c) of Fig. 2.4. The derivative $\partial_r P_g$, needed to calculate the v_{drift} , becomes

$$\partial_r P_g \propto -2A(r - r_0). \quad (2.33)$$

Thus, we can estimate the radial drift timescale τ_{drift} as

$$\tau_{\text{drift}} \approx \frac{\rho_g \Omega_K}{2A} \left(\text{St} + \frac{1}{\text{St}} \right). \quad (2.34)$$

Comparing Eqs. (2.27) and (2.34), using Eqs. (2.14) – (2.16), and replacing $\rho_g c_s / \Omega_K = \rho_g H_g = \Sigma_g$ we find the expression for the width of the trapped

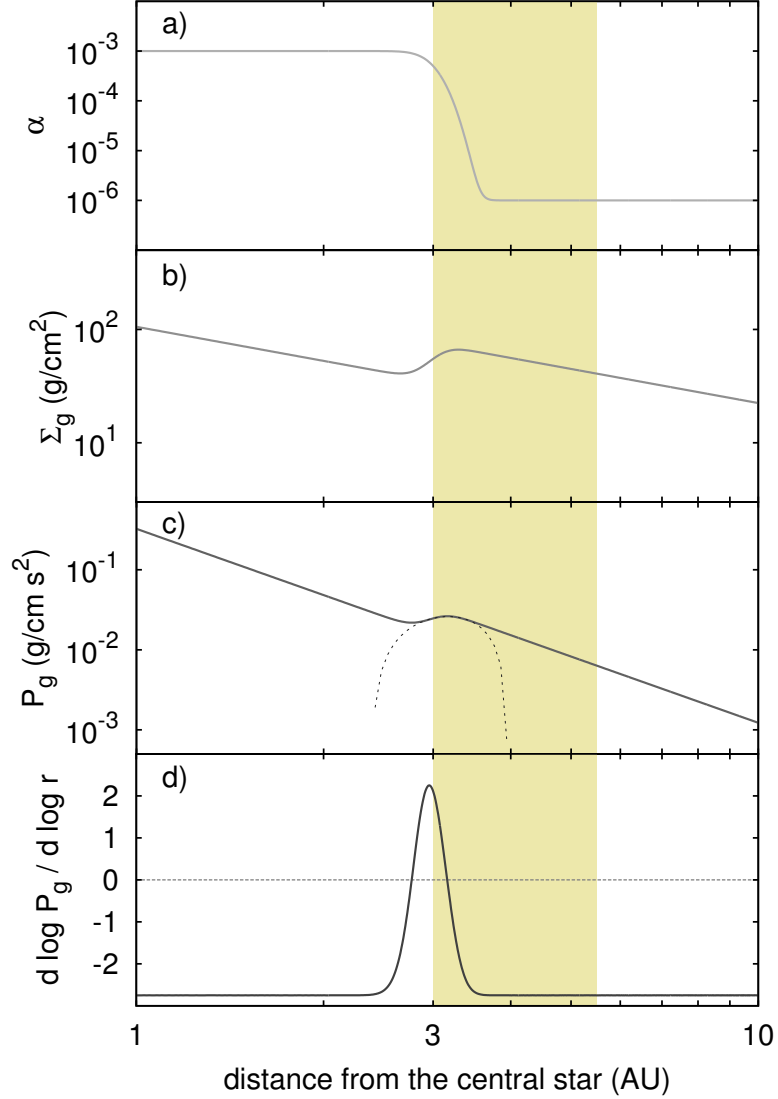


Figure 2.4: The disk model with the pressure bump near the snow line according to [Kretke & Lin \(2007\)](#). The panels show: a) the α parameter, b) gas surface density, c) gas pressure in the midplane and its Taylor expansion around the pressure bump location (Eq. (2.32), dashed line), d) gas pressure gradient, as a functions of the radial distance from the central star, for our fiducial disk model. Region highlighted with the different background color refers to models described in Chapter 3.

2.3. TEST CASES

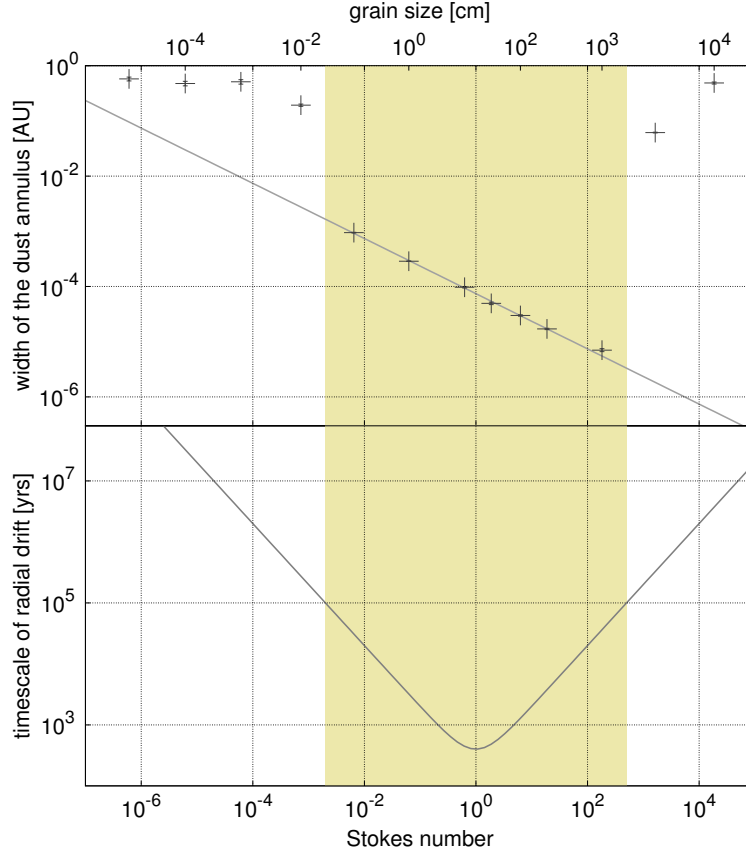


Figure 2.5: The top panel shows the analytically derived dependence for the trapped dust annulus width (Eq. 2.35, line) and the results of test runs (points). The timescale of particles trapping is associated with the timescale of radial drift. The latter is specified on the lower plot (Eq. 2.34). The points on the top panel were measured after 10^5 years of evolution. This indicates a range of Stokes numbers of particles that can be trapped (marked with different background color).

dust annulus:

$$L \approx \left(\frac{\alpha}{A} \Sigma_g c_s \Omega_K \frac{1}{St} \right)^{1/2}. \quad (2.35)$$

One can notice that the width of the annulus becomes larger with growing surface density, turbulent viscosity or temperature of the gas, consistent with intuition.

The solids are trapped on a timescale of radial drift that is specified by Eq. (2.34). The timescale is shortest for particles of $St = 1$ and grows

for both smaller and bigger sizes. We perform a set of simulations using different sizes of particles ranging from 10^{-5} to 10^4 cm. For each simulation we use 10^5 of representative particle distributed over 100 radial and 20 vertical zones. Initially the particles are placed between 3 and 4 AU. The collisions are switched off. After 10^5 yrs of evolution, the width of the bump in the dust surface density is measured by fitting Gaussian distribution. In the top panel of Fig. 2.5, the fitted standard deviation of the distribution is plotted as a function of the Stokes number, together with the fit errors. In the bottom panel, the timescale of radial drift is shown. The range of Stokes numbers for that the timescale is shorter than 10^5 yrs is indicated with different background color. The width of the trapped dust annulus on the top panel is consistent with the dependence given by Eq. (2.35), but only for the particles in the range specified by the short enough timescale condition. This result is perfectly in agreement with our predictions.

In this test we neglect the radial drift velocity caused by gas accretion, specified by Eq. (2.6). Pinilla et al. (2012a) showed that if we do not neglect this effect, we get additional restriction for size of particles that can be trapped (their Eq. 11). Particles with Stokes number smaller than St_{crit} are not trapped because their coupling to gas is so strong that they move with the gas through the pressure maximum, where

$$St_{\text{crit}} = -\frac{v_{\text{g}}^{\text{r}}}{\partial_{\text{r}}P_{\text{g}}}\rho_{\text{g}}\Omega_{\text{K}}, \quad (2.36)$$

with v_{g}^{r} as the radial velocity of gas. This condition holds only when the other component of the dust radial velocity is positive, i.e. $\partial_{\text{r}}P_{\text{g}} > 0$. In our model $St_{\text{crit}} \approx 10^{-4}$, so this effect would not change the test result.

2.3.4 SEDIMENTATION DRIVEN COAGULATION

The Gaussian vertical structure of the dust as described in Sect. 2.3.2 is usually a good approximation in the case of protoplanetary disk. However, it can be strongly affected by collisional evolution of the aggregates.

We investigate the growth of the dust aggregates in a 1-D vertical column. We base on a model presented by Dullemond & Dominik (2005) and reproduced by Zsom et al. (2011a) (henceforth ZsD11). The column is placed at the distance $r = 1$ AU from the star of mass $M_{\star} = 0.5M_{\odot}$, with a gas surface density $\Sigma_{\text{g}} = 100 \text{ g cm}^{-2}$ and a gas temperature $T_{\text{g}} = 200 \text{ K}$. The radial drift is switched off. The dust particles are initially equal size monomers with radii $a_0 = 0.55 \text{ }\mu\text{m}$ and material density $\rho_{\text{p}} = 1.6 \text{ g cm}^{-3}$. They are initially vertically distributed such that the dust to gas ratio $\rho_{\text{d}}/\rho_{\text{g}} = 0.01$ is constant along the column. Fragmentation is not included in this model, i.e.

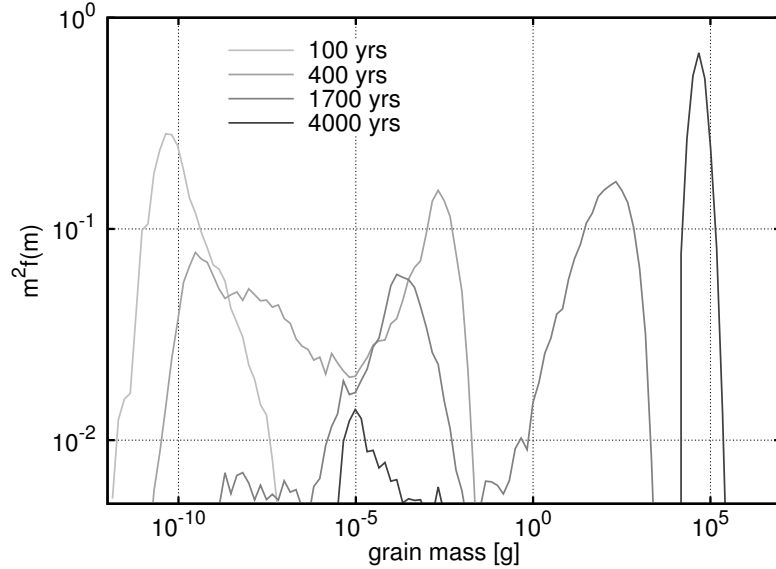


Figure 2.6: Vertically integrated dust mass distribution at different stages of evolution for the sedimentation driven coagulation test. After approximately 400 yrs, the dust distribution splits into two parts. The big aggregates continue to grow at the expense of the small particles.

the particles collisions result in sticking for every collision energy. The growth is driven only by Brownian motion and differential settling. We ignore other sources of relative velocity: radial and azimuthal drift as well as turbulence. For the test we used 5×10^4 representative particles and 100 cells (500 particles per cell). The test run took about 48 hours on an 8 core 3.1 GHz AMD processor.

Similar to [Dullemond & Dominik \(2005\)](#) and ZsD11, we notice that initially the growth is slow, driven by the Brownian motions, and proceeds faster closer to the midplane, where the matter density is highest. At $t \approx 100$ yrs, the particle growth in the upper layers speeds up as the differential settling comes into play. The value of the vertical settling velocity increases with height, as can be noticed from Eq. (2.12). The aggregates grow and settle down simultaneously. The first rain-out particles that reach the midplane have masses of around 10^{-2} g.

Fig. 2.6 presents the mass distribution evolution obtained in this test. It can be noticed that within the first 400 years the dust distribution becomes bimodal. One population consists of the rain-out particles, which reached the midplane, and the other one are the smaller aggregates, which remain vertically dispersed. The bigger particles grow at the expense of the small

ones, thus the surface density of the latter decreases. The final mass of the biggest aggregates is $\sim 10^6$ g. Such a bimodal dust distribution for sedimentation driven coagulation was also reported by [Dullemond & Dominik \(2005\)](#) and [Tanaka et al. \(2005\)](#).

The numerical model used by ZsD11 is practically identical to ours, but the spatial grid is fixed and consists of equally spaced cells, while in our case we use the adaptive grid method. They use 40 cells to resolve 4 gas pressure scale heights. We notice that in comparison to their results, we get a faster evolution of the dust. The first rain-out particles arrive to the midplane after approximately 400 yrs of evolution, instead of 500 yrs reported by ZsD11. We observe also that the growth proceeds to bigger sizes than in ZsD11, where the growth stalls at approximately 10^{-1} g.

In order to explain the discrepancy of the results obtained by ZsD11 and us, we perform resolution test. As the adaptive grid reflects a very high number of cells in high density regions, we investigate if the result obtained by ZsD11 depends on the number of cells used. Therefore, we perform a set of simulation with constant, equally spaced grid but increasing the number of cells. Fig. 2.7 presents the mass-height distribution of the dust after 1000 yrs of evolution for the constant grid with 80, 240 and 640 cells as well as for the adaptive gridding with 100 cells. Note that ZsD11 modeled only the upper half of the column, so their 40 cells is equivalent to our 80 cells resolution. We find that the timescale of the evolution is indeed dependent on the vertical resolution. With the adaptive grid method, we are also able to see the effect of sweeping up of the small particles by the big ones on the dust distribution around the midplane (see the bottom panel of Fig. 2.7).

If we consider one grid cell with a bottom wall at $z = 0$, using the model described in this section, the collision rate defined by Eqs. (2.19) – (2.20) does not depend directly on the height above the midplane of the center of the cell z_c . The relative velocity Δv is dominated by the differential settling velocity that is directly proportional to z_c . Also the cell volume V is directly proportional to z_c . Therefore, one could expect that the collisional evolution does not depend on the vertical resolution we choose. However, we find that the higher resolution we use, the faster the growth and settling proceed. This effect can be explained in the following way: we calculate the relative velocities of particles basing on the physical values obtained in the centers of the cells. Thus, the exact values of gas density, Stokes numbers and vertical settling velocities depend on the exact choice of the location of the cell. All these values influence the collision rate of particles. The more cells we use, the closer to the midplane (where the growth proceeds fastest at the very beginning as well as at the end of the evolution) we are able to resolve. On the other hand, the faster growth we obtain, the quicker the particles settle

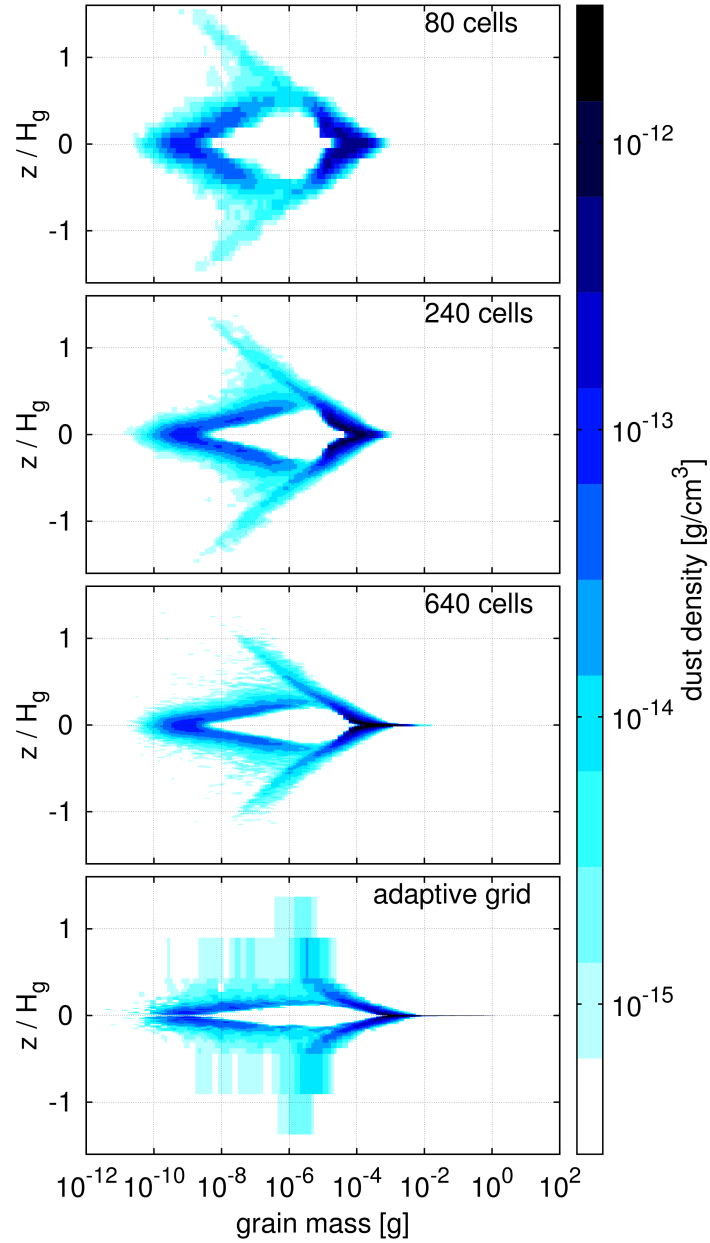


Figure 2.7: The vertical distribution of the dust grains of different sizes for the 1-D sedimentation driven coagulation test. The three upper panels show the result of simulations with constant grid with growing number of cells. The bottom panel uses the adaptive grid routine described in this work with 100 cells. All the distributions were plotted after 1000 yrs of the evolution. The numerical convergence of results is noticeable.

down.

It is worth noting, that one of the basic assumptions of the method we use (Zsom & Dullemond 2008) is that the particles are homogeneously distributed over the volume of the cell within they can collide. If we do not assure sufficiently high spatial resolution, this assumption is broken, and the model leads to nonphysical results.

The vertical resolution defines the maximum dust to gas ratio we are able to obtain. In the case of constant grid with the number N_c of cells the maximum dust to gas ratio $\rho_d/\rho_g = N_c \times 0.01$ would occur if we place all of the dust particles in one cell. The 0.01 is the global dust to gas mass ratio. In the case of the adaptive grid the dependence on the number of cells is much weaker, and we are able to resolve higher dust to gas ratios with much lower number of cells.

The impact of the dust layer width on the growth was investigated by Nakagawa et al. (1986). They concluded that the growth terminates for an infinitely thin layer, as when all of the bodies are located at $z = 0$ the vertical velocity of dust resulting from Eq. (2.12) $v_d^z = 0$, and the main source of the relative velocities driving the collisions vanishes. However, even with the adaptive grid, we can never obtain an infinitely small cell, so the growth termination does not occur in our simulations.

The existence of such an infinitely thin dust layer is unrealistic anyway. As soon as the dust to gas ratio exceeds unity, the shear instabilities (Weidenschilling 1980; Cuzzi et al. 1993), in particular the Kelvin-Helmholtz instability (Johansen et al. 2006) are known to occur. Bai & Stone (2010a) showed that in the case of no turbulence, another kind of hydrodynamic instability, namely the streaming instability (Youdin & Goodman 2005), will generate a turbulence and maintain the dust to gas ratio before the Kelvin-Helmholtz instability could be triggered. It then prevents the dust from further settling and the growth from terminating.

With the adaptive grid routine, we are able to resolve the dust to gas ratio much higher than one. To avoid such a nonphysical situation, we implement an artificial α viscosity, α_{SI} , that is designed to mimic the impact of the streaming instability on the vertical distribution of dust. We calculate the α_{SI} as

$$\alpha_{\text{SI}} = \alpha_{\text{SI,max}} \left[1 + \operatorname{erf} \left(\frac{\rho_d/\rho_g - c_1}{c_2} \right) \right], \quad (2.37)$$

where $\alpha_{\text{SI,max}}$ defines a minimal turbulent viscosity that we need to maintain dust to gas ratio lower than one and the c_1 , c_2 are parameters of the error function erf. The $\alpha_{\text{SI,max}}$ can be calculated from Eq. (2.29) as

$$\alpha_{\text{SI,max}} = Z_0^2 \min(0.5, \bar{\text{St}}) \left(1 + \bar{\text{St}}^2 \right), \quad (2.38)$$

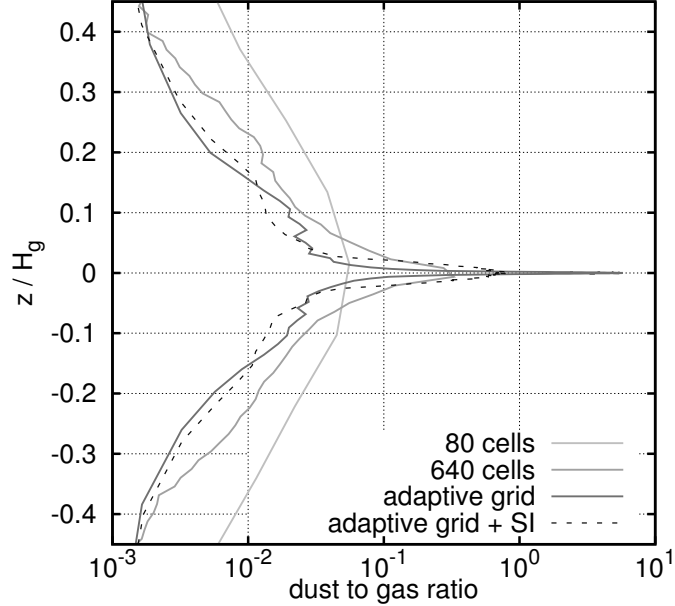


Figure 2.8: The dust to gas ratio around the midplane after 1000 yrs of evolution as resolved by different algorithms: constant grid with 80 and 640 cells and the adaptive grid with 100 cells with and without the streaming instability (SI). The obtained dust to gas ratio depends strongly on the vertical resolution. In the case of the adaptive grid it exceeds unity. The implementation of the streaming instability lowers the dust to gas ratio only in the region in that such a nonphysical value occurs.

with Z_0 representing initial dust to gas ratio, and \bar{St} being the Stokes number averaged over all particles present in given cell, as the strength of the streaming instability driven turbulence is determined by the collective property of the particles. The form of Eq. (2.37) was chosen such that the additional term of viscosity is nonzero only when the dust to gas ratio exceeds unity and it adds only the amount of turbulence that is needed to maintain the dust to gas ratio below the nonphysical value. A more accurate prescription for the α_{SI} can be found in Chapter 5.

The Fig. 2.8 shows the dust to gas ratio at different heights above the midplane after 1000 yrs of evolution for the different resolutions and for the test with the artificial viscosity introduced by the α_{SI} . The resolution dependence can be noticed. The dust to gas ratio in the case of the adaptive grid exceeds unity. The implementation of the α_{SI} changes the dust to gas ratio only very close to the midplane.

We find that implementing such an additional turbulence source speeds

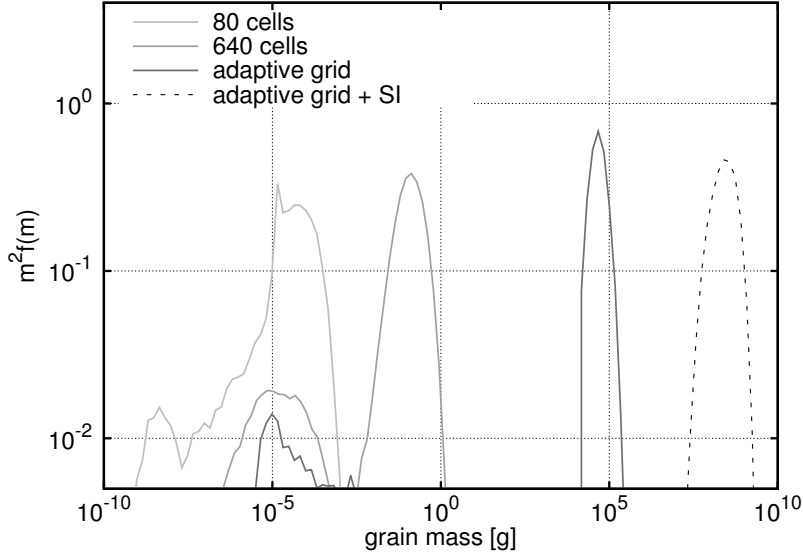


Figure 2.9: The dust mass distribution after 4000 yrs of evolution for the tests with the constant grid with 80 and 640 cells and adaptive gridding with 100 cells with and without the streaming instability (SI) implemented. The figure reveals a huge impact of the vertical resolution on the dust growth timescale. With the adaptive gridding we obtain much bigger bodies after the same time of evolution. Taking the SI into account additionally speeds up the growth.

up the coagulation of the big particles. This is because it increases the relative velocities of the bodies and thus the collision rates. As we ignore the possibility of the aggregates fragmentation, the higher relative velocities result in faster growth.

The Fig. 2.9 shows the mass distributions after 4000 yrs of evolution obtained for different gridding as well as with and without the streaming instability (SI). This figure reveals how much the growth depends on the resolution. The mass of the biggest agglomerates obtained after 4000 yrs in the test with 640 constant cells and 100 adaptive grid cells varies by five orders of magnitude. This is however a timescale effect. If we wait long enough, which is of the order of Myrs for the constant grid, we will obtain the same resulting size of agglomerates. The growth can proceed only until all the small particles are swept up by the big ones.

The consideration of the streaming instability allows us to obtain another 4 orders of magnitude in mass larger particles. The additional viscosity increases the vertical extent of the big bodies as well as their relative veloci-

ties. Thus, they are able to collide with the small particles that reside higher above the midplane. This speed up of the growth can however be a result of the simplified instability implementation we used. We do not account for the strong particle clumping reported for the streaming instability (Johansen et al. 2009b). We ignore also the possibility of the gravitational instability of the clumps (Johansen et al. 2007). We include these effects in Chapter 5.

The growth timescale dependence on the vertical resolution revealed in these sections can have a huge impact on dust evolution models. In 2-D cases the impact of vertical structure resolution is even stronger as the relative velocity is dominated by the radial and azimuthal drift. Its value does not depend on the vertical position, so the collision rate becomes explicitly dependent on z .

In the model presented here, turbulence is not included, besides the one generated by the streaming instability. We ignore also the possibility of the aggregates fragmentation. We expect that including these effects would lower the discrepancy between the results obtained using the constant and adaptive gridding. The turbulent mixing prevents the high dust to gas ratio, which is problematic for the constant grid scheme. Taking the fragmentation into account sets up a maximum mass over which the particles cannot grow. Thus, the difference in the growth timescale does not change the maximum size of particles after the same time of evolution obtained in the different models.

The tests presented in this section have proven our adaptive grid to deal very well with the high dust density regions. However, as can be observed on the bottom panel of Fig. 2.7, the low density regions are resolved much worse. As the most of the coagulation happens in the high density regions around the midplane, this flaw should not effect the mass distribution function evolution. However, it may limit the possibilities of using our code in context of the protoplanetary disks observations.

2.4 SUMMARY

We developed a new computational model for dust evolution in the protoplanetary disk. The representative particles method (Zsom & Dullemond 2008) has been used to describe the dust. The gas disk has been included in an analytical way. The model tracks the dust drift as well as the coagulation. The Monte Carlo method has been used to investigate the collisions between the dust aggregates. The code is a further development of the work presented by Zsom et al. (2011a). We extended the model of Zsom et al. (2011a) by adding an adaptive gridding method, which assures high spatial resolution in high dust density regions, as well as the radial dimension.

With the new numerical code, we found that high spatial resolution is

necessary to model the dust evolution properly. In particular, in the case of lack of turbulent mixing, when a dense midplane layer is formed, the dust growth timescale depends on the resolution very strongly.

A great difficulty in the planet formation modeling is that the dynamic range involved is too wide to be covered by a single numerical method. When km-sized bodies are formed, regardless of their formation process, the gravitational interactions become important and the N-body dynamics needs to be considered. Statistical approach, which is commonly used to study the dust coagulation, is very hard to connect with the N-body methods, as it only handles the dust distribution function and it does not consider individual particles. In our code, we used the representative particles as a description for dust, thus the connection to the N-body regime is more natural. The code presented in this chapter is a very first step towards a complete model of the planet formation.

The main conclusions of this chapter can be summarized in the following points:

- Adaptive gridding allows us to investigate the dust collisional evolution with Monte Carlo method in 2-D. It assures sufficient spatial as well as mass resolution to account for the dust structure. It automatically moves the computational effort towards the high dust density regions.
- Proper resolution of the vertical structure of protoplanetary disk is important for obtaining a correct dust growth timescale. This is true especially in the case of low turbulence.

Scientific applications of the new code are described in the following chapters. In Chapter 3, we investigate the possibility of planetesimal formation via sweep-up growth at the inner edge of dead zone by performing 2-D models involving collision scheme with sticking, bouncing, fragmentation, and mass transfer. In Chapter 4, we implement the impact velocity distribution that also enables planetesimal formation via sweep-up growth and perform a direct comparison of the results obtained with the code and with a Smoluchowski equation solver. In Chapter 5, we extend the code by adding a possibility of planetesimal formation via the streaming instability.

2.4. SUMMARY

PLANETESIMAL FORMATION AT THE INNER EDGE OF DEAD ZONES

*Adapted from Drążkowska, Windmark & Dullemond, 2013, A&A, 556, A37
and Drążkowska, Windmark & Dullemond, 2013, poster presented at PPVI¹*

3.1 INTRODUCTION

Despite decades of research, planet formation is still not fully understood. At the point of formation, the protoplanetary disk is thought to contain submicron dust grains. The formation of planetesimals out of these grains is one of the more uncertain aspects in the theory of planet formation, since the growth of large dust particles by subsequent sticking collisions is very difficult to obtain in realistic models. Such a simple particle aggregation has been shown to encounter numerous obstacles, such as the electrostatic barrier (Okuzumi et al. 2011b), the bouncing barrier (Zsom et al. 2010), the fragmentation barrier (Blum & Münch 1993), and the radial drift barrier (Weidenschilling 1977a). The relative velocities of dust particles, which are regulated by their interaction with gas, have been found to be too high to allow sticking of aggregates as small as millimeters. On the other hand, even if there is a way to grow meter-sized bodies, they are going to be lost inside of an evaporation line within a few hundred years due to the radial drift.

Some solutions to these problems have been suggested in recent years. The sticking properties of ices are claimed to be much better than those of silicates (Wada et al. 2009), leading to ice grains capable of forming highly porous aggregates. Including this property in models has been shown to let the particles avoid the radial drift barrier (Okuzumi et al. 2012). However, the collisional properties of the ice particles are still rather uncertain, because of the difficulties in conducting the laboratory experiments. There is much more laboratory data concerning the collisional physics of the silicates (Güttler et al. 2010), although even the silicate collisional properties remain an extensively discussed topic. Recent experiments have revealed a smooth

¹See page ix for the authorship details.

transition between sticking and bouncing behavior (Langkowski et al. 2008; Weidling et al. 2012; Kothe et al. 2013), but numerical molecular dynamics simulations predict no or significantly less bouncing (Wada et al. 2011; Seizinger & Kley 2013). At still higher collision velocities, particles are expected to fragment, but if the mass ratio is high enough, growth via mass transfer is also a possibility (Wurm et al. 2005; Teiser & Wurm 2009; Kothe et al. 2010; Beitz et al. 2011).

The relative velocity of collision between the aggregates are usually calculated on the basis of a mean turbulence model, where two particles with given masses m_1 and m_2 always collide at the same relative velocity $\Delta v(m_1, m_2)$. Considering a probability distribution function $P(\Delta v|m_1, m_2)$ and the sweep-up by the mass transfer is another possibility of overcoming the growth barriers (Windmark et al. 2012b; Garaud et al. 2013). However, as the exact nature of the probability distribution is unknown, it is not certain if this effect can indeed allow the planetesimal growth. The combined action of hydrodynamic and gravitational instabilities (Goodman & Pindor 2000; Johansen et al. 2007) is an alternative scenario for the formation of planetesimals. The radial drift barrier can be overcome by taking local disk inhomogeneities into account that lead to the pressure gradient change (pressure bumps) and suppress of the inward drift of bodies (Whipple 1972; Barge & Sommeria 1995; Klahr & Henning 1997; Alexander & Armitage 2007; Garaud 2007; Kretke & Lin 2007).

3.2 MOTIVATION

In the test models presented in Chapter 2, we have always assumed perfect sticking between particles, and ignored all other possible collision outcomes. However, collisional physics of dust aggregates is highly complex, and laboratory experiments have shown that also effects such as bouncing, fragmentation and erosion can occur (Blum & Wurm 2008). By implementing the collision scheme proposed by Güttler et al. (2010) in 0-D simulations, Zsom et al. (2010) showed the importance of using a realistic collision model, and discovered the existence of the bouncing barrier, where growth-neutral bouncing collisions can completely prevent particle growth above millimeter-sizes, even before the fragmentation barrier is reached.

Windmark et al. (2012a) showed that the existence of a collisional growth barrier (such as the bouncing barrier) can actually be beneficial for the growth of planetesimals. If some larger particles, or *seeds*, are artificially introduced into a 0-D model, they can grow by sweeping up the population of particles kept small by the bouncing barrier, thanks to the mass transfer effect observed by Wurm et al. (2005). When two large particles collide

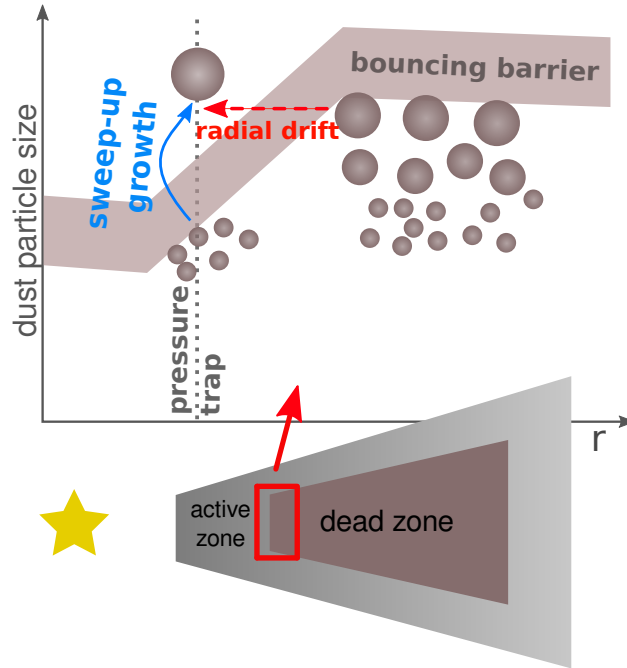


Figure 3.1: Sketch of the planetesimal formation mechanism we suggest. Thanks to the radial variation in turbulence efficiency, the position of the collision regimes is shifted in terms of particle size. The dust aggregates can grow to larger sizes in the dead zone than in the MRI active zone. The "big" particles grown in the dead zone drift inwards through the bouncing regime, to the location of the pressure trap, and some of them can continue to grow via sweeping up the small particles halted by the bouncing barrier.

at a high velocity, they tend to fragment, but if the mass ratio between the colliding particles is high enough, only the smaller of the two will be disrupted, depositing a fraction of its mass onto the larger particle in the process. In this way, two populations of particles are formed, where the few seeds grown by sweeping up the small particles while colliding only rarely between themselves. [Windmark et al. \(2012b\)](#) and [Garaud et al. \(2013\)](#) showed that the first seeds might be formed by including velocity distributions produced by stochastic turbulence, but the exact nature of these distributions, and whether the effect is capable of producing high enough mass ratios, is still unclear.

In this study, we investigate whether the seeds can be produced at one location in the disk and then transported by the radial drift to another region, where they are significantly larger than the grains produced locally. This could allow them to grow further by sweeping up the smaller grains.

3.3. SIMULATION SETUP

In particular, we postulate that such a situation can occur for a sharp α change, e.g. at the inner edge of a dead zone.

Figure 3.1 shows the basic idea behind our model. At the inner edge of the dead zone, strength of the MRI turbulence drops, affecting the relative velocities between dust particles. In the MRI active region, the turbulence is stronger than in the dead zone, causing bouncing to occur for significantly smaller particles. Thus, aggregates growing in the dead zone can reach larger sizes. The radial drift (that increases toward the Stokes number equal unity) can transport the largest particles to the MRI active region, and at the same time into another collisional regime. The drifting particles have now become seeds, and can continue to grow by sweeping up the small grains stuck below the bouncing barrier. Furthermore, the rapid turbulence strength decline can result in a formation of a pressure trap that allows the seeds to avoid further inward drift and becoming lost inside of the evaporation radius of the star.

A difficulty in the planetesimal formation by sweep-up growth scenario is that the first seed particles have to be orders of magnitude more massive than the main population, and that if too many such seeds are formed, they will fragment among themselves too often to be able to grow. As a first application of our 2-D code presented in Chapter 2, we investigate whether the planetesimal formation via the mechanism described above can be initiated in a realistic protoplanetary disk.

This chapter is organized as follows. In Sect. 3.3, we describe the simulation setup used in our models. We present their results in Sect. 3.4. We discuss and summarize the results in Sect. 3.5.

3.3 SIMULATION SETUP

We focus on a protoplanetary disk with a pressure bump around the snow line (Kretke & Lin 2007), using the disk model presented in Sect. 2.3.3. We assume a stationary disk, which is a simplification, as the dust grains size distribution, evolution of which we model, should affect the disk structure. We discuss this issue further in Sect. 3.5. The total disk mass integrated between 0.1 and 100 AU is $0.01M_{\odot}$, and we set the mass accretion rate to $10^{-9} M_{\odot} \text{ yr}^{-1}$. Thus, our model corresponds to a low-mass, passive protoplanetary disk. We focus this study on the region around the pressure bump, between $r = 3 - 5.5$ AU, as highlighted in Fig. 2.4. At 3 AU, the disk has a gas surface density $\Sigma_g = 65 \text{ g cm}^{-3}$ and a temperature $T_g = 140 \text{ K}$. This disk model is highly simplified, especially in the outer regions, but as we focus only on the inner region, we consider it a good approximation. We also assume a stationary gas disk, since, because of the computational expense of the simulations, we only run the models for $\sim 3 \times 10^4$ yrs, which is much

shorter than the typical disk evolution timescale.

We assume an initial dust to gas ratio of 0.01, and distribute the dust mass into monomers of size $a_0 = 1 \mu\text{m}$. The internal density of the particles is set to $\rho_p = 1.6 \text{ g cm}^{-3}$. For the models presented in this study, we use over a half a million (exactly 2^{19}) representative particles and an adaptive grid resolution of 64 radial and 32 vertical zones. This gives 256 representative particles per cell, which allows us to resolve the coagulation physics properly (see Sect. 2.3.1). Each swarm represents $\sim 10^{22}$ g, corresponding to a maximum representative particle size of roughly 100 km that is obtainable without breaking the requirement that the number of representative particles must be lower than the number of physical particles in the swarm they represent. At the current stage of our project we do not reach km-sizes.

3.3.1 COLLISION MODELS

For our collision model, we use two simplified prescriptions (models A and B) for bouncing, fragmentation and mass transfer based on the work of [Windmark et al. \(2012a\)](#). In both models, we determine the sticking probability as a function of the relative velocity Δv :

$$p_s(\Delta v) = \begin{cases} 1 & \Delta v < v_s \\ 0 & \text{if } \Delta v > v_b \\ 1 - k & \text{otherwise,} \end{cases} \quad (3.1)$$

where $k = \log(1 + \Delta v - v_s) / \log(1 + v_b - v_s)$, consistent with the findings by [Weidling et al. \(2012\)](#). The smooth transition between sticking and bouncing collisions turns out to be a natural way to limit the number of potential seeds, i.e. particles that are large enough to initiate sweep-up in the dead zone.

The fragmentation probability is determined by a step function:

$$p_f(\Delta v) = \begin{cases} 0 & \text{if } \Delta v < v_f \\ 1 & \text{if } \Delta v \geq v_f, \end{cases} \quad (3.2)$$

and we let $v_s = 3 \text{ cm s}^{-1}$, $v_b = 60 \text{ cm s}^{-1}$, and $v_f = 80 \text{ cm s}^{-1}$ be the sticking, bouncing and fragmentation threshold velocities. These values correspond to

silicate grains, which are believed to be less sticky and resilient to fragmentation than icy grains that would also exist in the simulation domain. However, because of the lack of knowledge about the ice collision properties, and the uncertainty in the efficiency in sublimation and sintering at the snow line, we decide to take the pessimistic approach of using only the silicates. The v_s , v_b and v_f are here independent on particle masses and Δv , which is different from the Windmark et al. (2012a) model. This is a significant simplification coming from the code optimization reason. However, the order of magnitude of these values is consistent with the original model, thus the overall scheme of collisional evolution is preserved.

In both of the models, during a fragmenting event, the mass of both particles is distributed according the power-law $n(m) \propto m^{-9/8}$, consistent with findings by Blum & Münch (1993) as well as Güttler et al. (2010), and the representative particle is selected randomly from the fragments (see Zsom et al. (2010) for details on how this is done in the representative particles and Monte Carlo fashion).

In model B, we also include the mass transfer effect, which occurs during a fragmenting event when the particle mass ratio is high enough, namely $m_1/m_2 > m_{\text{crit}}$ ($m_1 > m_2$), where we put $m_{\text{crit}} = 10^3$. We assume a constant mass transfer efficiency of $0.8 \cdot m_2$, i.e. the more massive particle gains 80% of the mass of the smaller particle.

The collisional model developed by Windmark et al. (2012a) is much more complex than ours. In their work the mass transfer efficiency is dependent on the impact velocity. We decided to assume the mass transfer efficiency to be constant, as we are here mostly concerned at the point where sweep-up is initiated, and we do not want to model the process in detail. For the same reason we ignored the threshold between erosion and mass transfer that Windmark et al. (2012a) found to be important for the growth to planetesimal sizes.

3.4 RESULTS

In Fig. 3.2, we present the collision outcome for all particle pairs with collision model B, in the midplane, at both the location of the pressure trap (3.23 AU) and in the dead zone (3.6 AU). In the case of collision model A, the plot is similar, but the mass transfer regime is replaced by fragmentation. From the plot, we can notice that due to differences in turbulent viscosity, the bouncing and fragmentation occur at different sizes depending on the location of the disk. In the dead zone, the turbulence is extremely low, $\alpha = 10^{-6}$, compared to $\alpha \approx 10^{-4}$ at the pressure trap, and the particle growth can therefore continue to more than one order of magnitude larger sizes before the bouncing barrier halts it. This is exactly what is needed for our planetesimal

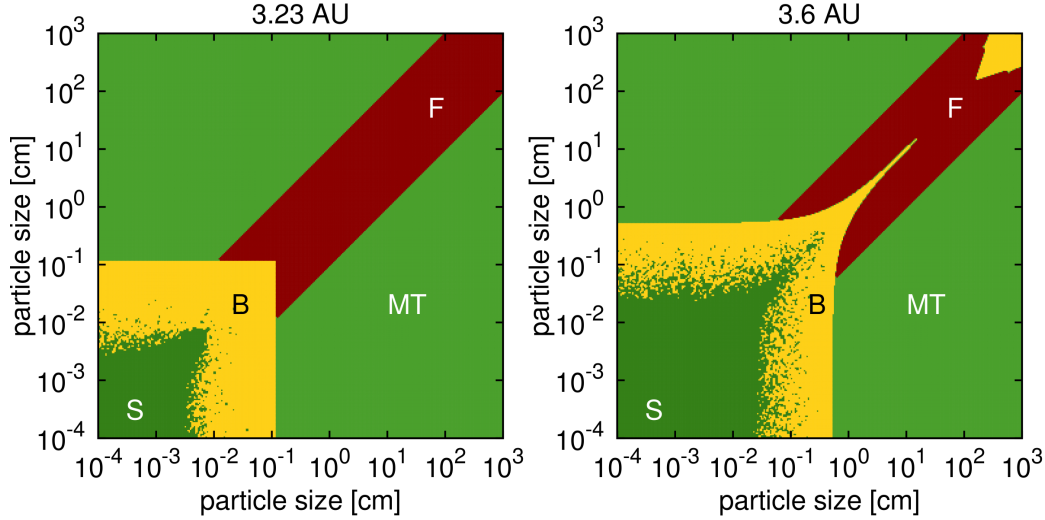


Figure 3.2: The collision outcome for particle pairs of given sizes located in the midplane at 3.23 AU (pressure trap) and at 3.6 AU (dead zone) in collision model B. "S" marks sticking, "B" bouncing, "F" fragmentation, and "MT" mass transfer. Thanks to the change in the disk properties between the two regions, the bouncing barrier occur at different particle sizes, as predicted when constructing our planetesimal formation scenario (Fig. 3.1).

formation via sweep-up mechanism to work.

In the case of collision model A, the growth is halted by the bouncing barrier at ~ 0.1 cm in the pressure trap region and ~ 0.7 cm in the dead zone, and there is no possibility that the growth could proceed towards bigger sizes. In model B, if radial drift would be ignored and the growth would only be allowed to proceed locally, the particle growth would stop at the same sizes as in model A. However, we find in our simulations that when both drift and mass transfer are included, the situation changes significantly, in a way that enables sweep-up, as discussed earlier.

The result of the simulation using collision model B is illustrated in Fig. 3.3, where we plot the vertically integrated dust density evolution at six different times between $t = 500$ yrs and $t = 30,000$ yrs. The dust growth proceeds the fastest in the inner part of the domain, where the relative velocities are the highest because of stronger turbulence. After 1,000 yrs, the particles in the inner part of the disk have reached the bouncing barrier, which efficiently halts any further growth. The position of the bouncing barrier, indicated with the dashed line in Fig. 3.3, is estimated analogically as the location of the fragmentation barrier in [Birnstiel et al. \(2011\)](#). As time progresses, particles further out also halt their growth due to bouncing. The bouncing

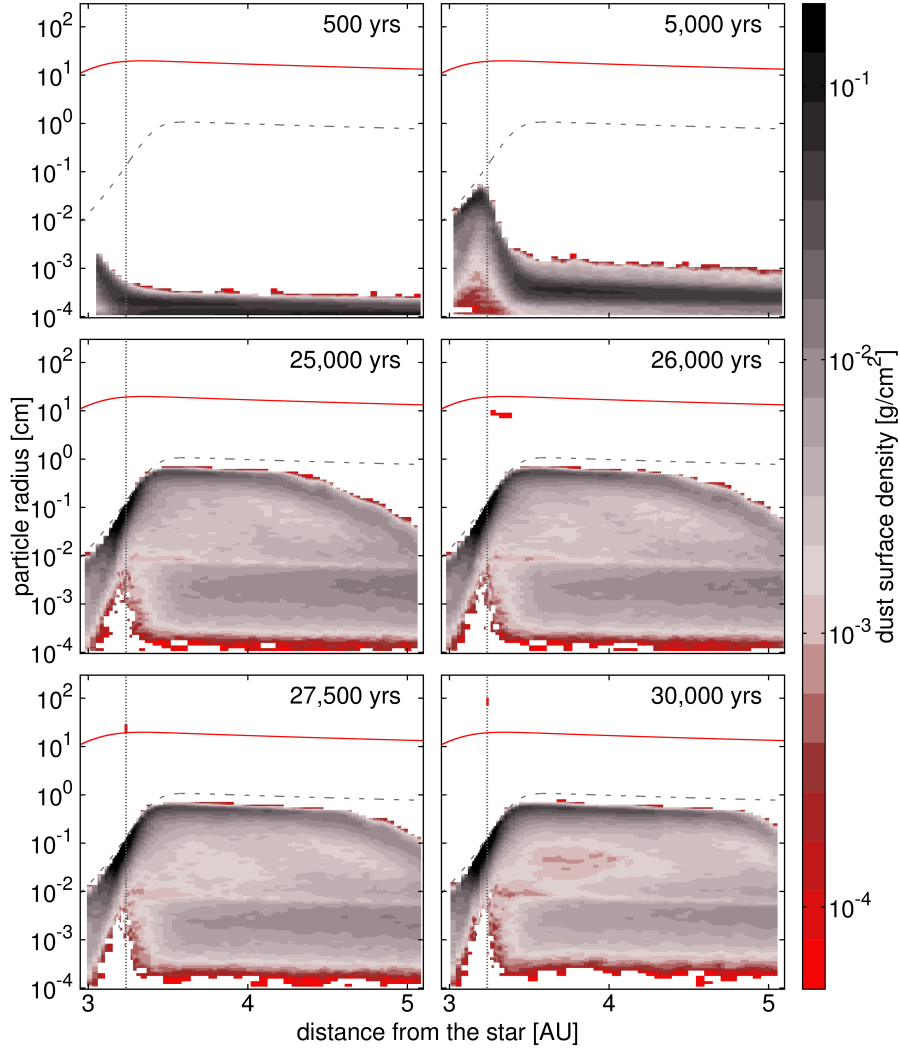


Figure 3.3: Vertically integrated dust density at different stages of the evolution, using collision model B. The red solid line shows the particle size corresponding to the Stokes number of unity, where the drift is the fastest. This line is also proportional to the gas surface density. The dashed line shows approximate position of the bouncing barrier. The dotted line indicates the location of the pressure trap. Two of the representative particles, visible as the red regions, are the particles that become the seeds and continue growing, trapped in the pressure trap at 3.23 AU, while the growth of the other swarms is stopped by the bouncing barrier. The feature at $r > 3.5$ AU and $a < 10^{-2}$ cm comes from the bimodal distribution revealed in the 1-D tests (see Sect. 2.3.4), where the small particles are vertically dispersed, while the bigger particles resides in the midplane of the disk.

barrier occurs at larger sizes in the dead zone than in the pressure trap. After 20,000 years, most of the particles are kept small by the bouncing, and only evolve by slowly drifting inwards. The size of the particles stopped by the bouncing in the dead zone corresponds to $St < 5 \times 10^{-2}$, for which the drift timescale $> 10^4$ yrs (see Fig. 2.5). Thus, the small dust is still present beyond the pressure trap at the end of the model.

During the inward drift, the particles halted by the bouncing barrier in the dead zone are automatically shifted to the fragmentation/mass transfer regime in the region of higher turbulence. Most of these particles fragment due to equal-size collisions, which can be seen in the Fig. 3.3, as the majority of the bigger particles from the dead zone is fragmented down to the position of the bouncing barrier. With these contour plots, however it is not easy to display the minute, but very important, amount of bodies that are able to cross the barrier unscathed. Thus, we choose a color palette that emphasizes low density features. The red spots that are separating from the main distribution are the seeds. The Monte Carlo method finds two such seed representative particles in the model B run.

Because of the smooth transition between sticking and bouncing, a limited number of particles manage to grow to the maximum size before they have drifted inwards. These particles have a chance to avoid the fragmenting collisions. This is because of two reasons. One of them is that the largest particles are drifting the fastest. What is more: the more massive the drifting particle is, the lower is the probability of fragmenting collision, due to the fact that the transition from fragmentation to mass transfer regime is at the projectile mass equal to 0.001 times the target mass. Thus some "lucky" particles from the higher end of the mass distribution spectrum can reach the position, where the equal-size collisions are very unlikely, as most of the surrounding particles are more than the three order of magnitude in mass lower, and so collisions will primarily lead to sweep-up growth. In our model we observe two such seeds. We check this amount in the resolution study presented in Sect. 3.4.1. After $t = 27,500$ yrs, they have reached the pressure trap, so their drift is halted, and by the end of the simulation, they have reached m-sizes.

In Fig. 3.4, we present the evolution of the spatially integrated size-distribution for model B, and Fig. 3.5 shows the evolution of the median and maximum radius of the dust particles for both models a and B. The median size illustrates the evolution of an "average" particle. Initially, both of the models evolve in the same way, and the median and maximum particle size grows gradually from μm - up to mm -sizes. After about $t = 23,000$ yrs, the largest particles in model A halt in their growth at a size of 0.7 cm due to the bouncing barrier. The median size continues to grow, as all particles

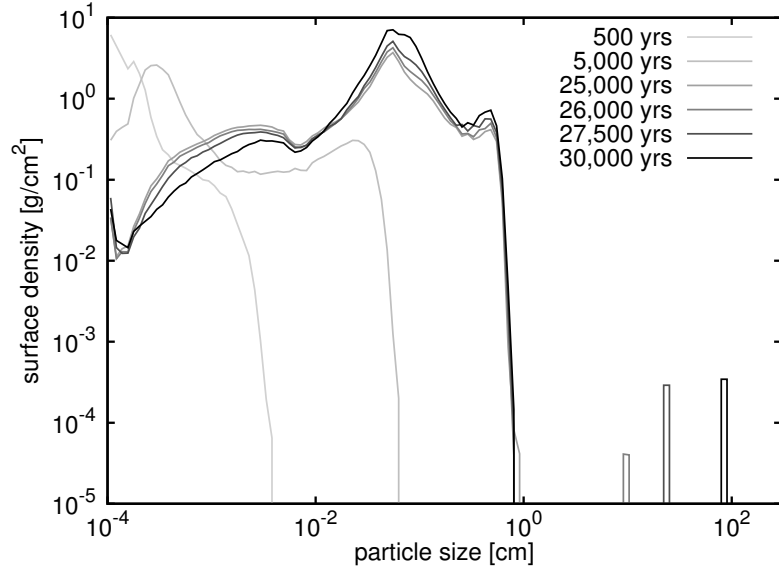


Figure 3.4: The evolution of the spatially integrated surface density of different sized particles for the model B. The particles grow until they reach the bouncing barrier. After that only a limited number of bodies continue the growth thanks to the mass transfer effect.

still have to reach the bouncing regime. In model B, however, the first seeds are formed and drifted into the pressure trap at $t = 23,000$ yrs, initiating sweep-up and causing a sudden increase in the size of the largest particles from cm- up to m-sizes. It can here be noticed that the sweep-up is only local, and the median particle size remains unchanged compared to model A. After the seeds are formed, the size-distribution becomes bimodal. As seen in Fig. 3.4, the seeds constitute a separate population, the surface density of which grows in time, as they are sweeping-up the small particles. However, as the seed population is represented by only two representative particles, its mass distribution cannot be resolved well in this model.

Fig. 3.5 shows also another interesting feature. The line corresponding to the maximum particle size in the model B exhibits two bumps before it finally jumps to depict the evolution of the growing seeds: these are some "unlucky" particles that fragmented before being able to reach the region where the mass ratio between them and the small particles is high enough to lead to mass transfer collisions. Also later in our model we observe some particles that grow a bit bigger than the others but then fragment. Of course, there can and should be some new "lucky" seeds formed later, in particular from the particles that started their evolution further away in the disk. However,

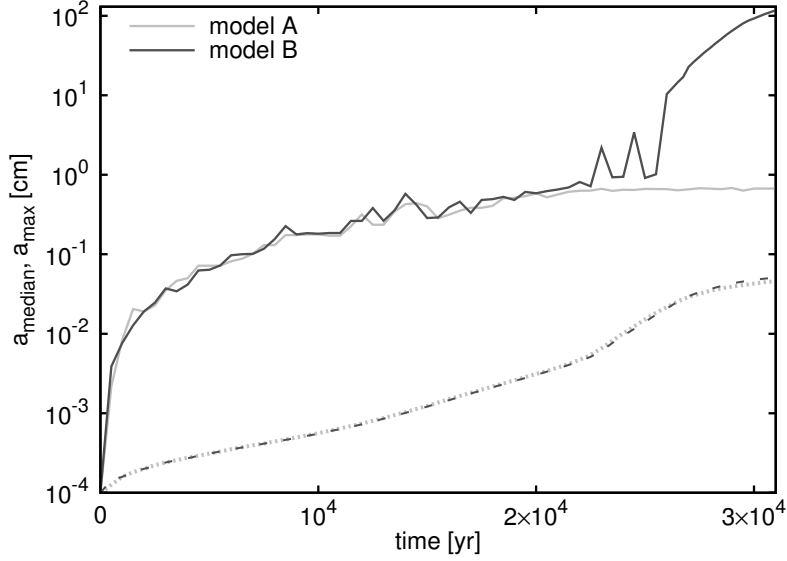


Figure 3.5: The time evolution the maximum (solid lines) and the median (dashed lines) radius of the dust particles in the model with and without the mass transfer effect. Both of the models generally evolve in similar way, what can be observed by following the median radius change. However, whereas the growth of the biggest particles is halted at sizes approximately ~ 0.7 cm by the bouncing in the case of the model A, in model B some particles manage to grow till the radius of 100 cm after 30,000 yrs.

as the growth timescale rises with the distance from the star, we would have to carry on our models over longer time and possibly start with a larger domain to see more of the seeds, which is not possible with the current state of our code, as explained below.

The model B run took about 50 days on an 8 core 2.83 GHz Intel processor. The model A run took about half as long, as all the particles stayed small so that a longer advection time step was used. Because of the computational expense of the simulations, we finish them at $t = 31,000$ yrs, when the seeds have reached sizes of 100 cm. Extrapolating the growth rate from the data, we find that the seeds would grow to km-sizes within the next 10^5 yrs. [Xie et al. \(2010\)](#) investigated the planetesimal growth by dust sweep-up and found the growth from 0.1 to 10 km within 10^6 yrs in their models. However, in our model the surface density of the dust in the pressure trap is enhanced, as the solids are constantly delivered to the trap by the radial drift, so the timescale of the growth is reduced.

The dust density distribution in the dead zone exhibits a bump for par-

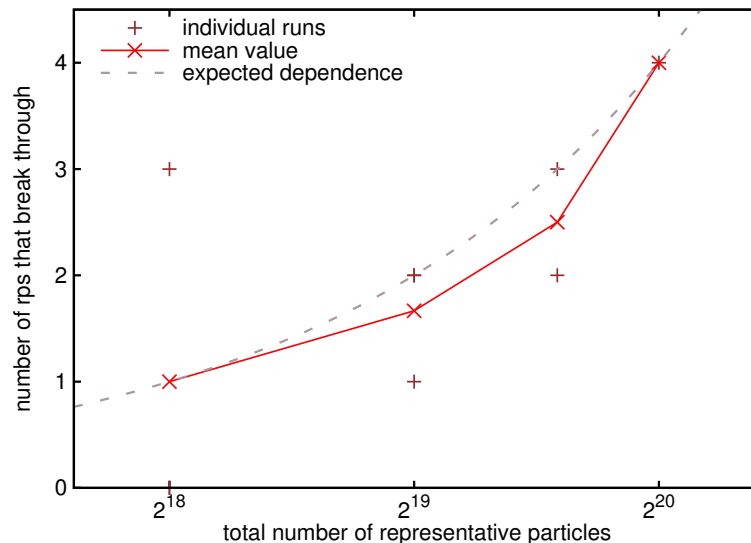


Figure 3.6: Total mass of seeds should be independent on resolution. Thus, number of representative particles that break through has to change with the total number of representative particles used. The points show results of runs with identical setup but different number of the particles, and the solid line represents the averaged value for runs with equal number of particles. The dashed line shows the expected dependence, which is consistent with our results.

ticles smaller than 10^{-2} cm (see Fig. 3.3). This feature comes from the bimodal distribution revealed in the 1-D tests presented in Sect. 2.3.4. It is not observed in the active zone while it is smeared by the relatively strong turbulence ($\alpha > 10^{-4}$). Such structure cannot be modeled by the commonly used dust evolution codes that treat the vertical structure in an averaged way (e.g. Birnstiel et al. 2010). However, the impact of resolving of this structure is hard to define without detailed comparison between results given by such 1-D code and by our code, which is much beyond the scope of this work.

3.4.1 RESOLUTION STUDY

Resolution study is important in order to confirm every new result obtained with numerical methods. We performed several runs with the same setup as described in Sect. 3.3, but varying the number of cells and the number of representative particles per cell such that the total number of particles is from two times lower to two times higher than in the runs presented in the previous section. Figs 3.6 and 3.7 present the results of this resolution study. We checked that the total mass of seeds that break through is nearly

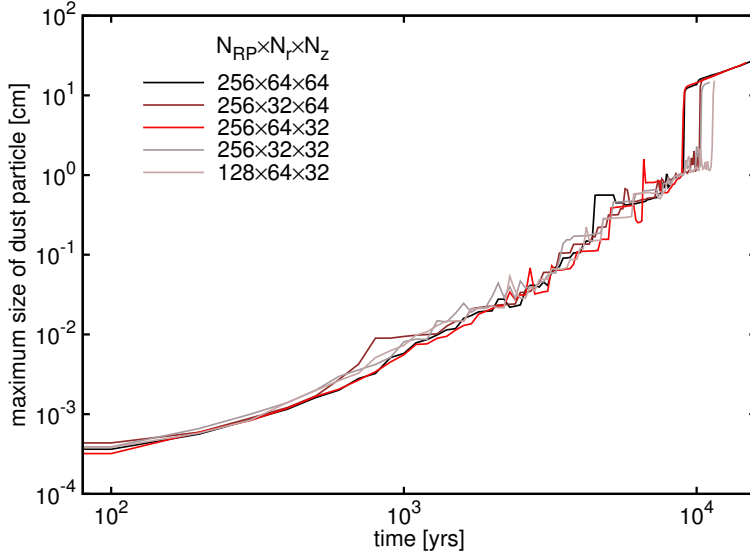


Figure 3.7: The figure shows time evolution of the maximum particle size in several runs, resolution of each is specified as number of representative particles \times number of radial cells \times number of vertical cells. The evolution is nearly identical in all the cases. We find that the time after which the first particle break through is independent on the resolution used to perform the models.

independent on resolution used. This means that we resolve the seeds well in the results presented in Sect. 3.4. We checked also that the time at which we get the breakthrough does not depend on resolution. As we will show in the Chapter 4, this is not a general rule and the time of breakthrough is dependent on numerical resolution when the breakthrough is driven by the impact velocity distribution. However, in the results presented in this chapter, the breakthrough is driven by the radial mixing of aggregates and thus such a resolution dependence is not expected.

3.5 DISCUSSION AND CONCLUSIONS

Planetesimal formation is a subject to many barriers, such as the bouncing, fragmentation and radial drift. Since it is problematic to form any grains larger than decimeter in the standard disk models, it would not be surprising if planetesimal formation could only happen in some "special" places within the protoplanetary disk. In this chapter, we investigated whether the inner edge of dead zone region can be such a place, and we found that such a sharp change in a protoplanetary disk structure can be favorable for the planetesimal formation by sweep-up as suggested by [Windmark et al. \(2012a\)](#).

3.5. DISCUSSION AND CONCLUSIONS

We applied the code presented in Chapter 2 to a snow line region in a low mass protoplanetary disk, and modeled the disk following the prescription of [Kretke & Lin \(2007\)](#), where the turbulent viscosity changes around the snow line, leading to occurrence of a low turbulence region as well as a pressure bump. We found that in such a disk it is indeed possible to grow planetesimals by the sweep-up. Due to the local dust density enhancement in the pressure bump, the sweep-up growth rate is increased, and the estimated planetesimal formation timescale is relevant for the planet formation.

Our model includes inevitable simplifications. We assumed that the disk is isothermal, i.e. the gas temperature T_g is constant along the vertical dimension. Also the turbulent viscosity D_g has been assumed to stay constant along a column at given distance from the star. We do not expect that including the dependence of T_g and D_g on the height above the midplane would influence the possibility of forming planetesimals via the mechanism described in this work. We did not include the gas disk evolution. This is not consistent with the snow line model we implement, as the gas ionization rate and thus the turbulence strength is dependent on the dust properties. As we include the dust growth, the total surface area of grains changes and thus the turbulence is modified. The disk structure builds up on the disk accretion timescale. As the dust coagulation proceeds much faster than the gas disk evolution, we start our models from a steady state disk, which is a common, but not self-consistent practice.

We focused on the disk region around the snow line, where the temperature allows for existence of solid water ice. The collisional properties of ice aggregates are generally thought to be much better than silicates. However, due to lack of laboratory data, we did not include the ice in our models. We used a collision model that reflects the evolution of silicate grains. Including collision model of ices would help the growth of particles. On the other hand, it would also require considering another complex effects, such as evaporation and condensation ([Kuroiwa & Sirono 2011](#); [Ros & Johansen 2013](#)) or sintering ([Sirono 2011](#)).

The planetesimal formation model we propose relies on the existence of a growth barrier, such as the bouncing barrier introduced by [Zsom et al. \(2010\)](#). The robustness of the barrier has recently been put into question as the sticking and bouncing efficiency have been shown to exhibit a strong dependence on the internal structure of colliding aggregates as well as the impact parameter ([Wada et al. 2011](#); [Kothe et al. 2013](#)). Even though the results on the bouncing behavior is inconclusive, we argue that fragmentation could also work in a similar fashion for the sweep-up scenario. In case where fragmentation acts as the main growth barrier, the smaller dust population would be able to grow a bit further, but might still be swept up by the

drifting seeds. As the mass transfer experiments have so far been performed over a limited parameter space only, this possibility would need to be verified experimentally.

As mentioned in Sect. 2.3.4, we did not include the effects of particle clumping via the streaming instability (Youdin & Goodman 2005) and possibility of the gravitational instability (Johansen et al. 2007) for dense midplane layer. These effects could change our results and lead to efficient planetesimal formation in the dead zone. We plan to implement these phenomena in future work.

The main conclusions of the models presented in this chapter can be summarized in the following points:

- In some protoplanetary disks, it is likely to overcome the growth barriers and obtain planetesimals via the sweep-up growth, as suggested by Windmark et al. (2012a). Since the disk properties change at different disk locations, the bouncing barrier is shifted in terms of maximum particles size. In our model the particles can grow more in the dead zone region. A limited number of these particles can become planetesimal seeds and continue to grow in the region of stronger turbulence, and their radial drift is at the same time halted because of the existence of the pressure trap.
- The snow line, as modeled by Kretke & Lin (2007), is a favorable region for the planetesimal formation by incremental growth.
- The amount of planetesimals that can be formed in the sweep-up at the inner edge of dead zone scenario presented in this chapter is very low. The total mass of planetesimals formed is of the order of 5% of the dwarf planet Ceres mass, which is $\sim 10^{-3}$ of the total dust mass included in the model.

We focused the study presented in this chapter on the snow line region, which is shown to be a favorable region for formation of big bodies in protoplanetary disk. This is consistent with other studies. The impact of the snow line is reported in the context of the exoplanets distribution. Schlaufman et al. (2009) argue that the statistical properties of observed exoplanets cannot be explained without taking the snow line into account. Also very recent work of Martin & Livio (2013) suggests that the snow line region is where the asteroid belts are preferentially formed. They come to this conclusions because of a correlation between the location of the snow line and observed warm dust belts in exosolar systems. They argue that the existence of such asteroid belts may be crucial for existence of life on rocky planets. It is worth

3.5. DISCUSSION AND CONCLUSIONS

noting that the planetesimal formation mechanism introduced in this work can take place also at locations other than the snow line. [Dzyurkevich et al. \(2013\)](#) have recently suggested that a steep variation of the turbulence efficiency and resulting pressure bump, which we need for our mechanism, can occur beyond what they call "metal freezeout line", i.e. at the border beyond which metal atoms in the gas phase thermally adsorb on dust particles. Anyway, in our model, the internal planetesimal population is formed at the same location in the disk that corresponds to the pressure maximum. Such a narrow annulus of planetesimals was suggested by [Hansen \(2009\)](#) as initial condition for formation of the terrestrial planets in the Solar System.

The thresholds that change the structure of protoplanetary disk, such as the snow line, clearly have a great significance for the emergence and evolution of planetary systems. Our models show that even with a "pessimistic" setup, in a low-mass protoplanetary disk consisting of not very sticky silicate grains, it is possible to form planetesimals at such a specific location. Further work is required to check the following evolution of the planetesimal ring. For bodies bigger than kilometers, consideration of the gravitational interactions, which we plan to include in our future work, is necessary. The question whether there will be an asteroid belt or a planet formed at the pressure trap cannot be answered at the current stage of our project.

4

PLANETESIMAL FORMATION TRIGGERED BY THE IMPACT VELOCITY DISTRIBUTION

Adapted from Drążkowska, Windmark & Dullemond, 2014, A&A, 567, A38, Windmark, Okuzumi & Drążkowska, in prep., and Drążkowska, Windmark & Okuzumi, accepted for publication in Proceedings of the IAU, Vol. 310¹

4.1 INTRODUCTION

Dust coagulation is an important astrophysical process, particularly in the case of planet formation. To form a planet, micron-sized dust particles have to collide and stick to form ever larger dust aggregates. The main problem with this picture is what is known as the "meter-size barrier": once particles reach a size of decimeter to meter, they acquire relative velocities that are too large to allow hit-and-stick growth. Instead, collisions at these speeds, which are on the order of tens of meters per second, lead to the destruction of the colliding aggregates. This is often called the "fragmentation barrier". Moreover, already at sizes of a millimeter, we encounter the "non-sticking problem", which is often called the "bouncing barrier": while the aggregates do not fragment upon collision at these sizes, they do not stick together either, meaning that the growth stalls. All these barriers are posing a major problem in our understanding of planet formation. In recent years, however, several new ideas have appeared in the literature to overcome these problems. One of the possible solution is the sweep-up growth, already discussed in the previous chapter. In this chapter, we focus on this scenario once more, but this time the "lucky" seeds are produced thanks to the impact speeds distribution contributed by turbulence.

¹See page [ix](#) for the authorship details.

4.2 MOTIVATION

The sweep-up growth scenario has been proposed as a solution for the growth barriers issue (Windmark et al. 2012a). In this scenario, a few boulders can grow large by colliding with numerous smaller pebbles through the fragmentation with mass transfer process (Wurm et al. 2005; Teiser & Wurm 2009; Meisner et al. 2013). The growth of the pebbles is suppressed due to bouncing and/or fragmentation between themselves, while a few larger aggregates, or seeds, might form if the distribution of impact velocities due to stochastic turbulence is taken into account (Windmark et al. 2012b; Garaud et al. 2013; Meru et al. 2013a). Thanks to the low velocity tail of the distribution, some grains can be "lucky" enough to not experience any destructive collisions and undergo only low-velocity sticking collisions, breaking through the growth barriers. This scenario enables the formation of planetary embryos while still keeping the disk dusty, which is consistent with observations.

Key to the trustworthiness of the conclusions derived from numerical models is the reliability of the codes and algorithms used. The problem of coagulation is extremely complex and nonlinear, and with the exception of some very simple coagulation kernels, no analytic solutions exist. So how do we know if the results of our codes are indeed correct? One way is to treat the problem with at least two distinct methods and compare the results.

Over the years, different approaches have been developed to study the dust coagulation problem. Besides numerous semi-analytic models, two main numerical approaches are used nowadays: direct numerical integration of the Smoluchowski equation and various Monte Carlo codes. The former is traditional approach, which has been used in different versions by Weidenschilling (1980); Nakagawa et al. (1981); Wetherill & Stewart (1989); Ohtsuki et al. (1990); Dullemond & Dominik (2005); Tanaka et al. (2005); Nomura & Nakagawa (2006); Brauer et al. (2008a); Okuzumi et al. (2009); Birnstiel et al. (2010); Charnoz & Taillifet (2012) and many others. This approach is often used when comparing dust coagulation models to observations, as it allows us to model the dust evolution in the global disk over very long timescales. The Monte Carlo approach is based on work by Gillespie (1975) and is used in one form by Ormel et al. (2007) and in another by Zsom & Dullemond (2008), subsequently used by Johansen et al. (2012); Ros & Johansen (2013) and Drażkowska et al. (2013). The Monte Carlo approach is useful to test different coagulation models and to include different properties of dust particles, such as the internal grain structure. It is also better suited to use along with hydrodynamic grid codes.

The two methods are usually benchmarked using analytical solutions of the coagulation equation that are available for three idealized growth ker-

nels (see, e.g., [Ohtsuki et al. 1990](#), [Wetherill 1990](#), and [Lee 2000](#)). However, these kernels do not necessarily represent any realistic growth scenario in the protoplanetary disk. In this chapter, we perform an explicit comparison between the two approaches for the first time. In this comparison, we focus on the sweep-up growth scenario, which is challenging to model for both of the methods. In particular, it was already asserted by [Windmark et al. \(2012c\)](#) that an artificial breakthrough may occur when a low mass resolution is used in the Smoluchowski method. We study this issue in more detail, and we show that not only the high resolution but also a careful treatment of interactions in low particle number density bins is needed to avoid the nonphysical growth.

Until now, the sweep-up growth triggered by the "lucky" growth was modeled using the Smoluchowski code only. Using a 2-D Monte Carlo code, in [Chapter 3](#) showed that sweep-up growth can occur at the inner edge of dead zone, but it was triggered by radial transport of big bodies grown in a dead zone in this case. In this chapter, we implement the relative velocity distribution in the Monte Carlo code and directly compare results of the two approaches, which gives us the possibility to restrict the planetesimal growth timescale and mass included in the newly formed large bodies. We also present some of the major features and differences of both the approaches.

This chapter is organized as follows: we describe both of our numerical models in [Sect. 4.3](#). In [Sect. 4.4](#), we compare results obtained with both codes. We discuss issues related to numerical convergence of both methods in [Sect. 4.5](#). We discuss the results presented in this chapter in [Sect. 4.6](#). In [Sect. 4.6.3](#), we discuss the implications of the planetesimal formation via sweep-up growth in a global protoplanetary disk. We summarize our findings in [Sect. 4.7](#).

4.3 THE NUMERICAL MODELS

We study the Smoluchowski approach using the code developed by [Brauer et al. \(2008a\)](#) and [Birnstiel et al. \(2010\)](#), along with an impact velocity distribution implemented as described in [Windmark et al. \(2012b\)](#). In this code, we let the dust-grain number density $n(m, r, z)$ be a function of the grain mass m , the distance to the star r , and the height above the midplane z , and give it in number of particles per unit volume per unit mass. The dust evolution can then be solved by integration.

However, discretization of the problem is necessary in the integration process, which can lead to a significant numerical diffusion in mass-space, because having a finite number of grid points means that particle collisions do not necessarily lead to particle masses m_p that directly correspond to

4.3. THE NUMERICAL MODELS

one of the logarithmically spaced sampling points. The approach by [Brauer et al. \(2008a\)](#) was to implement an algorithm that distributes the mass of the resulting particle into two adjacent mass bins corresponding to grid points i and $i + 1$, $m_i < m_p < m_{i+1}$, according to

$$\epsilon = \frac{m_p - m_i}{m_{i+1} - m_i}, \quad (4.1)$$

where $\epsilon \cdot m_p$ is put into mass bin m_{i+1} , and $(1 - \epsilon) \cdot m_p$ is put into mass bin m_i . This algorithm is based on the work of [Kovetz & Olund \(1969\)](#) and is adopted by most of the modern dust coagulation codes. This approach, however, leads to some numerical diffusion, as $m_{i+1} > m_p$ means that mass is inserted into a mass bin that corresponds to a larger mass than the mass of physical particle created in the collision. If the spacing between the mass bins is too coarse, this leads to a significant, artificial growth rate speed-up ([Ohtsuki et al. 1990](#)). We show that the same effect strongly affects the number of seeds formed in the "lucky growth" scenario; however, the problem is more severe and requires a careful approach to low number density regions in this case.

In the Monte Carlo method, we use the representative particles approach described by [Zsom & Dullemond \(2008\)](#) that implementation is described in Chapter 2. We have slightly modified the method to match the vertical treatment of the Smoluchowski code (described by [Brauer et al. 2008a](#)). Instead of performing an explicit vertical advection, we redistribute the particles according to a Gaussian distribution with a width:

$$H_{\text{dust}} = H_{\text{gas}} \left[1 + \frac{\min(0.5, \text{St}) (1 + \text{St}^2)}{\alpha} \right]^{-\frac{1}{2}}, \quad (4.2)$$

where H_{gas} is the pressure scale height of the gas, St is the particle's Stokes number and α is the turbulence strength parameter. In this way, we account for the reduction in the collision rate between small and large grains due to their different vertical settling. This occurs because small particles are more strongly affected by the turbulent diffusion, and, thus, their density in the midplane of the disk is lower than in the case of large particles.

One of the assumptions of the representative particle approach that we implement is that one representative particle, or swarm, represents a constant amount of mass, which is equal to

$$M_{\text{swarm}} = M_{\text{tot}} / N_{\text{swarms}}, \quad (4.3)$$

where M_{tot} is the total mass of dust present in the computational domain and N_{swarms} is the number of swarms used. In other words, the total mass

of dust M_{tot} is divided into N_{swarms} equal-mass units. Each of these units represents physical particles of mass m_i ($m_i \ll M_{\text{swarm}}$), but the number of these particles N_i has to be such that $N_i \cdot m_i = M_{\text{swarm}}$. The algorithm fails, if, for example, a physical coagulation kernel would lead to formation of only one massive particle with mass m_p , while keeping all the other particles small. If $m_p < M_{\text{swarm}}$, the single big particle cannot be resolved, because it involves less mass than the smallest available unit M_{swarm} . Increasing the number of swarms, N_{swarms} , lowers M_{swarm} and thus improves the mass resolution of the method; however, the computation time increases quadratically with the number of swarms used. The dynamic mass range of the representative particle approach is limited by the number of swarms used. This issue can be overcome by implementing a more advanced algorithm, as the "distribution method" proposed by [Ormel & Spaans \(2008\)](#) that involves continuously adjusting M_{swarm} by splitting and merging the swarms. This method was later used in the context of accretion among planetesimals ([Ormel et al. 2010](#)), allowing the Monte Carlo method to resolve a runaway coagulation kernel. However, the method was not yet tested with velocity distributions or complicated collision models that are needed to break through the growth barriers.

4.4 COMPARISON OF RESULTS OBTAINED WITH BOTH METHODS

Because our Monte Carlo method is not capable of the same dynamic mass range as the Smoluchowski method to directly compare the two methods, we choose a setup where the particle breakthrough (i.e. where the "lucky" particles can start to grow by mass transfer) occurs at relatively high particle number density, which is possible to resolve with our representative particle approach (see the previous section).

For the disk model, we use the Minimum Mass Extrasolar Nebula ([Chiang & Laughlin 2013](#)) at 1 AU. The gas surface density is $\Sigma_{\text{gas}} = 9900 \text{ g cm}^{-2}$, and the temperature is $T = 280 \text{ K}$. We assume a turbulence of $\alpha = 10^{-2}$ and a standard dust to gas ratio of 10^{-2} . We take a relative velocity between the dust grains driven by Brownian motion and turbulence into account, by calculating the root-mean-square impact velocity v_{rms} from the formulas derived by [Ormel & Cuzzi \(2007\)](#), and we assume a Maxwellian distribution of the impact velocity.

We consider sticking, fragmentation, and mass transfer as possible outcomes of collision, which we refer to as the SF+MT model ([Güttler et al. 2010](#); [Windmark et al. 2012b](#)). The collision outcome is determined by taking the sticking and fragmentation/mass transfer probabilities $P_s(v_{\text{rms}})$ and

4.4. COMPARISON OF RESULTS OBTAINED WITH BOTH METHODS

$P_{f/mt}(v_{\text{rms}})$ into account, which are calculated analogically as in [Windmark et al. \(2012b\)](#). We take the fragmentation threshold velocity to be $v_f = 50 \text{ cm s}^{-1}$. If a collision should lead to fragmentation but the mass ratio between the colliding particles mass is $m_1/m_2 > 20$ ($m_1 > m_2$), we assume projectile fragmentation with mass transfer with a 10% efficiency; that is the larger particle gains 10% of mass of the smaller one during the event. Realistic values of the collision parameters are poorly constrained, as discussed in [Sect. 4.6.2](#).

Implementing the same setup in both of the codes, we perform a number of runs by varying the numerical resolution by around one order of magnitude. In the Smoluchowski code, we use from 3 to 40 mass bins per decade. In the Monte Carlo code, we use from 12,000 to 120,000 representative particles, and we repeat each run ten times with different random seeds.

The Monte Carlo method relies on random numbers used to determine which particles are participating in the subsequent collisions and to calculate collision time steps ([Zsom & Dullemond 2008](#)). Thus, outcomes of the Monte Carlo runs performed with different random seeds vary despite using the same setup. In the velocity distribution case, this effect is even stronger, meaning that multiple runs with different random seeds are necessary. This causes our high resolution Monte Carlo models to need a few days on an 8 core 3.1 GHz AMD machine. For comparison, the Smoluchowski models with 40 bins per mass decade take about of one hour on a single core processor.

[Figure 4.1](#) shows the time evolution of the dust mass distribution obtained with both of the codes. For the Smoluchowski code, we display results obtained with the resolution of 30 bins per mass decade. For the Monte Carlo code, we display averaged results, along with their scatter, of our highest resolution simulations with 120,000 particles, which additionally showed a breakthrough before 100 yrs; otherwise, the figure gets indecipherable due to high noise.

The early evolution, as seen in the upper panels of [Fig. 4.1](#), is very similar in both codes, and the point at which the dust distribution hits the fragmentation barrier, where the growth of the majority of particles is hindered due to fragmentation that occurs when the impact velocities exceed the fragmentation threshold velocity v_f , is identical ($m \cong 10^{-2} \text{ g}$, $t \cong 20 \text{ yrs}$). If the fragmentation with mass transfer collisions are not included and there is no possibility of growth beyond the fragmentation barrier, the steady state is represented by the third panel of [Fig. 4.1](#), and the two methods agree perfectly. However, as we include the breakthrough possibility, we encounter some differences between the two approaches, which are visible at later stages of the evolution. Both of the codes reveal that some of the particles can grow beyond the fragmentation barrier thanks to the low-velocity sticking colli-

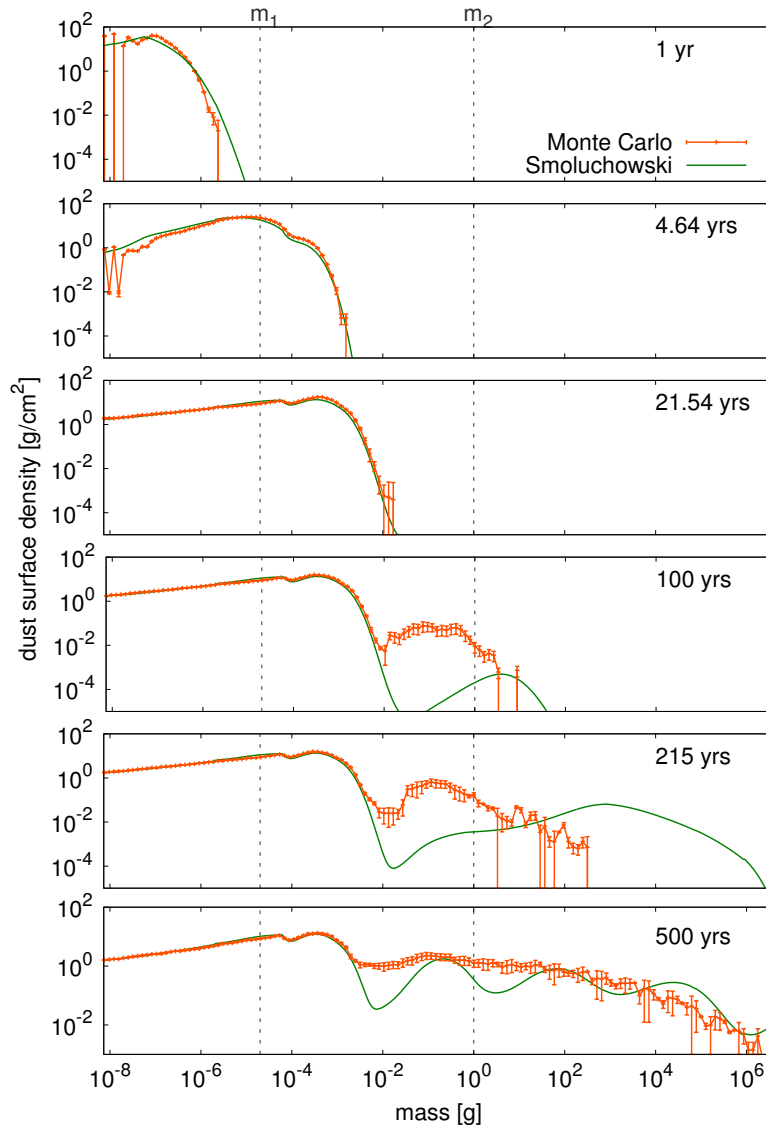


Figure 4.1: Comparison of the mass distribution evolution obtained using our Smoluchowski and Monte Carlo codes. In a standard case when an insurmountable fragmentation barrier is present, the two methods perfectly agree (three upper panels); however, we encounter some differences between the results obtained with the two approaches (three bottom panels) with the possibility of breakthrough. For the Smoluchowski code, the presented results were obtained with a resolution of 30 mass bins per decade. For the Monte Carlo code, the results are averaged from the simulations using 120,000 particles. The "check points", m_1 and m_2 , which are indicated with the dotted lines, are used to quantitatively compare dust growth timescales in Sect. 4.5.1.

sions. The growth is very quick in general and meter-sized bodies are formed within <1000 yrs. However, the breakthrough generally occurs later in the Monte Carlo code, and the population of big grains lacks the characteristic waves seen in the distribution obtained from the Smoluchowski code, which can be seen in the bottom panel of Fig. 4.1. The differences in the late stages of evolution are caused by the restricted dynamic mass range of our representative particle approach that was discussed in Sect. 4.3. We further discuss issues related to resolution dependencies of both methods in the following section.

4.5 RESOLUTION DEPENDENCE

The results obtained with both codes exhibit resolution dependence. In this section, we discuss specific issues connected to the numerical convergence of both Smoluchowski and Monte Carlo methods.

4.5.1 GROWTH TIMESCALES

To quantitatively compare dust growth obtained in both codes, we establish "check points" m_1 and m_2 , as marked with the dotted lines in Fig. 4.1. We arbitrarily choose $m_1 = 2 \cdot 10^{-5}$ g and $m_2 = 1$ g, and mark the time at which the peak of the mass distribution reaches a mass corresponding to one of the check points.

Figures 4.2 and 4.3 show the results obtained for m_1 and m_2 , respectively. We show the times of crossing the "check points" as a function of the number of bins used in the Smoluchowski code and a number of representative particles used in the Monte Carlo method. We note that the scaling of x-axes of these figures is arbitrary, as there is no method to directly connect the number of bins in the Smoluchowski method to the number of representative particles in the Monte Carlo method.

Mass m_1 is located before the fragmentation barrier. This part of the evolution corresponds to a standard growth scenario that does not include the "lucky" breakthrough possibility and is well resolved by both of the codes. In the Monte Carlo code case, the time of crossing m_1 depends very weakly on the number of particles used. The difference between individual runs, as marked by the shaded region in Fig. 4.2, is also very low. The Smoluchowski code exhibits much stronger resolution dependence. In the case of our lowest resolution of 3 bins per mass decade, the growth is more than four times faster than with 40 bins. The results obtained with resolution of 40 bins per mass decade converge to a value that is consistent with the one given by the Monte Carlo code. The critical resolution agrees with findings of Lee (2000) and Okuzumi et al. (2009).

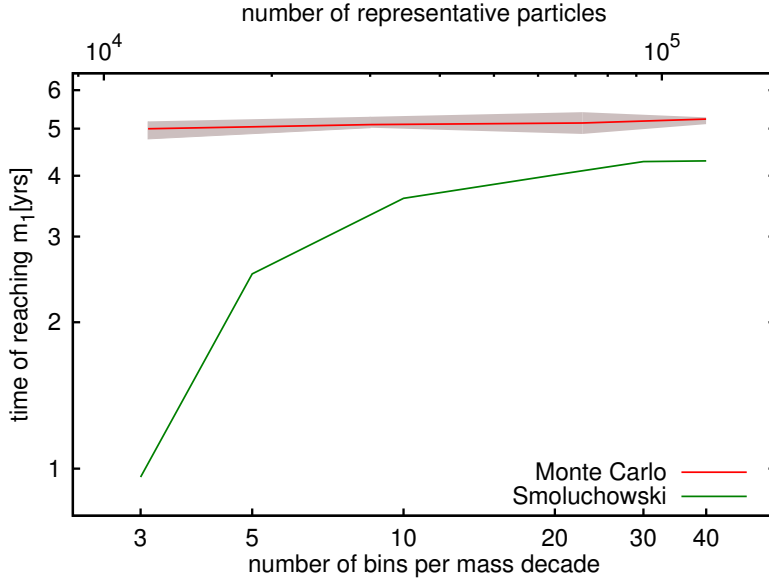


Figure 4.2: Time at which the peak of mass distribution reaches the mass $m_1 = 2 \cdot 10^{-5}$ g for both the Smoluchowski and Monte Carlo code. The result changes with mass resolution, given by the number of bins per mass decade in the case of Smoluchowski code and the number of particles used in the Monte Carlo code. The scatter of results obtained in different runs with the same number of particles in the Monte Carlo code is marked by the shaded region around an averaged dependence. The Monte Carlo approach does not exhibit a strong resolution dependence. The Smoluchowski algorithm overestimates the growth rate by a factor of few when we do not use enough mass bins.

The reason for the high diffusion of the Smoluchowski method is the linearity of the algorithm described in Eq. (4.1), which is a necessity for solvers that employ implicit integration schemes to overcome the numerical stiffness of the equations (see Brauer et al. 2008a for further details). Explicit solvers, on the other hand, are capable of implementing higher order mass distribution schemes, which lowers the numerical diffusion. We find that steady states that arise when a bouncing or fragmentation barrier is met and that have no possibility of breaking through are significantly less dependent on mass resolution. Thus, the conclusions of most of the papers that did not include breakthrough are not affected, even if a lower resolution was used.

As can be seen in the Fig. 4.3, the situation changes significantly in the case of the second check point m_2 . This point is located beyond the fragmentation barrier and breakthrough point. Due to limited dynamic mass range, the resolution dependence of the Monte Carlo code is much stronger. The dis-

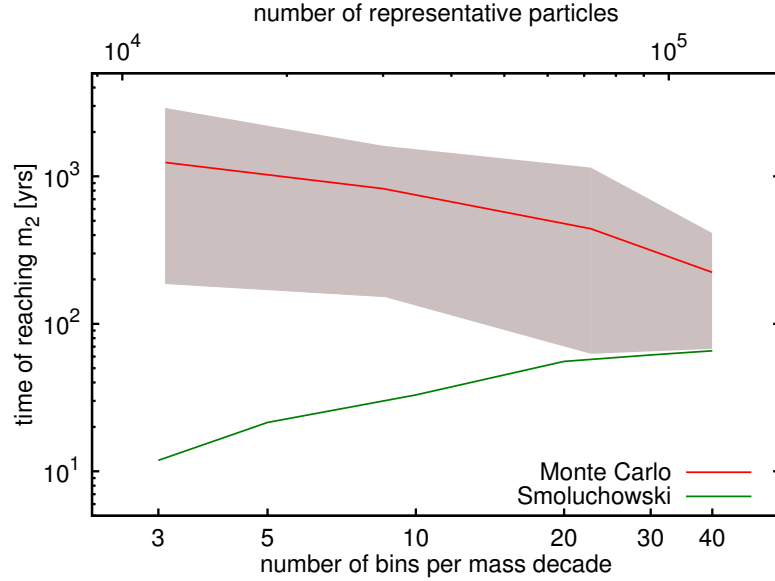


Figure 4.3: Figure analogical to Fig. 4.2 but for the "check point" $m_2 = 1$ g. The resolution dependence of the Smoluchowski method is the same as for m_1 , but it changes significantly in the case of the Monte Carlo code. The Monte Carlo code tends to underestimate the breakthrough possibility when used with a low number of particles due to the limited dynamic mass range.

persion of results obtained in individual runs is much higher and can reach even an order of magnitude. Generally, the less particles we use, the longer we have to wait for the breakthrough. In the case of the Smoluchowski code, the resolution dependence is the same as for m_1 , meaning that the lower resolution we use, the faster the breakthrough occurs. This is consistent with the findings of [Garaud et al. \(2013\)](#). The results obtained with both of the codes roughly converge for our highest accuracy. Both of the methods become computationally inefficient when used with even higher resolutions.

The different resolution dependence seen in the Fig. 4.3 is a result of a fundamental difference between the two approaches. In a real protoplanetary disk, the number of physical particles is so high that even when the breakthrough probability is low, some particles will be able to be "lucky" and overcome the fragmentation barrier quickly. However, the number of representative particles is restricted in the Monte Carlo code and the breakthrough probability is additionally reduced. In contrast, the breakthrough is resolved much easier because the Smoluchowski code deals with number densities instead of discrete particles. However, this introduces another problem, which is discussed in the following section.

4.5.2 BREAKTHROUGH PROBABILITY

The "lucky growth" scenario has introduced a new issue in how the numerical diffusion affects the global dust evolution in the Smoluchowski method. In this section, we discuss this issue and introduce a way to limit its effect by including a modulation function to the coagulation algorithm that suppresses the interactions with mass bins containing unrealistically low particle numbers.

As discussed above, when velocity distributions are introduced, the collision barriers are naturally smeared out. Because a particle that is more massive than the grains at the mass distribution peak must be "lucky" and has to grow by only interacting with other particles in low-velocity collisions, it becomes necessary to accurately resolve the high-mass tail of the distribution. Otherwise, if not all sticking events are resolved properly, the slope of the tail becomes incorrect, creating artificially large mass ratios between the luckiest grains and those in the peak.

As an example of this, we can consider the extreme case where the entire high-mass tail is represented by a single mass bin m_i . If two grains in the peak undergo a single sticking event, forming a particle of mass $m \ll m_{i+1}$, some mass will still be put into the mass bin $i + 1$, even though the particles would need to undergo several consecutive sticking events to reach a mass m_{i+1} in reality. Such a badly resolved large-particle tail could cause an artificial breakthrough of growth barriers, as unrealistically large particles can form that continue to grow by the sweep-up process where no such particles would form in a better resolved case.

To show this issue clearly, we perform additional simulations with the Smoluchowski code using a critical mass transfer ratio, that is the mass ratio above which a fragmenting collision leads to mass transfer (see Sect. 4.4), of 500. The point of breakthrough then occurs at a very low dust density, which is impossible to resolve with our implementation of the Monte Carlo method, as the particles that should break through would involve less mass than the mass of single swarm in our simulation (see also Sect. 4.3). We have therefore performed a resolution study with the Smoluchowski code only. Simulations were run with resolutions between 3 and 40 bins per decade of mass with the results shown in Fig. 4.4. As can be seen, the SF+MT case is extremely sensitive to the mass resolution. Between the highest and the lowest resolutions, the point of breakthrough differs by more than 25 orders of magnitude in surface density. For resolutions above 30 bins per decade, the point of breakthrough would have occurred at a density lower than the density corresponding to 1 particle in an annulus of 0.1 AU width.

To correctly simulate the lowest dust densities, it becomes necessary to

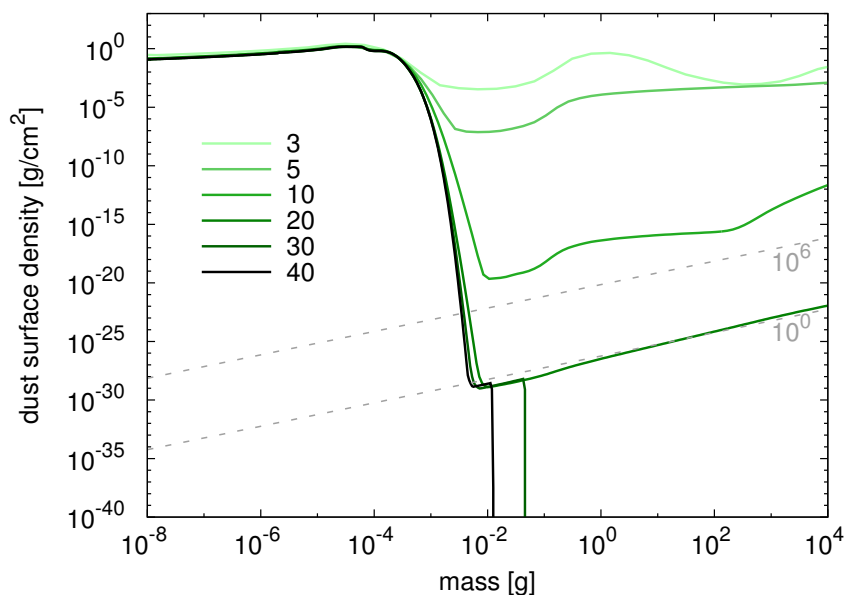


Figure 4.4: The effect of mass resolution in the case of SF+MT setup with a critical mass ratio of 500 for the Smoluchowski code. The resolutions included a range from 3 to 40, and the mass distribution is shown after 100 yrs of evolution. The point of breakthrough is very sensitive to the resolution used, and the breakthrough happens only in the low resolution cases, which is clearly nonphysical. The dashed lines mark the density corresponding to 1 and 10^6 particles of a given mass in an annulus of 0.1 AU width.

include a modulation function, f_{mod} , that limits the interactions between mass bins that have particle numbers that are too low. The reasoning behind this is the following. For breakthrough to occur, we need at least 1 real particle within the simulation domain that is large enough to trigger a sweep-up. Because the Smoluchowski code deals with number densities in a single point in space, the limiting particle density becomes somewhat arbitrary and relies on choosing a reasonable physical domain size.

The modulation function works in a similar way to the active bin method introduced by Lee (2000). Instead of speeding up the code by deactivating low-populated mass bins; however, it is a continuous method that prevents growth of bins with unrealistically low particle numbers. The collision frequency between particle species i and j can then be written as

$$f_{ij} = n_i n_j K_{ij} \cdot f_{\text{mod}}, \quad (4.4)$$

where n_i and n_j are the number densities, K_{ij} the coagulation kernel. We

choose $f_{\text{mod}} = \exp(-1/N_i - 1/N_j)$, where N_i and N_j are numbers of particles in a given surface of the disk, which we take to be an 0.1 AU wide annulus at 1 AU. The result of this is that mass is allowed to be put into a mass bin with a non-unity amount of particles by coagulation, for example, but the mass inside is unable to coagulate further until the bin contains sufficient mass.

For our setup, the modulation function f_{mod} suppresses the breakthrough in the case of resolution larger than 30 bins per mass decade. The breakthrough that occurs in the runs with lower resolution is a result of the numerical diffusion introduced by the mass distribution algorithm (Eq. 4.1), which is discussed in the Sect. 4.3. This is seen by the sharp cut-off at masses between $10^{-2} - 10^{-1}$ g for the highest resolutions. We stress that this particular resolution dependency varies very strongly between setups, and it is necessary to confirm numerical convergence individually.

We want to note that even a high resolution run can lead to a nonphysical breakthrough if f_{mod} is not included. In such a case, breakthrough would initially occur at densities corresponding to less than one particle in an annulus of 0.1 AU width, but the density of the high-mass tail could increase over the threshold density during further evolution. Thus, the combination of sufficient numerical resolution and the modulation function is necessary to ultimately confirm the possibility of forming planetesimals in the breakthrough scenario under given conditions.

In this section, we clarified the issue of too crude mass resolutions found by Windmark et al. (2012c). Although the lower resolutions commonly used in previous papers might work well for less extreme cases, which did not include the possibility of breakthrough, an artificial growth might occur for problems of the kind discussed here. Thus, we stress that careful convergence tests are necessary to confirm breakthrough possibility. We find that the convergence depends strongly on the strength of the growth barrier, and therefore, a separate convergence study is needed for each setup.

As was shown in the previous section, the Monte Carlo code underestimates the breakthrough chance with low particle numbers in contrast to the Smoluchowski code, and, thus, the time at which breakthrough happens increases. If the Monte Carlo code is used with not sufficient number of particles, the breakthrough might be completely suppressed. This happens when the mass that should be involved in the breakthrough is lower than M_{swarm} , the mass represented by a single swarm, that limits the dynamic range of the Monte Carlo method (see Sect. 4.3). The minimum number of representative particles required is dependent on the breakthrough mechanism. Here, the breakthrough is driven by distribution in the impact velocities, which smear out the fragmentation barrier by changing the slope of the mass distribution

high-mass end. The breakthrough is only possible if the largest particles are more massive than the particles in the mass distribution peak by a factor defined by the critical mass ratio. Thus, the number of breakthrough particles is defined by the mass distribution function slope and the value of the critical mass transfer ratio. The higher the slope and the critical mass ratio, the lower number of particles can break through. However, it was shown in Chapter 3 that the breakthrough can also be driven by radial mixing of dust aggregates between regions of different grain sizes. In such case, the number of breakthrough particles follows different constraints than here.

4.6 DISCUSSION

4.6.1 COAGULATION CODES

The issue of numerical resolution of the Smoluchowski code has been discussed for a long time in the context of dust coagulation in protoplanetary disks (Ohtsuki et al. 1990; Wetherill 1990; Lee 2000). These codes used different algorithms that do not necessarily result in similar resolution dependencies as the implicit integration scheme with the linear mass distribution algorithm we use.

In this chapter, we extended the prior studies by implementing a possibility of breaking through growth barriers with impact velocity distributions and including a direct comparison to the Monte Carlo algorithm with representative particle approach. The two methods have never before been explicitly compared. Our work showed that the two methods give consistent results when applied to usual coagulation problems. However, we find that modeling of the recently discovered planetesimal formation via "lucky growth" is much more challenging. Although the results obtained with the two methods converge for sufficient resolution, the approaches are fundamentally different and their limitations have to be realized when performing scientific models.

In agreement with previous studies, we find that simulations with the Smoluchowski code require a sufficiently high mass resolution to avoid an artificial speed-up of the growth rate. This problem arises from numerical diffusion and our implementation of the algorithm, which is required to describe how the resulting mass is distributed after a collision event. Additionally, we show that the introduction of the modulation function that prevents interactions between mass bins containing less than one physical particle is necessary to study the dust coagulation at low number densities. In the Sect. 4.5.2, we have shown that the numerical issues can change both the quantitative and the qualitative result in the case of the breakthrough scenario.

The Monte Carlo approach used to study the breakthrough scenario, in which only a few "lucky" particles break through the growth barriers, results in a high noise. In the presented tests, the individual runs show times of breakthrough that are orders of magnitude different and their averaged value depends on mass resolution. However, contrary to the Smoluchowski approach, the Monte Carlo approach does not suffer a strong resolution dependence when the dust aggregates grow with a relatively narrow size distribution, which usually is the case for small aggregate evolution when no breakthrough or runaway growth are possible. The Monte Carlo methods are generally computationally expensive, and they require numerous runs with different random seeds to reduce the noise.

The convergence of each of the methods can be very different for every setup. We cannot present a general recipe for the minimum resolution required to study dust growth, because this can vary enormously from case to case. Thus, it is important to run resolution tests for every new physical model until convergence of results is obtained.

We find the breakthrough scenario to be more sensitive to resolution issues than other problems we have tested, when the dust growth is utterly stopped by bouncing or fragmentation. At the same time, this scenario is of particular importance for the current planetesimal formation theory. Regardless of the method used, modeling of the "lucky growth" requires extreme computational force, and restricting the resolution to make the models more efficient can lead to serious numerical artifacts: the nonphysical breakthrough in the Smoluchowski approach case and lack of breakthrough in the case of the Monte Carlo approach.

To conclude the technical part, we list features that characterize the two main coagulation methods. One should keep these in mind when deciding which method to use for a particular scientific application.

The Smoluchowski equation solver with implicit integration scheme

- is capable of simulating dust evolution over long timescales (even at high resolutions, 0D simulations are finished within minutes),
- resolves equilibrium states well, as the implicit integration scheme allows for very large time-steps once the solution approaches steady-state ([Birnstiel et al. 2010](#)),
- has a very high dynamical range that allows phenomena involving a single physical particle of tiny mass (compared to the total dust mass) to be resolved, which makes it ideal for breakthrough studies ([Windmark et al. 2012a](#)), and to produce synthetic observations, as the opacity is

dominated by small particles, which may contain only a low fraction of the dust mass,

- is slowed by a factor of $\mathcal{O}(n^3)$, where n is the number of mass bins, for each additional dust property beyond mass (Windmark et al. 2012a), although numerical tricks exist to circumvent this (see, e.g., Okuzumi et al. 2009),
- suffers from high numerical diffusion that affects both growth timescale and breakthrough likelihood. The growth timescale can be benchmarked against the analytical kernels (e.g. Ohtsuki et al. 1990), but it depends strongly on the strength of the barrier in the breakthrough case.

The Monte Carlo coagulation algorithm with equal-mass representative particles

- makes it easy to implement additional particle properties, such as porosity (Zsom & Dullemond 2008; Zsom et al. 2010), because the computation time does not depend significantly on the number of properties that are evolved, but only on the number of collisions performed,
- it is straightforward to develop it to further spatial dimensions (Zsom et al. 2011a; Drążkowska et al. 2013), as the representative particles can be treated as Lagrangian tracer bodies,
- can be used along with hydrodynamic grid codes (Johansen et al. 2012),
- experiences no numerical diffusion of the mass function in general, so there is no danger of encountering an artificial speed-up of the growth,
- has difficulty resolving features that include low fraction of total mass, which makes it less useful in the case of breaking through the growth barriers or runaway growth modeling, although the algorithm can be developed to overcome this issue (Ormel & Spaans 2008),
- makes it hard to model evolution over long timescales in general, because it is impossible to use extremely long time-steps, as every collision needs to be resolved.

4.6.2 PLANETESIMAL FORMATION EFFICIENCY

Since we find that the numerical convergence is sensitive to the collision model parameters, it is important to use realistic values. However, these are poorly constrained, as the amount of data we have from laboratory experiments is restricted, and it is still not necessarily reproduced by direct numerical simulations. Laboratory experiments show that bouncing collisions start to occur at velocities between 0.1 and 10 cm s⁻¹ (Kothe et al. 2013), while numerical simulations claim that such collisions only rarely occur, if ever (Wada et al. 2011; Seizinger & Kley 2013). Fragmentation is also hotly discussed, as laboratory experiments find fragmentation to occur at velocities as low as a few cm s⁻¹ between 5 cm grains (Schräpler et al. 2012) and up to a few m s⁻¹ for mm-sized grains (Lammel 2008). Numerical simulations, on the other hand, predict significantly higher threshold velocities for fragmentation, ranging between 1 and 12 m s⁻¹ for 6 to 10 cm-sized grains (Wada et al. 2011; Meru et al. 2013b). The value of the fragmentation threshold velocity determines the maximum size of particles that we are able to obtain before the breakthrough happens. Mass transfer experiments are even more uncertain with the mass transfer efficiency that ranges between 0 and 60% (Teiser & Wurm 2009; Kothe et al. 2010; Beitz et al. 2011; Meisner et al. 2013), and the critical mass ratio, which is in principle unexplored in the laboratory and only for small ratios numerically (Meru et al. 2013b; Wada et al. 2013). In all of these cases, additional material and collisional properties, such as porosity, composition, structure and impact angle also greatly influence the outcome, which adds to the uncertainty. As discussed in this work, the critical mass transfer ratio might need to be significantly lower than estimated in prior studies, due to the need for a relatively high numerical resolution of Smoluchowski solvers to accurately represent the high-mass tail.

The collision models used in sweep-up modeling attempt to simplify the very complex physics of collisions between dust agglomerates. There have been a few attempts at more rigorous models (Zsom et al. 2010; Windmark et al. 2012a) to consolidate the recent progress in laboratory and numerical collision experiments (Wada et al. 2007; Blum & Wurm 2008; Güttler et al. 2010), but these are still not necessarily more correct than the simple models that narrow the modeling down to only a few key parameters (Windmark et al. 2012b; Garaud et al. 2013; Meru et al. 2013a; Drażkowska et al. 2013). As the critical mass ratio plays the crucial role in determining if the breakthrough is possible, restricting its realistic values should be a priority for the future laboratory studies.

The amount of planetesimals formed in our local models would depend

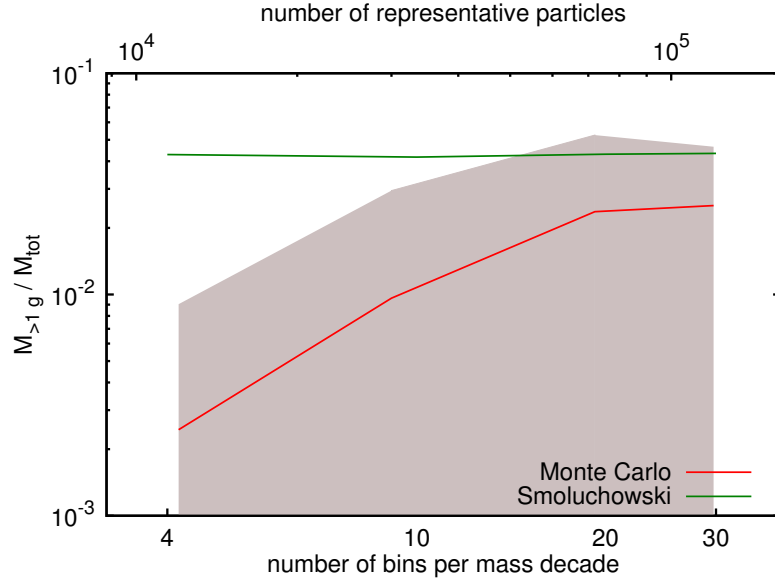


Figure 4.5: Mass fraction of large aggregates (with mass above $m_2 = 1$ g) found in the results of tests presented in Sect. 4.4. The shaded region shows the scatter of results in the case of the Monte Carlo approach. The fraction of large grains, which corresponds with the possibility of planetesimal formation, depends on the numerical method and resolution used. The results converge to $M_{>1\text{ g}}/M_{\text{tot}} \approx 4\%$

on the method and resolution used. In Fig. 4.5, we analyze the results of our tests in order to extract the mass of aggregates larger than $m_2 = 1$ g at the end of each run, and plot the value normalized by the total mass of dust used. We find that at low resolutions, the Monte Carlo code does not resolve the possibility of planetesimal formation well, which is connected to the issue of low dynamic mass range discussed earlier in this chapter. In contrast, the Smoluchowski approach gives a roughly constant value. The results converge at $\sim 4\%$ of large grains. A minimum size of a planetesimal is roughly 100 m, when the self-gravity starts to dominate over the material strength (Benz & Asphaug 1999). This corresponds to mass of $\sim 10^{12}$ g, which is much higher than we model. Due to computational reasons, we are not able to extend our models to masses corresponding to planetesimals. However, we already see that the formation of any large bodies is not very efficient and that at most a few percent of the dust aggregates will be turned to planetesimals in the sweep-up growth scenario.

4.6.3 SWEEP-UP GROWTH IN A GLOBAL DISK

The sweep-up growth triggered by the relative velocity distribution allows us to form planetesimals essentially anywhere in the disk. Presence of the turbulence contributing the stochastic impact speeds is the only requirement. This way, we overcome the growth barriers caused by the collisional physics of aggregates (see Sect. 1.3.3). However, we are still left with the radial drift barrier, which results from the timescale of radial drift being shorter than the growth timescale. Because of this barrier, the growing bodies drift inwards and cannot be kept in the outer part of the protoplanetary disk. However, the radial drift barrier is not immeasurable.

Discussing the growth barriers in Sect. 1.3.3, we have shown maps of the growth barriers in the case of an equal-sized growth in three different disks models (Fig. 1.9). In each of the cases, there is a region free from the drift barrier in the inner part of the disk. Is it then possible to keep the planetesimals formed via the sweep-up growth in the disk? In Sect. 1.3.3, we performed a simple toy model that followed evolution of a few test particles, including the interplay between their growth and drift (Eq. 1.36). Similar toy model can be constructed for the sweep-up growth case. In this case, the growth rate changes to

$$\frac{da}{dt} = \epsilon_{\text{mt}} \rho_{\text{d}} \Delta v / \rho_{\text{p}}, \quad (4.5)$$

where ρ_{d} is the density of small particles that are "swept" by the large aggregate, Δv is the impact speed, ρ_{p} is the internal density of grains, and ϵ_{mt} is the efficiency of the mass transfer, describing how much mass of the small aggregate is transferred to the large one during one collision. The growth rate is similar to the one for equal-sized growth (Eq. 1.37), however it is restricted by the efficiency parameter ϵ_{mt} and by the fact that the small grains do not settle to the midplane as efficiently as the large ones, meaning that their density ρ_{d} is typically lower than in the equal-sized growth case. On the other hand the sweep-up growth rate is not limited by the fragmentation threshold and this is what is the most important here.

Figure 4.6 shows a map of the growth barriers in a Minimum-Mass Extrasolar Nebula disk model, introduced earlier in this chapter, in terms of the distance from the star and dust grain size. Panel a) corresponds to the equal-sized growth and panel b) shows the map for the sweep-up growth mode. The grey region corresponds to the radial drift barrier, and the yellow region to the fragmentation barrier. The drift barrier is more pronounced in the sweep-up growth case than in the equal-sized growth case because the sweep-up growth rate is lower. However, the region that is free of the drift barrier still exists inside 1 AU and this is where our growing test particles pile-up, indicating that planetesimals should be able to both form and remain

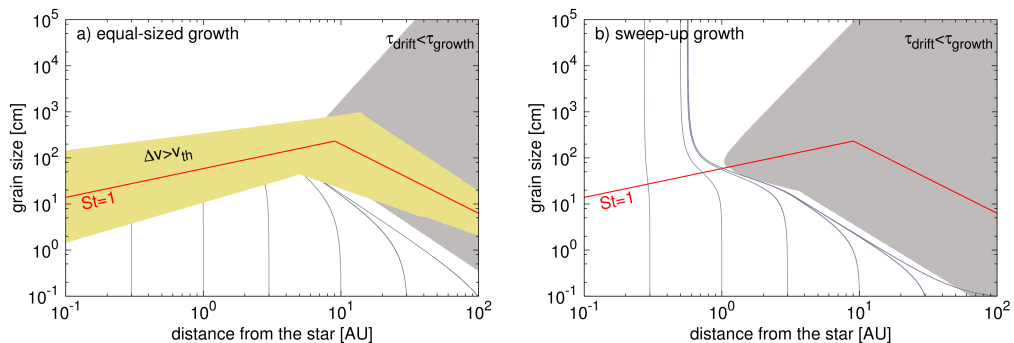


Figure 4.6: Maps of the growth barriers: the radial drift barrier (grey region) and the fragmentation barrier (yellow region), and evolution of test particles (grey lines): a) for the usual, equal-sized growth mode, b) for the sweep-up growth. The red line corresponds to aggregates with Stokes number of unity, which have the highest radial drift and impact velocities. The fragmentation barrier corresponds to impact velocities higher than $v_{\text{th}} = 10 \text{ m s}^{-1}$.

there. The possibility of rapid coagulation in the inner part of the disk was previously discussed by [Birnstiel et al. \(2010\)](#) and [Okuzumi et al. \(2012\)](#).

We check the predictions of the toy model, which comprises only a simplified prescription for drift and growth of test particles, by direct numerical simulations using a 1-D version of the Smoluchowski equation solving dust coagulation code described earlier in this chapter with the same Maxwellian velocity distribution implemented. The mass transfer efficiency is set to $\epsilon_{\text{mt}} = 50\%$. Results obtained with this model are presented in Fig. 4.7. A population of km-sized planetesimals is formed very quickly inside of 1 AU, but a large population of small aggregates is also present due to the original fragmentation barrier, shown with the orange dashed line. Redistribution of the solid material by the radial drift leads simultaneously to significant pile-up in the inner disk, reaching a few times the initial dust-to-gas ratio, and to depletion of solids beyond 1 AU. The results presented in this contribution will be described in more detail in Windmark et al. (in prep).

While it has been previously postulated that the radial drift may lead to a pile-up of the solid material in the inner disk ([Youdin & Shu 2002](#); [Laibe et al. 2012](#); [Hansen 2014](#)), the interplay between dust drift and growth was investigated only briefly. We show that including both growth and drift leads to the conclusion that planetesimals can only form and survive in the inner part of the disk, where the growth rate exceeds the drift rate. This

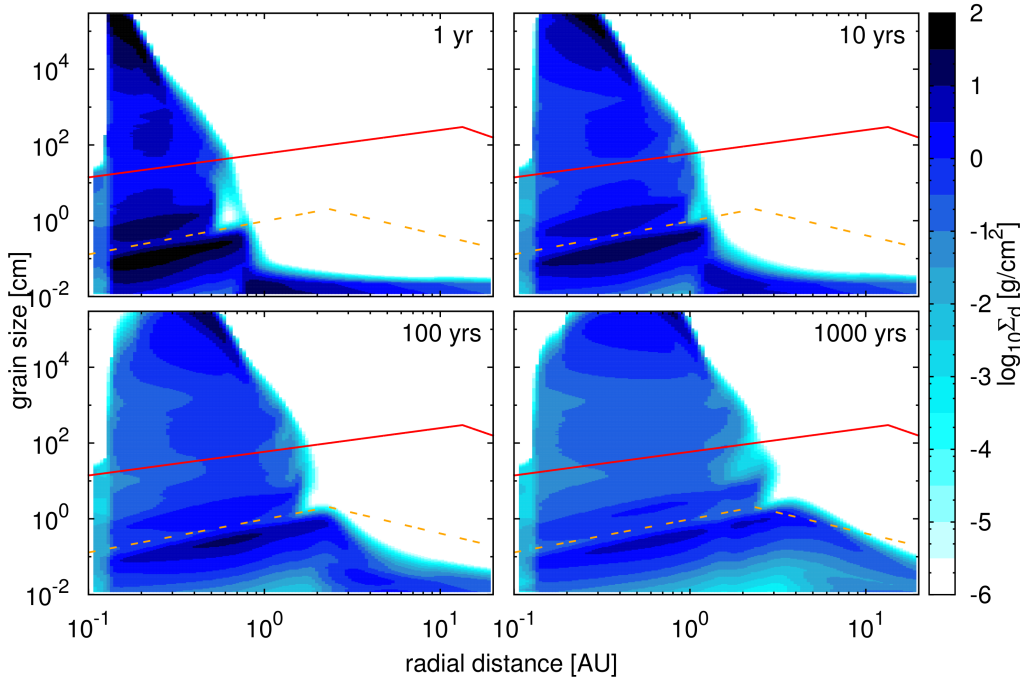


Figure 4.7: Results of the dust coagulation simulation with the sweep-up growth and impact velocity distribution enabled. The panels show color-coded surface density of dust aggregates. Planetesimals are formed very efficiently inside of 1 AU. The original fragmentation barrier, marked with the orange dashed line, is still impacting the outcome: only some fraction of dust aggregates is able to overcome it. The solid red line corresponds to the Stokes number of unity.

scenario, which we call *sweep-up and pile-up*, is particularly interesting in the context of two issues: low mass of Mars and systems with tightly-packed inner planets.

Raymond et al. (2009) showed that attempting to reproduce the final assembly of the inner Solar System starting from an initially uniform distribution of planetesimals leads to mass for Mars significantly higher than observed. Hansen (2009) found that the mass of Mars can be reproduced if all the planetesimals are initially packed in a narrow annulus between 0.7 AU and 1 AU. Standard explanation of this setup involves the Grand Tack scenario, where Jupiter migrates inwards and reaches the semi-major axis of only 1.5 AU, before reversing the migration direction due to the interaction with

Saturn. The gravitational interactions with Jupiter truncate the planetesimal disk at roughly 1 AU. Subsequent planetesimal accretion gives a mass for Mars consistent with observations (Walsh et al. 2011). Most recently, Izidoro et al. (2014) showed that the low mass of Mars can be reproduced using a disk with an initial ad-hoc depletion of solids between 1 AU and 2 AU. Our scenario may naturally produce planetesimal distribution required to reproduce the masses of inner Solar System planets and we are going to investigate this in our future work.

The *Kepler* mission has found hundreds of new exoplanets. Many of them are in multiple systems, with 3 to 5 planets with orbital periods of less than 100 days and very low inclinations (Fang & Margot 2012). These multi-transiting systems with tightly-packed inner planets could form by migration of planets from the outer disk (Raymond & Cossou 2014), but this would lead to mean-motion resonances, which are only observed in some of the systems. The planetesimal formation scenario we present suggests that in situ formation of these systems is a natural outcome of solid material evolution in a gas-rich protoplanetary disks.

4.7 CONCLUSIONS

The sweep-up growth was announced as an efficient way of overcoming the bouncing and fragmentation barriers and growing planetesimals in high impact speed collisions (Windmark et al. 2012a). Chapter 3 showed that this scenario can be triggered in some privileged places such as the inner edge of dead zone, where a few large aggregates can be mixed in the "sea" of small particles, but the efficiency of planetesimal formation in such scenario is low. In this chapter, we investigated scenario in which the sweep-up growth is triggered by the impact speed distribution (Windmark et al. 2012b; Garaud et al. 2013; Meru et al. 2013a). This scenario, in principle, does not require any special conditions, only the turbulence is needed.

By comparison of the Smoluchowski solver with the Monte Carlo method, we showed that the previous results, suggesting that, with the impact speeds distribution, planetesimal formation can be triggered easily, might have been affected by numerical issues, namely the low resolution and lack of the algorithm limiting low particle number interactions (Sect. 4.5.2). The sweep-up growth scenario may still work, but it is impossible to confirm it without more detailed laboratory data, which would allow us to constrain the values of two critical parameters: the critical mass ratio and the mass transfer efficiency. The amount of planetesimals formed in this scenario is dependent on the assumed parameters. In our local models, despite assuming pretty optimistic parameter values, it was on the order of a few percent of the total

dust mass.

It is important to remember that the possibility sweep-up growth solves only the problem of lack of growth in the high impact speeds collisions. The radial drift barrier still prevents formation of any large grains, particularly in the outer part of the disk. In Sect. 4.6.3, we presented the sweep-up and pile-up scenario for planetesimal formation in the inner part of the protoplanetary disk. We explained this scenario using a simple toy model and confirmed it with direct numerical simulations. Including both the radial drift and dust growth is crucial for this scenario, as it emerges from the interplay between the two processes. Because of the radial drift barrier, the planetesimals can only form and survive in the inner part of the disk, which could explain the low mass of Mars and suggests an in situ formation of the exoplanetary systems with tightly-packed inner planets discovered by the *Kepler* mission.

4.7. CONCLUSIONS

PLANETESIMAL FORMATION VIA THE STREAMING INSTABILITY

Adapted from Drazkowska & Dullemond, accepted for publication in A&A¹

5.1 INTRODUCTION

The number of known exoplanets is steadily rising, and it already exceeds 1800. Indirect methods indicate that every star in our Galaxy has at least one planet on average (Cassan et al. 2012). Planet formation is ubiquitous and result in a variety of planetary systems architectures. However, the details remain a mystery, as they are impossible to follow with direct observations: these only cover the very first stages of planet formation, when protoplanetary disks consist mainly of gas and small dust particles, and its outcome in the form of the exoplanet population.

Planets form in disks surrounding young stars. The solid material has initially form of μm -sized grains, which are already present in the interstellar medium (Pagani et al. 2010). Analytical and numerical models of dust evolution aim to explain the growth of the primordial μm -sized grains through around 40 orders of magnitude in mass to >1000 km-sized planets. However, the growth encounters serious obstacles already at the beginning of the size range, and these are referred to as growth barriers. There are in principle two kinds of the growth barriers: resulting from collisional physics of dust aggregates and resulting from radial drift timescale. Barriers of the former type are known as the bouncing and fragmentation barrier. They arise from the impact speeds being too high to allow aggregate sticking. An overview of collisional physics of dust aggregates is given by Güttler et al. (2010). Implementing a complex model derived from the laboratory work into a dust coagulation code, Zsom et al. (2010) found that the silicate grains growth is inhibited by aggregates compaction and bouncing already at millimeter sizes. Icy particles, which can exist outside the snow line, are considered to be more sticky and presumably avoid the bouncing behaviour (Wada et al.

¹See page ix for the authorship details.

2011). However, even without bouncing, the impact velocities reaching a few tens m s^{-1} are too high to allow grain growth and rather lead to fragmentation (Blum & Münch 1993; Blum & Wurm 2008; Meru et al. 2013b). At even smaller sizes, for $<$ mm-sized aggregates, there was another sticking barrier found, called the charge barrier, which is resulting from the electrostatic charge of small aggregates (Okuzumi 2009).

The second kind of barrier is known as the drift barrier and it is caused by the sub-Keplerian rotation of pressure supported gas disk. The dust grains interact with the gas via aerodynamic drag, lose their angular momentum and drift toward the central star. For roughly decimeter-sized grains, the drift timescale is typically shorter than the growth timescale. Thus, such grains are removed from a given location in the disk faster than they can produce any larger aggregates (Weidenschilling 1977a; Nakagawa et al. 1986; Brauer et al. 2007, 2008a).

There are several concepts that facilitate overcoming the growth barriers and producing bodies which are held together by self-gravity: planetesimals with minimum size of 100 m (Benz & Asphaug 1999). Such concepts are, among others, pressure bumps (Whipple 1972; Kretke & Lin 2007; Brauer et al. 2008b; Pinilla et al. 2012b; Drażkowska et al. 2013), dust accumulation in vortices (Barge & Sommeria 1995; Bracco et al. 1999; Klahr & Bodenheimer 2006; Lyra et al. 2009; Meheut et al. 2010), sweep-up growth (Windmark et al. 2012a,b; Garaud et al. 2013; Meru et al. 2013a; Drażkowska et al. 2014), ice condensation (Cuzzi & Zahnle 2004; Ros & Johansen 2013), and ultra-porous grain growth (Okuzumi et al. 2012; Kataoka et al. 2013a). A review of the current understanding of planetesimal formation can be found in Johansen et al. (2014). In this chapter, we focus on planetesimal formation by gravitational collapse of dense dust clumps produced by two-fluid instability known as the streaming instability.

One of the early scenarios of planetesimal formation was proposed by Goldreich & Ward (1973). This model relied on dust settling towards the midplane of the protoplanetary disk and formation of thin, unstable disk of solids. Such a thin disk would then fragment because of the gravitational instability and the fragments would collapse directly to planetesimals. However, it was found that formation of such a thin midplane layer is not possible, because as soon as the local dust-to-gas ratio in the midplane exceeds unity, the shear instabilities (Weidenschilling 1980; Cuzzi et al. 1993; Weidenschilling 1995), in particular the Kelvin-Helmholtz instability (Johansen et al. 2006; Barranco 2009) occur.

Formation of planetesimals by gravitational instability is still possible if a strong clumping of dust is present. The complicated interactions between gas and dust may lead to development of a powerful instability, called

streaming instability, that cause strong inhomogeneities in the dust density (Goodman & Pindor 2000; Youdin & Goodman 2005). The instability is most efficient for high dust-to-gas ratios and large particles, with stopping times corresponding to the orbital timescale. Youdin & Johansen (2007) and Johansen et al. (2007) confirmed that this instability is able to produce very dense dust clumps and lead to rapid planetesimal formation. This result was later confirmed by high resolution numerical simulations (Johansen et al. 2011), as well as by other authors using different methods and codes (Balsara et al. 2009; Tilley et al. 2010; Bai & Stone 2010a; Jacquet et al. 2011; Kowalik et al. 2013).

5.2 MOTIVATION

The numerical models of the streaming instability are generally computationally expensive and do not allow us to perform wide parameter studies or use extended simulation domains. They are also typically initialized with an arbitrary particle size distribution, often with even just a single particle species. The aggregate sizes used in the simulations are usually relatively large, corresponding to Stokes numbers of $10^{-2} - 1$, whereas in a primordial protoplanetary nebula we expect μm -sized grains, which correspond to Stokes number of 10^{-6} . Larger grains may be produced by coagulation, but their maximum size is limited by the bouncing and fragmentation at Stokes numbers in range $10^{-4} - 10^{-1}$. Choosing only a narrow size distribution and assuming that all of the dust particles are large leads to a kind of super-critical initial condition and the instability is triggered very quickly. We expect that gradual dust growth leads to a quite wide and highly problem-dependent size distribution, meaning that only some fraction of the largest grains will be able to participate in clumping (Bai & Stone 2010a). These particles can already form planetesimals, while other particles are still growing and gradually refill the population of big grains.

Besides the abundant large grains, streaming instability also requires that the vertically integrated dust-to-gas ratio is super-solar and the local dust-to-gas ratio is higher than unity, which makes it only possible to happen in a dense midplane layer. Such a midplane layer can be relatively easily formed in a dead zone, where no turbulent diffusion is present. In order to investigate the interplay of dust coagulation and the planetesimal formation in the streaming instability triggered in a dead zone of protoplanetary disks, we build a semi-analytical model of the latter effect into our dust coagulation code based on the Monte Carlo algorithm and representative particle approach (Zsom & Dullemond 2008). We base our model of the streaming instability on the work of Bai & Stone (2010a,c). We describe the numerical

model in the Sect. 5.3. Basing on this approach, we present simple estimates in Sect. 5.4 and results of full numerical models in Sect. 5.5. We offer an analytical formula that explains these results in Sect. 5.5.3. We discuss limitations of our approach in Sect. 5.6 and summarize our work in Sect. 5.7.

5.3 NUMERICAL METHODS

5.3.1 DUST EVOLUTION

We use the Monte Carlo method and representative particle approach first described by [Zsom & Dullemond \(2008\)](#) to model the dust evolution. We developed this method by adding an adaptive grid routine, which enables multi-dimensional models. The code was presented in Chapter 2. For this chapter, we focus on local models, only including the vertical dimension. We have already tested our code with such setups in Sect. 2.3.4 and we found a good agreement with the results of [Dullemond & Dominik \(2005\)](#) and [Zsom et al. \(2011a\)](#). We have also noticed that the adaptive grid routine allows us to obtain very high resolution of the midplane layer and thus to follow dust evolution in dead zones well.

The representative approach relies on assumption that the evolution of many dust particles can be resolved by following the evolution of only a limited number of so called representative particles. One representative particle is representing a swarm of identical physical particles. In our code, all the swarms have equal mass, thus the mass of one swarm M_{swarm} is an adequate fraction of the total dust mass M_{tot}

$$M_{\text{swarm}} = M_{\text{tot}}/N_{\text{swarms}}, \quad (5.1)$$

where N_{swarms} is number of representative particles, or swarms, present in our simulation (the approach restrictions are discussed in Chapter 4). The collisions between dust particles are modelled with a Monte Carlo algorithm, described in details in [Zsom & Dullemond \(2008\)](#) and Chapter 2 of this dissertation.

In the original code, the particles were influenced by the gas but the gas was not changing its state. Here, we assume that particles are active, i.e. we enable the back-reaction on gas. The effects of the back-reaction are implemented in a semi-analytical way. First, a very crude approach of implementing the turbulence triggered by the streaming instability was already made in the Chapter 2. However, that approach did not include the dust clumping and the possibility of planetesimal formation, which we include now. As we do not directly model the hydrodynamics of the gas, we cannot capture the two-fluid interactions explicitly. We model dust growth and settling, and

include the effects of back-reaction basing on results of the direct numerical simulations, that investigated the dynamics of dust grains in the midplane of protoplanetary disks, presented by [Bai & Stone \(2010a,c\)](#), and analytical model by [Takeuchi et al. \(2012\)](#). We describe this approach in Sect. 5.3.2.

The dust evolution in a protoplanetary disk is driven by its interactions with gas. We assume that the gas disk is described by the Minimum Mass Solar Nebula (henceforth MMSN) model proposed by [Hayashi \(1981b\)](#), where the surface density follows

$$\Sigma_{\text{g}} = 1700 \times \left(\frac{r}{\text{AU}} \right)^{-1.5} \text{ g cm}^{-2}, \quad (5.2)$$

where r is radial distance to the central star of mass $1 M_{\odot}$. The surface density of dust is parametrized by metallicity Z such that $\Sigma_{\text{d}} = Z \times \Sigma_{\text{g}}$. The vertical structure of the gas is described by the local hydrostatic equilibrium and thus the gas density follows

$$\rho_{\text{g}}(z) = \frac{\Sigma_{\text{g}}}{\sqrt{2\pi}H_{\text{g}}} \exp\left(\frac{-z^2}{2H_{\text{g}}^2}\right), \quad (5.3)$$

where z is distance to the midplane, $H_{\text{g}} = c_{\text{s}}/\Omega_{\text{K}}$ is the pressure scale height of gas, defined by the sound speed c_{s} and orbital frequency Ω_{K} . We assume an isothermal disk with temperature

$$T = 280 \times \left(\frac{r}{\text{AU}} \right)^{-0.5} \text{ K}. \quad (5.4)$$

To investigate dust particles dynamics, it is convenient to use the Stokes number defined as

$$\text{St} = t_{\text{s}}\Omega_{\text{K}}, \quad (5.5)$$

where t_{s} is stopping time of the dust particle. The stopping time of a particle determines the timescale that particle needs to adjust its velocity to the velocity of the surrounding gas. The exact expression that we use to compute the t_{s} depends on the particle radius, and we use the formulas given by [Weidenschilling \(1977a\)](#). The Stokes number can be used as a particle-gas coupling strength indicator. The particles with $\text{St} \ll 1$ are well coupled and follow the motion of the gas, whereas the particles with $\text{St} \gg 1$ are fully decoupled from the gas. The particles that have $\text{St} \approx 1$, sometimes called pebbles, are marginally coupled to the gas and suffer the most from this interaction by acquiring high drift and impact speeds. However, these are also the grains that can trigger the streaming instability and form planetesimals, what we investigate in this chapter.

5.3. NUMERICAL METHODS

In a laminar disk, dust settles due to the vertical component of the star gravity and gas drag. We use the vertical velocity that implements the damped oscillations of large grains, such that the sedimentation rate is consistent with the results of [Carballido et al. \(2011\)](#):

$$v_z = -z\Omega_K \frac{\text{St}}{1 + \text{St}^2}. \quad (5.6)$$

If turbulence is present, we use the α prescription ([Shakura & Sunyaev 1973](#)), and the turbulent mixing of dust is implemented as "random kicks" ([Ciesla 2010](#)). The height of dust layer is regulated by the turbulence strength and settling. Including orbital oscillations of grains with $\text{St} > 1$, we get the scale height of the dust layer ([Carballido et al. 2006](#); [Youdin & Lithwick 2007](#); [Carballido et al. 2011](#))

$$H_d = H_g \sqrt{\frac{\alpha}{\alpha + \text{St}}}. \quad (5.7)$$

The collisions between dust aggregates are driven by the Brownian motions, relative radial, transverse and vertical drift, and turbulence. Although we do not include the radial drift of particles explicitly, we keep the drift speeds as a source of impact velocities, to correctly capture the growth rates and collisional physics.

5.3.2 STREAMING INSTABILITY

In a laminar disk, all dust grains would settle to the midplane and form a very thin and gravitationally unstable midplane layer ([Nakagawa et al. 1981](#)). However, the shear between such a layer and gas triggers turbulence that maintains its height at a level that typically does not allow direct gravitational collapse. The strength of turbulence triggered by the midplane instability was recently investigated by [Takeuchi et al. \(2012\)](#). They estimated the turbulence efficiency from the energy supplied by the radial drift of dust. Irrespectively of the turbulence mechanism, which can be both the Kelvin-Helmholtz and streaming instability, they find that for particles with $\text{St} < 1$ the resulting turbulence strength can be parametrized with

$$\alpha = \left[(C_1 C_{\text{eff}} \eta Z)^{-2/3} + (C_2 C_{\text{eff}} \eta Z^{-1})^{-2} \right]^{-1} \text{St}, \quad (5.8)$$

where $C_1 = 1$, $C_2 = 1.6$, $C_{\text{eff}} = 0.19$. As derivation of this equation was based on the assumption that all dust grains have an equal size corresponding to one Stokes number St , in our implementation we take $\text{St} = \bar{\text{St}}$, a mass-weighted average Stokes number of all the particles. Parameter η is related to the gas

midplane pressure P_g gradient

$$\eta = \frac{1}{2\rho_g r \Omega_K^2} \frac{\partial P_g}{\partial r}. \quad (5.9)$$

It is useful to parametrize the pressure gradient as

$$\Pi = \frac{|\eta| v_K}{c_s}, \quad (5.10)$$

the ratio of maximum radial drift speed $|\eta|v_K$, with v_K being the orbital velocity, and the isothermal sound speed c_s .

[Bai & Stone \(2010a,c\)](#) (henceforth BS10) performed local two- and three-dimensional numerical simulations of particles and gas dynamics in the midplane of a protoplanetary disk using the Athena code, including gas as a fluid and dust as superparticles ([Bai & Stone 2010b](#)). Both the aerodynamic coupling and particles to gas feedback were included. Magnetic forces and self-gravity were ignored. BS10 focused on a laminar disk, where the turbulence is initially not present. They regulated the aggregates sizes by varying the minimum and maximum Stokes number of particles and assuming that each logarithmic particle size bin is represented by the same amount of mass. They found that the settling of particles triggers the streaming instability and the related turbulence maintained the particles height before the Kelvin-Helmholtz instability could emerge. The strength of this turbulence is comparable with the results of [Takeuchi et al. \(2012\)](#).

The most interesting property of the streaming instability in the planet formation context is its ability to concentrate dust particles in dense clumps. BS10 performed a parameter study, varying dust sizes, the dust-to-gas ratio and the pressure gradient, in order to define threshold conditions for the strong clumping, over the Roche density, which could lead to planetesimal formation. The grain size distributions used by BS10 had the minimum Stokes number of 10^{-4} and the maximum of 1. Analyzing the results of their runs, in particular the dense clumps composition, they concluded that the smallest particles needed to trigger such a strong clumping correspond to a critical Stokes number of $St_{\text{crit}} = 10^{-2}$ and that a super-solar dust abundance is required. They found that a higher vertically integrated dust-to-gas ratio Z_{tot} lowers the threshold abundance of large grains, as a high dust-to-gas ratio reduces the turbulence and makes it easier to form a dense midplane layer. They also found that the lower the radial pressure gradient, the more easily the streaming instability can be triggered, consistent with findings of [Johansen et al. \(2007\)](#).

The BS10 work suggests a critical total metallicity as a criterion for strong clumping and they find its value to be in range 0.02 – 0.07 for different values

5.3. NUMERICAL METHODS

of the pressure gradient and different sizes of dust grains. They assumed a flat mass distribution in logarithmic size bins in their models. In our runs, the size distribution is an outcome of the Monte Carlo dust coagulation modeling. In order to use the BS10 results in our code, we build a model relying on splitting the dust mass distribution in two parts: particles larger and smaller than the size corresponding to the critical value of the Stokes number $St_{\text{crit}} = 10^{-2}$. In our model, we calculate the metallicity $Z(St > 10^{-2})$ taking into account only the large grains, with Stokes number higher than $St_{\text{crit}} = 10^{-2}$:

$$Z(St > 10^{-2}) = \sum_{St > 10^{-2}} \frac{\Sigma_d(St)}{\Sigma_g}, \quad (5.11)$$

where $\Sigma_d(St)$ is dust surface density contributed by particles corresponding to a Stokes number St . If the abundance of large grains $Z(St > 10^{-2})$ is higher than a critical value Z_{crit} , we assume that clumping over the Roche density happens and planetesimal formation is possible.

The work of BS10 suggests that the value of Z_{crit} depends on the total metallicity Z_{tot} and the radial pressure gradient, which is parametrized with Π . We assume the dependence to be

$$Z_{\text{crit}} = a \times Z_{\text{tot}} + b \times \Pi + c. \quad (5.12)$$

In order to determine values of the parameters a , b , and c , we analyze the results presented by [Bai & Stone \(2010c\)](#). For each set of runs sharing the same size distribution and pressure support, we check what is the minimum total metallicity allowing for planetesimal formation. Then, we calculate the metallicity contributed by the large grains in these runs (Z_{crit}) and compare it to the total metallicity (Z_{tot}). By numerical fitting to the data, we find $a = -0.88$, $b = 0.912714$, and $c = 0.004125$. We present the fit and data extracted from [Bai & Stone \(2010c\)](#) in [Fig. 5.1](#). With these values, we find that the absolute minimum metallicity to trigger strong clumping, for the standard value of $\Pi = 0.05$, is $Z_{\text{crit}} = 0.026$ (assuming that all the particles are large), which is significantly higher than the standard solar value of 0.01. This result is consistent with findings of [Johansen et al. \(2009b\)](#).

Our planetesimal formation algorithm works as follows: at every advection time step of the Monte Carlo coagulation calculation, we check the mass distribution of grains produced by the interplay of settling and coagulation, and calculate the metallicity of large grains $Z(St > 10^{-2})$. If the $Z(St > 10^{-2})$ is higher than the threshold value of Z_{crit} , planetesimal formation may happen. We also check whether the dust-to-gas ratio in the midplane exceeds unity, as this is a general condition for the streaming instability to be triggered. If both the conditions are fulfilled, we remove some amount of our largest

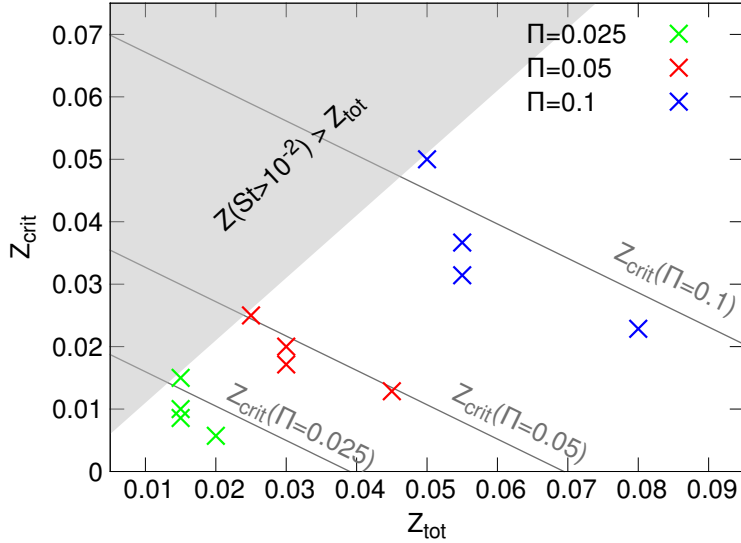


Figure 5.1: The critical metallicity of large aggregates necessary to trigger planetesimal formation as a function of total metallicity. The points present data obtained in direct numerical simulations by [Bai & Stone \(2010c\)](#) for three different values of the Π parameter. The lines show our fit to the data (Eq. 5.12). The shaded region is where the metallicity of large grains would be higher than the total one, which is not possible.

aggregates, which corresponds to an assumed mass of clump M_{clump} , from the dust coagulation code and refer to them as planetesimals. The evolution of the newly formed planetesimals is not included in the current version of the code.

The BS10 models did not include self-gravity, thus the formation of planetesimals was not followed. In our models, the amount of dust grains removed in one planetesimal-forming event is estimated with the mass of a collapsing clump

$$M_{\text{clump}} = \rho_d^0 \times H_d^3, \quad (5.13)$$

where ρ_d^0 is dust density in the midplane and H_d is vertical scale-height of the dust. For MMSN at 5 AU, we get $M_{\text{clump}} \approx 10^{22}$ g, which corresponds to 100 km-sized planetesimals with the internal density of 1 g cm^{-3} , consistent with constraints from the asteroid belt ([Morbidelli et al. 2009](#)). Eq. 5.13 presents a very crude order-of-magnitude estimate based on the typical height of the dust layer, which is resulting from the interplay of settling and the turbulence driven by the streaming instability (Eqs. 5.7 and 5.8). In reality,

the streaming instability forms elongated filaments that fragment to form planetesimals. Recently, [Yang & Johansen \(2014\)](#) estimated the width of the filaments from direct numerical simulations to be on the order of $10^{-2} \times H_g$, which is consistent with our H_d estimate (for $St = 10^{-2}$ and $\alpha = 10^{-6}$). In their simulations, the filaments include dust of density $\sim 10^2 \times \rho_g^0$, where ρ_g^0 is the gas density in the midplane. As in our models $\rho_d^0 \gtrsim \rho_g^0$, the M_{clump} estimated by [Yang & Johansen \(2014\)](#) would be by 2 orders of magnitude higher than calculated from the Eq. 5.13. Nevertheless, we find that the final outcome of our models does not depend on the exact value of the M_{clump} as long as there are no resolution issues coming into play.

To avoid the resolution issues, we take care that the mass represented by one swarm M_{swarm} (Eq. 5.1) is lower than the mass of the collapsing clump M_{clump} , meaning that we remove more than one representative particle to account for collapse of one clump. Thanks to this, the amount of dust removed in one step is not too high. At the same time, we need the M_{swarm} to be higher than a maximum mass of aggregate possible to produce with coagulation, which can be estimated thanks to Eq. (5.14). The representative particles approach only works when the physical particles are less massive than the mass of one swarm. This is because of the assumption that one swarm represents multiple physical particles.

5.4 PRELIMINARY ESTIMATES

We investigate whether the dust coagulation can produce aggregates that are large enough to trigger strong clumping in the streaming instability, which can then lead to planetesimal formation, and model the planetesimal formation when it is possible. We present results of our numerical simulations in Sect. 5.5, but first we motivate our choice of parameter space with simple estimates.

The size of dust grains possible to obtain by coagulation is limited by numerous effects, such as collisional physics and radial drift. On the other hand, existence of the large grains is crucial for the streaming instability and subsequent planetesimal formation.

The maximum size of aggregates depends mainly on the critical velocity above which particles do not stick. Fragmentation velocities of silicate aggregates are measured in laboratory experiments to be in range of a few tens cm s^{-1} to a few m s^{-1} , while bouncing collisions already happen at velocities of a few cm s^{-1} ([Güttler et al. 2010](#); [Seizinger & Kley 2013](#); [Kelling et al. 2014](#)). The collision outcome is known to depend strongly on the porosity and porous grains may be able to grow even at velocities of 30 m s^{-1} ([Wada et al. 2011](#); [Meru et al. 2013b](#)). However, numerical models including the porosity

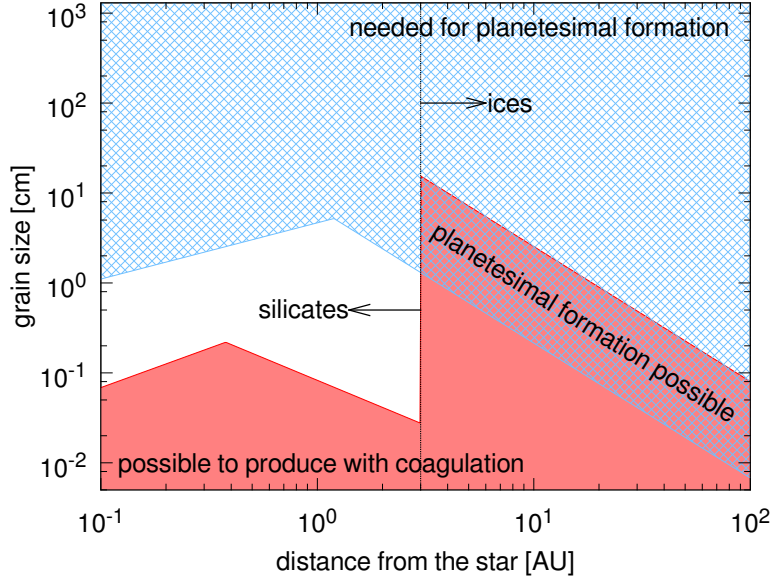


Figure 5.2: Comparison of maximum dust particles size possible to obtain with coagulation (the red shaded region) and minimum size needed for planetesimal formation in a dead zone (the blue crosshatched region). We assume that particle growth is limited by the relative drift velocities, ignoring turbulence, which corresponds to the dead zone. We find that the maximum particle size exceeds the size corresponding to the $St = 10^{-2}$ only for the ices that can exist beyond the snow line, where the presence of ice makes the dust particle more sticky.

have shown that the porous silicate grains will be collisionally compacted and the growth will be halted by bouncing (Zsom et al. 2010). The dust grains consisting of ices are considered to be significantly more sticky and resistant against compaction (Okuzumi et al. 2012; Kataoka et al. 2013b; Aumatell & Wurm 2014). However, as the laboratory experiments involving ices are more challenging than for silicate grains, there is still no detailed collision model for such grains. In the molecular dynamics models, ice grains are found to be very porous and able to grow even at velocities of 50 m s^{-1} (Wada et al. 2009).

To account for the difference in growth efficiency of silicates and ices in our simple model, we assume a different critical velocity for growth inside and outside the snow line. For the silicate particles present inside the snow line (located at 3 AU in this model) we assume the impact velocity for bouncing/fragmentation of $v_{\text{in}} = 10 \text{ cm s}^{-1}$ and for the icy particle $v_{\text{out}} = 10 \text{ m s}^{-1}$.

As we place our models in a dead zone, we do not consider turbulence as

a source of impact velocities. The impact velocities are thus determined by relative drift, which can be parametrized by η (Eq. 5.9). Besides the bouncing and fragmentation, maximum size of grains can also be restricted by removal of material with radial drift. However, we find that for the enhanced dust abundance, which is prerequisite for an efficient streaming instability, the growth rate is enhanced as well, and the drift barrier does not influence the maximum size of grains, as it would only occur for particles larger than the size limited by fragmentation. We neglect the removal of material by the radial drift in this chapter.

The maximum Stokes number of aggregates resulting from the collisions driven by relative drift can be estimated as (Birnstiel et al. 2012)

$$\text{St}_{\text{max}} \approx \frac{v_f}{|\eta|v_K}. \quad (5.14)$$

We plot the size of aggregates corresponding to the St_{max} and the critical value of $\text{St}_{\text{crit}} = 10^{-2}$ in the laminar MMSN disk in Fig. 5.2. In other words: Fig. 5.2 shows where the dust growth can produce aggregates that are large enough to trigger the streaming instability. We find that to obtain grains with $\text{St} > 10^{-2}$, the velocity v_f has to be typically higher than $\sim 1 \text{ m s}^{-1}$. Thus, obtaining the particles of $\text{St} > 10^{-2}$ is very hard inside the snow line, where the growth of silicate particles is halted by bouncing. However, it should be relatively easy in regions where solid ice can exist. The snow line location is fixed at 3 AU in the simple model presented in this section. In a realistic disk, the snow line migrates with time (Davis 2005; Min et al. 2011; Martin & Livio 2012; Bitsch et al. 2014). If the snow line moves inwards, the region where planetesimals can form extends.

5.5 RESULTS

We use our dust evolution code together with the planetesimal formation prescription described in Sect. 5.3 to model dust coagulation and planetesimal formation in a dead zone of the MMSN disk. Motivated by the estimates presented in the previous section, which show that the streaming instability can only form planetesimals outside the snow line, we locate our numerical models at 5 AU, where the cores of giant planets in the Solar System were presumably formed. We assume that the dust aggregates have internal density of $\rho_p = 1 \text{ g cm}^{-3}$ and we treat them as compact spheres. The dust grains have an initial size of $1 \mu\text{m}$ and are distributed such that the dust-to-gas ratio is constant within the whole vertical range. We let the grains stick and fragment as well as settle down towards the midplane and be stirred by turbulence triggered by the streaming instability when the dust-to-gas ratio in

the midplane reaches unity. Fragmentation occurs for collisions with impact speeds higher than a critical value v_f . All our runs have vertical resolution of 100 grid cells and we place 400 representative particles in each cell. For such resolution, we only find minor differences between runs started with identical parameters but different random seeds, as is usually practiced for Monte Carlo methods.

5.5.1 FIDUCIAL RUN

For our fiducial run we choose $\Pi = 0.05$, corresponding to a pressure gradient slightly reduced with respect to the nominal MMSN model, where $\Pi \approx 0.08$ at 5 AU. However, this value is matching a more realistic disk model presented by [Chiang & Youdin \(2010\)](#). In general, the value of Π increases with the radial distance from the star. In the MMSN model $\Pi \approx 0.055 \times (r/\text{AU})^{1/4}$, whereas in the [Chiang & Youdin \(2010\)](#) model $\Pi \approx 0.036 \times (r/\text{AU})^{2/7}$. We start the run with the vertically integrated dust-to-gas ratio of $Z = 0.05$, factor of five higher than the usual solar metallicity. For the impact velocity above which the particles fragment, we take $v_f = 1000 \text{ cm s}^{-1}$. Such setup could correspond to a pressure trap induced by a long-lived zonal flow ([Dittrich et al. 2013](#)).

Figure 5.3 shows the evolution of grain size distribution in the fiducial run. For comparison, we also show the evolution of the same run but without the planetesimal formation algorithm enabled. Typical sedimentation driven coagulation scenario happens: the equal-sized particles initially grow slowly thanks to the Brownian motions. Then, the particles in the upper layers start to grow much faster than those in the midplane, because the settling velocities increase with height (Eq. 5.6). The largest aggregates sweep-up smaller particles while they settle down and thus further increase their settling velocity, resulting in formation of a bimodal size distribution at ~ 600 yrs. Then, the particles encounter the fragmentation barrier and a coagulation-fragmentation equilibrium develops, leading to a power law like size distribution. The slope of the distribution depends on mass distribution of fragments implemented. We implement the fragment distribution $n(m) dm \propto m^{-11/6} dm$, corresponding to the MRN distribution ([Mathis et al. 1977](#)). We find that the coagulation-fragmentation equilibrium in the dead zone, where collisions are mainly driven by the systematic drift, leads to size distribution

$$n(a) \cdot a \cdot m d\log a \propto a^{1/2} d\log a, \quad (5.15)$$

visible in the bottom panel of Fig. 5.3.

The evolution proceeds identically in both cases: with and without planetesimal formation, until ~ 1000 yrs. After this time, both the conditions

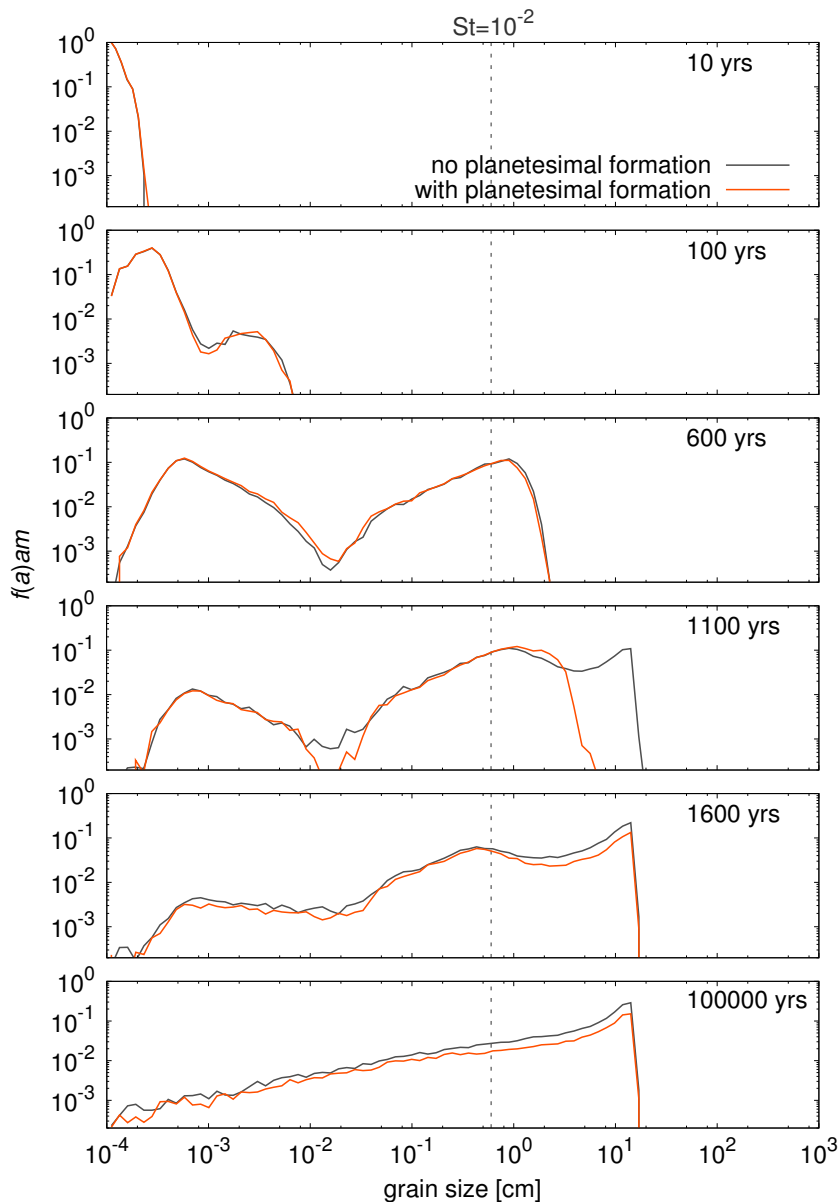


Figure 5.3: Time evolution of the dust size distribution in our fiducial run with and without the planetesimal formation by streaming instability enabled. The vertical dashed line indicates grain size corresponding to Stokes number of 10^{-2} . Larger grains can form planetesimals and be removed from the simulation.

described in Sect. 5.3.2 are fulfilled and some particles are removed to account for the planetesimal formation. Removing the large grains slows down the collisional evolution, which may be noticed in the fourth panel of Fig. 5.3. This is because the missing large grains possessed very high interaction rates and would normally participate in many collisions. However, this effect is quickly smeared out by the development of the coagulation-fragmentation equilibrium. The final difference between the size distributions is not very pronounced.

Figure 5.4 presents an extended overview of the fiducial run time evolution. Panel a) presents how the dust and planetesimals abundance changes with time. Planetesimal formation starts at $t \sim 990$ years and lasts $\sim 6 \times 10^4$ years. Planetesimal formation efficiency decreases over time. Panels b) and c) correspond to the two conditions that have to be fulfilled simultaneously to allow the planetesimal formation: high metallicity in the form of large grains ($Z(\text{St} > 10^{-2}) > Z_{\text{crit}}$) and the midplane dust-to-gas ratio higher than unity. In the presented case, the first condition is fulfilled already at $t \sim 700$ years, but the settling takes an additional ~ 300 years which delays the onset of planetesimal formation. The large amount of large grains already present results in a planetesimal formation outburst: around 40% of the final amount of planetesimals is formed in the first planetesimal-forming step. After this, the turbulence generated by the streaming instability stirs the midplane layer below the threshold dust density again. Interplay of growth and settling leads to refilling the large grains reservoir. Each time a clump is removed, the total metallicity Z_{tot} decreases and the threshold metallicity Z_{crit} increases (Eq. 5.12). After $\sim 6 \times 10^4$ years, Z_{crit} is so high that the coagulation cannot produce enough of large grains and the planetesimal formation is not possible anymore.

The fact that the sedimentation takes longer than growth up to the required sizes is not a general rule. In some of the other runs, presented in the following section, we observe the opposite relation: the growth takes longer than settling. This is because both the timescales are comparable in the dead zone case. Thanks to this, the sedimentation driven coagulation may happen, where the growth and settling timescales for the rain-out particles are equal.

It is worth noting that the modeling of sedimentation driven coagulation requires including the vertical structure. The sedimentation driven coagulation determines the initial timescale of growth. The process we describe cannot be modeled in detail using vertically integrated algorithms, which assume that equilibrium between vertical settling and mixing is reached on a timescale shorter than growth timescale. We find that the planetesimal formation starts before such equilibrium is reached.

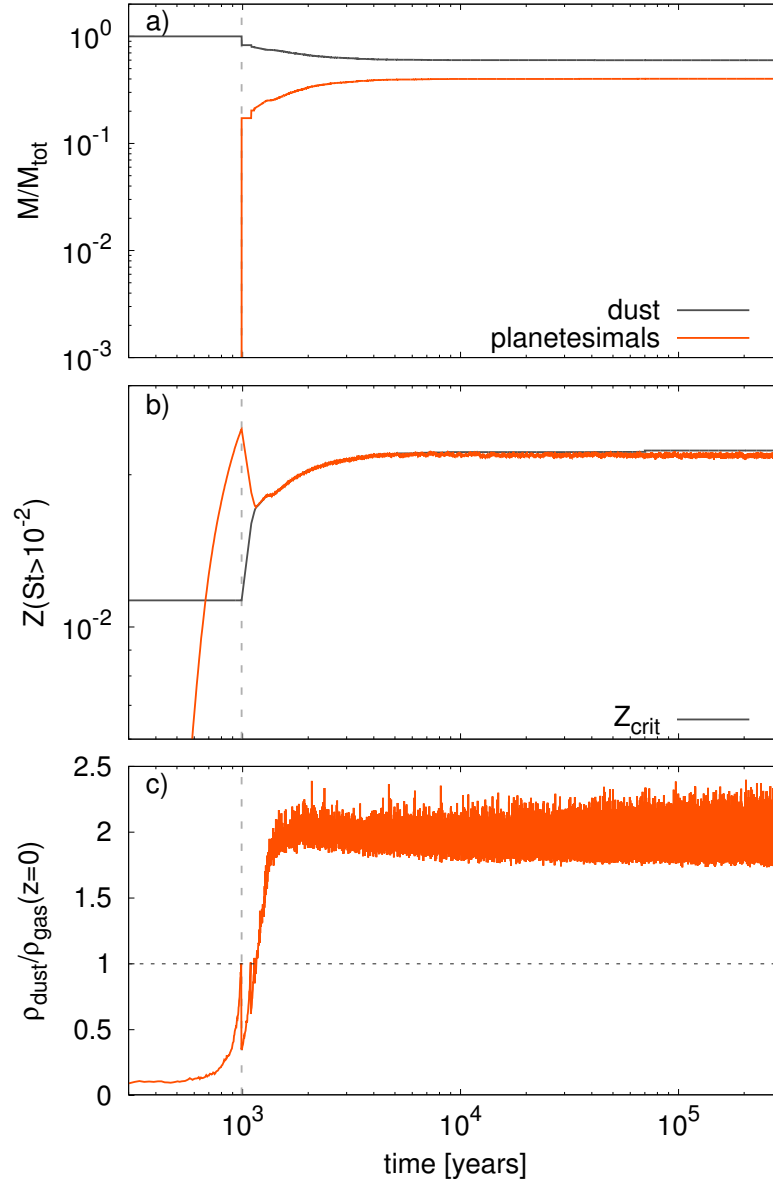


Figure 5.4: Time evolution of our fiducial run: a) total planetesimal and dust mass, b) ratio of the surface density of particles larger than $\text{St} = 10^{-2}$ to the gas density compared to the threshold value Z_{crit} , c) dust-to-gas ratio in the midplane compared to the threshold value of unity. The dashed vertical line corresponds to the time when first planetesimals are formed. It can be seen that although the metallicity of large grains was higher than Z_{crit} already at $t \sim 700$ years (b), the planetesimal formation only starts at $t \sim 990$ years (a), because the large grains were not settled to the midplane yet (c).

5.5.2 PARAMETER STUDY

In order to check how our results depend on the choice of parameters, we vary the fragmentation velocity v_f , the pressure gradient Π , and the total vertically integrated metallicity Z_{tot} . We perform 24 runs in total. Table 5.1 gives overview of the parameter values used in our simulations and their results in terms of how much dust is turned into planetesimals and how long do we have to wait for the planetesimal formation to be triggered. Our fiducial run is referred to as P5Z5V1000 in this table. Different panels of Fig. 5.5 show how the planetesimal formation changes when one of the parameters is varied from its fiducial value. We discuss the parameter dependencies further in this section.

DEPENDENCE ON RADIAL PRESSURE GRADIENT

Both Johansen et al. (2007) and Bai & Stone (2010c) observed that with a lower pressure gradient it is easier to trigger the planetesimal formation. This effect may seem counterintuitive, as the streaming instability is driven by the existence of the pressure gradient and the sub-Keplerian rotation of gas. However, the radial pressure gradient provides free energy that triggers the turbulence, therefore, a lower pressure gradient weakens the turbulence and promotes particle settling to higher densities (see Eq. 5.8). In our model, the radial pressure gradient is parametrized by Π (Eq. 5.10). Based on the BS10 results, the critical metallicity for planetesimal formation, Z_{crit} , is dependent on Π such that a lower pressure gradient promotes planetesimal formation (Eq. 5.12). What is more, with a lower Π , the collision speeds between particles are also lower and thus the maximum particle size and the corresponding Stokes number (St_{max}) are higher. This is because, as seen in Eq. (5.14), the maximum Stokes number we can obtain is inversely proportional to the maximum radial drift velocity, which is proportional to the radial pressure gradient. With the two effects adding up, the effect of the radial pressure gradient is very strong. As can be seen in panel a) of Fig. 5.5, lowering the pressure gradient by 60% results in more than 80% increase in amount of planetesimals that can be formed. On the other hand, by increasing the gradient by 60%, we get a dramatic decrease in the amount of planetesimals produced: from 40% to only 5% of initial mass of dust.

DEPENDENCE ON METALLICITY

Increasing the total amount of dust available has a positive effect on the amount of planetesimals that are formed. First of all, higher total metallicity directly translates into a larger amount of large grains ($Z(\text{St} > 10^{-2})$) that can participate in the strong clumping that can lead to planetesimal formation. As seen in Eq. (5.12), higher total dust abundance lowers the critical

Table 5.1: Overview of parameters used and results obtained in different runs: columns (a)-(c) correspond to the parameters used in each run, columns (d)-(e) to their results

Run name	Π^a	Z_{tot}^b	v_f^c	$M_{\text{plts}}/M_{\text{tot}}^d$	t_{plts}^e
P2Z7V5000			5000	83%	60
P2Z7V1000	0.02	0.07	1000	80%	64
P2Z7V100			100	78%	174
P2Z5V5000			5000	77%	85
P2Z5V1000	0.02	0.05	1000	73%	88
P2Z5V100			100	68%	212
P2Z3V5000			5000	61%	147
P2Z3V1000	0.02	0.03	1000	54%	151
P2Z3V100			100	47%	275
P5Z7V5000			5000	64%	59
P5Z7V1000	0.05	0.07	1000	57%	63
P5Z7V100			100	43%	175
P5Z5V5000			5000	50%	83
P5Z5V1000	0.05	0.05	1000	40%	88
P5Z5V100			100	20%	227
P5Z3V5000			5000	16%	233
P5Z3V1000	0.05	0.03	1000	0.8%	693
P5Z3V100			100	0%	-
P8Z7V5000			5000	35%	56
P8Z7V1000	0.08	0.07	1000	32%	61
P8Z7V100			100	0%	-
P8Z5V5000			5000	9%	125
P8Z5V1000	0.08	0.05	1000	5%	201
P8Z5V100			100	0%	-

^a Radial pressure gradient measure (Eq. 5.10)

^b Total metallicity

^c Fragmentation velocity in cm s^{-1}

^d Total final mass of planetesimals produced with respect to the initial total mass of dust

^e Time when the planetesimal formation started in local orbital timescales

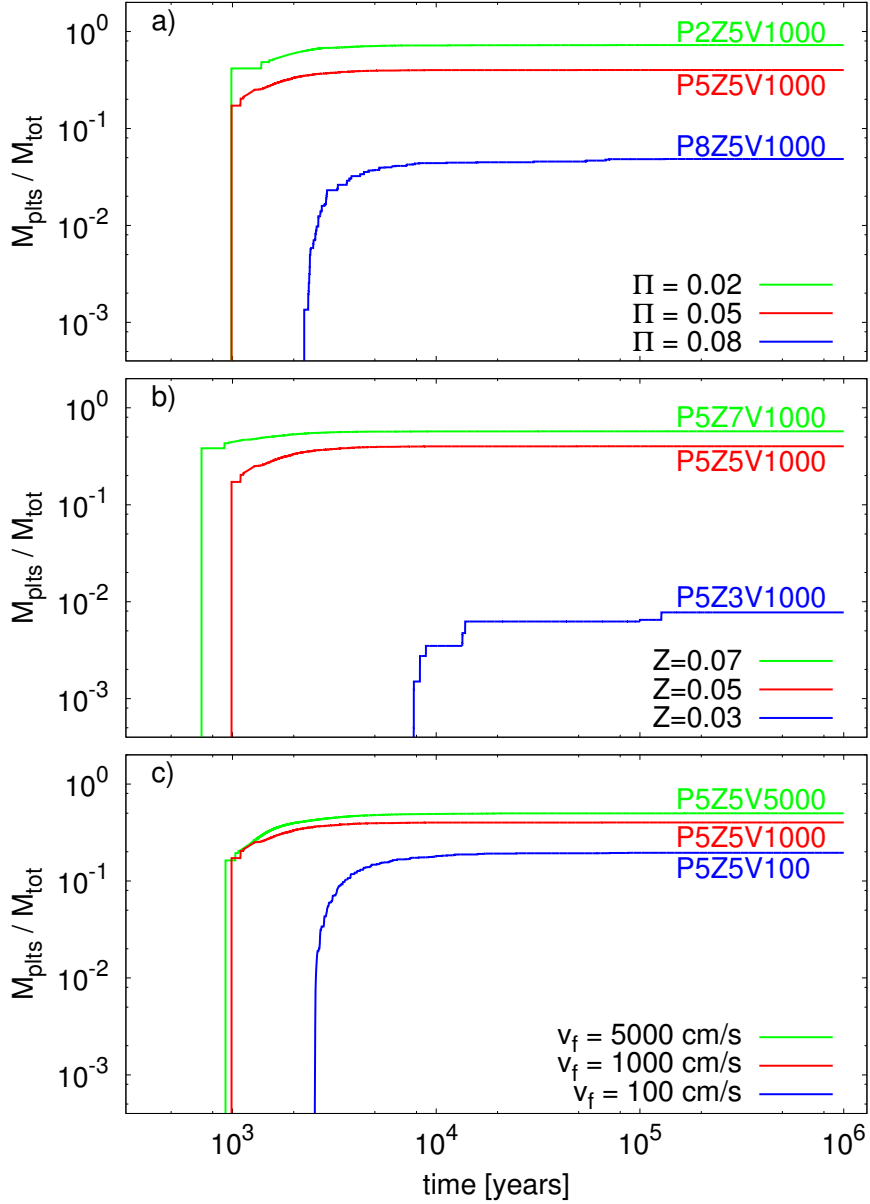


Figure 5.5: Planetesimal formation in our runs depends on parameters: a) radial pressure gradient parametrized by Π (Eq. 5.10), b) total metallicity Z_{tot} , c) fragmentation velocity v_f . The red line in each panel corresponds to our fiducial run P5Z5V1000.

vertically integrated dust-to-gas ratio Z_{crit} . This is because the higher dust abundance reduces the turbulence triggered by the instability (Eq. 5.8) and thus makes the clumping easier. The higher dust-to-gas ratio in the mid-plane also leads to a faster rotation of the gas and reduction of the difference between the gas and Keplerian rotation (Bai & Stone 2010a). This has similar effect as reduction of the radial pressure gradient, which facilitates the planetesimal formation, as discussed above. Finally, the higher metallicity speeds up the growth and makes the planetesimal formation able to start earlier, as the growth timescale scales inversely with the vertically integrated dust-to-gas ratio (Birnstiel et al. 2012):

$$\tau_{\text{growth}} \propto (Z_{\text{tot}} v_{\text{K}})^{-1}, \quad (5.16)$$

where v_{K} is the Keplerian velocity. In fact, we observe that with metallicity $Z_{\text{tot}} > 0.03$, the growth proceeds so quickly, that it is the settling timescales which determines the onset of planetesimal formation. Such effect takes place in our fiducial run P5Z5V1000. With these positive effects adding up, metallicity is influencing the amount of planetesimals formed very strongly. However, the impact of metallicity is nonlinear: increasing it by 40% results in >40% increase in the amount of planetesimals formed, but decreasing it by 40% with respect to the fiducial value results in almost no planetesimals being formed (panel b of Fig. 5.5). The strong dependence on the vertically integrated dust-to-gas ratio is consistent with results of direct numerical simulations (Johansen et al. 2009b; Bai & Stone 2010a).

DEPENDENCE ON FRAGMENTATION VELOCITY

Dependence on the fragmentation velocity is the most straightforward. The value of v_{f} only influences the maximum size of particles we are able to obtain by coagulation. The maximum Stokes number St_{max} increases proportionally to the fragmentation velocity, as can be seen in Eq. (5.14). The higher the fragmentation velocity, the more grains will have Stokes number above the critical value ($\text{St}_{\text{crit}} > 10^{-2}$), and it is easier to reach the condition of the high metallicity of large grains ($Z(\text{St} > 10^{-2}) > Z_{\text{crit}}$). We present the dependence of our results on the fragmentation velocity in panel c) of Fig. 5.5. For the chosen values, the v_{f} is not influencing the outcome as strongly as the other two parameters. However, as we show in Sect. 5.4, with even lower fragmentation velocities we would not be able to produce any grains larger than the critical size. We conclude that, due to the fact that for the chosen fragmentation law the large grains possess most of the mass, the fragmentation velocity does not influence the amount of planetesimals that can be formed much as long as it enables growing grains with the Stokes number $\text{St} > 10^{-2}$ at all.

5.5.3 ANALYTICAL MODEL

We presented results of our numerical simulations following interplay between coagulation and planetesimal formation under different conditions in the disk. In this section, we construct a relatively simple formula that estimates the results, computing the efficiency of planetesimal formation in terms of the pressure gradient, initial vertically integrated dust-to-gas ratio and fragmentation velocity.

As we describe previous sections, the key property determining whether the planetesimal formation is possible is the amount of dust grains with Stokes number lather than the critical value $St_{\text{crit}} = 10^{-2}$. If the Stokes number of the largest grains possible to produce by coagulation is $St_{\text{max}} > St_{\text{crit}}$, the amount of grains of interesting sizes can be estimated taking into account the dust mass distribution. The mass distribution we obtain when the coagulation and fragmentation are in equilibrium is described with Eq. (5.15). We emphasize that this particular slope is a result of the chosen distribution of fragments, which was described in Sect. 5.5.1.

Taking into account that $m \propto St^3$ (in the Epstein drag regime, which applies to the small grains that we obtain in our simulations) and $d \log m = dm/m$, we can rewrite the size distribution (Eq. 5.15) in terms of the Stokes number

$$n(St) \cdot m \, dSt \propto St^{-1/2} \, dSt. \quad (5.17)$$

The relative amount of dust above a critical Stokes number St_{crit} is

$$\frac{Z(St > 10^{-2})}{Z_{\text{tot}}} = \frac{\int_{St_{\text{crit}}}^{St_{\text{max}}} n(St)m \, dSt}{\int_{St_{\text{min}}}^{St_{\text{max}}} n(St)m \, dSt} = \frac{\sqrt{St_{\text{max}}} - \sqrt{St_{\text{crit}}}}{\sqrt{St_{\text{max}}} - \sqrt{St_{\text{min}}}}. \quad (5.18)$$

The minimum Stokes number St_{min} is in principle determined by the size of monomers, and for μm -sized grains $St_{\text{min}} \approx 10^{-6}$. The maximum Stokes number St_{max} is determined by the fragmentation velocity v_f and the impact speeds. In the dead zone case, collisions are mainly driven by radial, azimuthal and vertical drift and the maximum size of grains is estimated well by Eq. (5.14). We assume the critical Stokes number of $St_{\text{crit}} = 10^{-2}$, as discussed in Sect. 5.3.2.

The planetesimal formation happens as long as the abundance of large grains is higher than critical ($Z(St > 10^{-2}) > Z_{\text{crit}}$). The threshold abundance Z_{crit} is dependent on the pressure gradient Π and the total metallicity Z_{tot} , as described with Eq. (5.12). When planetesimals are produced, the total metallicity decreases and thus the critical metallicity increases. The planetesimal formation stops when the amount of large grains, corresponding to $Z(St > 10^{-2})$ cannot reach the threshold value Z_{crit} anymore. Taking into

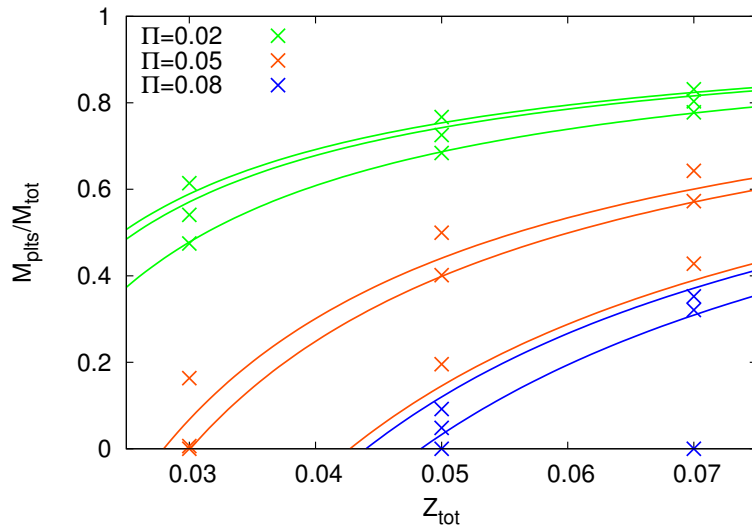


Figure 5.6: Comparison of the mass in planetesimal as a function of total metallicity obtained in different runs (points) and predicted by our analytical model (lines). The three different colors correspond to different values of the pressure gradient parameter Π . The three lines of the same colors correspond to different values of the fragmentation velocity used. For $\Pi = 0.08$ and $v_f = 100 \text{ cm s}^{-1}$, there is no planetesimal formation predicted, thus the line is not visible.

account the ratio of the mass included in large grains to the total mass resulting from the equilibrium mass distribution (Eq. 5.18), we can derive a critical total vertically integrated dust-to-gas ratio $Z_{\text{tot,crit}}$, below which planetesimal formation is not possible anymore. Using Eqs. (5.12) and (5.18), we obtain

$$Z_{\text{tot,crit}} = (b\Pi + c) \times \left(\frac{\sqrt{\text{St}_{\text{max}}} - \sqrt{\text{St}_{\text{crit}}}}{\sqrt{\text{St}_{\text{max}}} - \sqrt{\text{St}_{\text{min}}}} - a \right)^{-1}. \quad (5.19)$$

The values of a , b , and c are given in Sect. 5.3.2, and the values of the Stokes numbers are discussed under Eq. (5.18).

The end of the planetesimal formation phase happens when the total metallicity Z_{tot} has dropped below the critical total metallicity $Z_{\text{tot,crit}}$ and the relative amount of planetesimals produced $M_{\text{plts}}/M_{\text{tot}}$ can be estimated as

$$\frac{M_{\text{plts}}}{M_{\text{tot}}} = \frac{Z_{\text{tot},0} - Z_{\text{tot,crit}}}{Z_{\text{tot},0}}. \quad (5.20)$$

Figure 5.6 shows comparison of the relative planetesimal mass produced, $M_{\text{plts}}/M_{\text{tot}}$, obtained with Eq. (5.20) and measured in our simulations (Ta-

ble 5.1). The efficiency of planetesimal formation given by Eq. (5.20) tends to slightly underestimate the results of our simulations. We associate this with the mass distribution peak around maximum grain size visible in the bottom panel of Fig. 5.3, which is not covered by the simple power law (Eq. 5.17) that we used to derive Eq. (5.20). This peak arises because of the fragmentation barrier: particles that grow mostly in roughly similar-sized collisions, suddenly lack slightly larger collision partners. In order to sustain a steady state, the particles pile-up around the maximum size (Birnstiel et al. 2011).

5.6 DISCUSSION

The work we presented includes some inevitable assumptions. In this section, we discuss uncertainties contributed by these assumptions as well as possible ways to improve our work.

The collision model used in our work is highly simplified, restricting all the collision physics to one key parameter: the fragmentation velocity v_f . What is more, we assume that all the dust grains are spherical and compact, with a constant internal density. It is known that the internal structure of grains is important to the coagulation (Ormel et al. 2007; Okuzumi et al. 2009; Meru et al. 2013b) and dynamics (Okuzumi et al. 2012; Hubbard & Ebel 2014). However, we lack reliable models of icy aggregates porosity, as laboratory experiments including the ices are particularly challenging. Our work may be improved in future, as soon as laboratory data on collisions of icy aggregates are available.

Our streaming instability model relies on the work of BS10 and thus inherits all its uncertainties. Probably the highest uncertainty is contributed by the fact that we use their 2-D simulations results, as due to computational expense reasons, the extended parameter study was performed in 2-D only. BS10 reported that conditions for the strong clumping are more stringent in 3-D than in 2-D, thus our model may be too optimistic. On the other hand, the BS10 models do not include the particle's self-gravity, which might help to obtain strong clumping for lower metallicity or higher pressure gradient. This is because with the self-gravity a dust clump is able to collapse even if its initial density is lower than the Roche density (Michikoshi et al. 2010).

BS10 reported that their runs saturate within ~ 50 -100 orbits. This is the time the dust needs to settle and the streaming instability needs to develop. The settling timescale is self-consistently included in our models, but we neglect the time the streaming instability needs to develop: we assume the streaming instability is able to produce planetesimals immediately after the dust is settled and a sufficient amount of large grains is present. We motivate this assumption by the fact that the timescale of dust coagulation

is typically longer than the timescale to develop the instability. What is more, the timescale for clump collapse measured in simulations that include self-gravity is very short, of the order of one orbit (Johansen et al. 2011).

BS10 assumed a flat mass distribution in logarithmic bins in the Stokes number, whereas in our models the mass distribution is a result of realistic coagulation-fragmentation cycle and roughly follows the power-law described with Eq. (5.15). The model we built to overcome the issue of incompatible size distributions relies on splitting the dust mass into particles larger and smaller than a size corresponding to the $St_{\text{crit}} = 10^{-2}$. We assume that the large particles are actively driving the instability and participating in clumps, and fit the dependence of critical abundance of the large aggregates on the total metallicity (Sect. 5.3.2, Fig. 5.1). Both the choice of a constant value of St_{crit} , and our fits should be rather treated as first approximation. Given the limited data of the BS10 papers, this is the best we can do. This model may be improved as soon as more detailed parameter studies of the streaming instability become available. What is necessary is a more systematic parameter scan of the 3-D streaming instability models, ideally going hand-in-hand with results from coagulation models to ensure that realistic particle size distributions are used in these 3-D models.

The BS10 results are restricted to laminar disk, without the turbulence, opposed to the work of Johansen et al. (2007). It is known that some source of viscosity is necessary as a mechanism of the angular momentum transport, which enables the disk accretion on observed timescales (Shakura & Sunyaev 1973). The magnetorotational instability (MRI) was considered as a mechanism to drive turbulence that is a source of such viscosity (Balbus & Hawley 1991). Thus, neglecting the turbulence may seem a serious restriction. However, many models of protoplanetary disks suggest that large regions of the disks can be free from the MRI (Gammie 1996; Turner et al. 2007; Dzyurkevich et al. 2013). In this picture, the midplane is quiescent, but the upper layers may still be active. The turbulence from the active layers may stir the midplane, which we neglect in this chapter. Recently it was shown that the MRI is inefficient or even completely suppressed in the inner regions of disks when all the non-ideal magnetohydrodynamic effects, such as the ambipolar diffusion and the Hall effect, are taken into account (Bai 2013, 2014; Lesur et al. 2014). The typical extent of such dead zone is from 1 AU to 10 AU, which covers the planetesimal formation region we investigate. Thanks to the existence of a dead zone, the planetesimals can not only form, but also avoid destructive collisions and grow by the runaway growth (Gressel et al. 2011, 2012; Ormel & Okuzumi 2013). The evolution of the planetesimals and their interaction with the remaining dust is not yet included in our model.

The extent of the dead zone is regulated by the amount of small dust

grains, whose large surface-to-mass ratio enables sweep-up of free electrons from the gas and thus decrease the ionisation (Sano et al. 2000; Ilgner & Nelson 2006). In the case of efficient growth of dust grains, the dead zone vanishes (Okuzumi 2009; Okuzumi & Hirose 2012). In our model, we neglect the dead zone evolution, but as we keep a significant number of small grains because of the fragmentation barrier, we consider this a safe approach.

We place our models at 5 AU, relying on our estimates, which show that it is not possible to grow sufficiently large grains out of silicate aggregates, when the bouncing barrier is acting (Sect. 5.4). It was shown that the bouncing barrier can be overcome and large grains can grow when the fragmentation with mass transfer effect is taken into account (Windmark et al. 2012b; Garaud et al. 2013; Drażkowska et al. 2014). However, the impact velocity distribution that is necessary to produce the seed grains in those papers is contributed by the MRI turbulence, which is not present in a dead zone. The MRI turbulence would make it harder to trigger the streaming instability, as it does not allow to form a very thin midplane layer. Thus, the sweep-up growth scenario may be operating and forming planetesimals preferentially in the active zone of protoplanetary disk, whereas the scenario we investigate in this chapter works better in the dead zone.

Another possibility of forming sufficiently large aggregates inside the snow line is co-accretion of dust and chondrules suggested by Ormel et al. (2008), and subsequently investigated in laboratory experiments by Beitz et al. (2012) and Jankowski et al. (2012). In this scenario, chondrules acquire dusty rims that facilitate their sticking and allow to overcome the bouncing barrier. As shown by Ormel et al. (2008), this scenario requires moderately low turbulence, which would also be favorable for the streaming instability.

Our models are local and neglect the radial drift. The radial drift timescale for pebbles of $St = 10^{-2}$ at 5 AU is on the order of 10^3 orbits, which is one order of magnitude longer than the coagulation needs to trigger the streaming instability, thus we consider this a safe approach.

We assume that metallicity is enhanced over the standard solar value of 0.01. Such enhancement could form in a radial drift dominated disk, where the pebbles necessary to trigger the streaming instability are drifting inwards and may form pile-ups, as suggested by Youdin & Shu (2002), Youdin & Chiang (2004), Laibe et al. (2012), and Laibe (2014). However, such enhancement typically happens inside the snow line, where growing sufficiently large particles is suppressed by the non-stickiness of aggregates and the existing large aggregates may be destroyed by ice evaporation and high speed collisions. A way to overcome this problem may be the reduction of impact speeds in presence of strong dust-to-gas ratio enhancements (Nakagawa et al. 1986; Bai & Stone 2010a), which is not yet included in our code. The reduction

of impact speeds would help to form larger aggregates and thus to produce more planetesimals.

Another possibility that would justify the enhanced metallicity and the reduced pressure support at the same time is existence of some kind of pressure bump. However, the formation process and lifetime of such pressure bumps remains uncertain. Pressure bumps caused by zonal flows have been observed in numerical simulations including the MRI turbulence (Johansen et al. 2009a; Dzyurkevich et al. 2010; Uribe et al. 2011), but their lifetimes are up to 50 orbits (Dittrich et al. 2013). a pressure bump arising around the snow line was suggested by Kretke & Lin (2007), but it was recently found to require an unrealistically high viscosity transition (Bitsch et al. 2014). What is more, complicated evaporation and condensation processes have to be taken into account to model the size evolution of dust (Kuroiwa & Sirono 2011) when considering the region near the snow line. Thus, our model is not self consistent in the pressure bump and dust enhancement origin aspect: we start our runs with metallicity already enhanced by a factor of a few with respect to a nominal solar value, as otherwise the planetesimal formation by streaming instability is not possible. We investigate the interplay between vertical settling, coagulation and planetesimal formation, ignoring the radial drift of dust. Such enhancement would in reality build up over timescale determined by the radial drift, even in a presence of pre-existing pressure bump. We plan to investigate the effects of radial drift on our results in future work.

The sizes of clumps and planetesimals created by the streaming instability are highly uncertain, as the hydrodynamic simulations have limited resolution and are typically not able to follow the clump collapse with realistic collisional behaviour. As described in Sect. 5.3.2, we assume that the collapsing clumps have identical mass, which is estimated based on the height of dust layer (Eq. 5.13). This is only an order-of-magnitude estimate, which is not necessarily consistent with the recent results of Yang & Johansen (2014), as discussed in Sect. 5.3.2. However, we find that, although the details of evolution are dependent on the assumed clump mass, the final outcome in terms of total planetesimal mass produced is not.

5.7 CONCLUSIONS

The streaming instability was proposed as an efficient way of overcoming the growth and drift barriers and forming planetesimals. However, strong clumping was proven to require large grains. In this chapter, we investigated whether such large grains can form in sufficient amount during coagulation under realistic conditions. We developed and implemented a simplified model for planetesimal formation into our dust coagulation code, as described in

Sect. 5.3. Our work is a step toward a unified model for planetesimal formation, as we join the dust coagulation modeling with planetesimal formation via streaming instability for the first time.

We find that planetesimal formation by streaming instability is hindered for the silicate aggregates because the bouncing barrier prevents growth to the sizes (Stokes numbers) needed to trigger the streaming instability. The minimum size of particles, corresponding to the critical Stokes number ($St_{\text{crit}} = 10^{-2}$), is possible to obtain for the more sticky, icy aggregates, which are present beyond the snow line. If some way can be found to overcome the bouncing barrier, we can expect the streaming instability to operate also inside the snow line. However, the strong clumping may only be triggered when the vertically integrated dust-to-gas ratio is enhanced by a factor of at least three with respect to the solar value of 0.01 or/and the radial pressure gradient is reduced with respect to the standard Minimum Mass Solar Nebula model. What is more, a dense midplane layer of solids have to be formed, which is only possible if the turbulence is relatively weak.

We modeled the interplay of dust coagulation and settling and planetesimal formation and performed a parameter study, varying the radial pressure gradient, metallicity and fragmentation velocity. We investigated how these values influence the amount of planetesimals formed. We proposed a simple explanation of the obtained results, by constructing an analytical expression for the maximum amount of dust that can be turned into planetesimals (Sect. 5.5.3). This model can be used in future projects, for example to constrain initial conditions for planetesimal evolution models or in planet population synthesis codes.

5.7. CONCLUSIONS

6

SUMMARY

The work presented in this dissertation is focused on the planetesimal formation problem. Several scenarios leading to formation of the km-sized objects, which are the building blocks of planets, were explored and their efficiency can now be compared.

In Chapters 3 and 4, we investigated planetesimal formation via the sweep-up growth triggered by the radial mixing of aggregates in the vicinity of the inner edge of dead zone and the impact velocity distribution respectively. In both the cases, the amount of dust turned to planetesimals is low, on the order of 1% of the total dust mass. Slightly more planetesimals can possibly be formed in the streaming instability scenario, which is discussed in Chapter 5. In Sect. 5.5.3, we derived a closed-form expression for the relative mass of planetesimals that can be formed via the streaming instability. The exact amount is dependent on the local properties of the protoplanetary disk. As this scenario requires some special conditions, like an enhanced dust-to-gas ratio and reduced pressure support, it is very hard to say what will be a realistic value of the planetesimals-to-dust ratio produced. Nevertheless, it is reasonable to assume that, similarly to the sweep-up growth case, the streaming instability is not very efficient in turning dust to planetesimals. This statement is consistent with the results of direct numerical simulations: e.g. [Johansen et al. \(2007\)](#) reported that around 10% of all the pebbles present in their runs were bound in the planetesimals, and similar value was obtained in the higher resolution simulations presented by [Johansen et al. \(2011\)](#). The values quoted here refer to local models and can be treated as an upper limit of the planetesimal formation efficiency in a global disk.

The fact that the planetesimal formation in each of the scenarios that we investigated is not very efficient, is consistent with the protoplanetary disk observations. Small dust grains are observed even in disks that are millions of years old. With our results, we have now reasons to believe that the planetesimals, which cannot be directly observed, are already existing in the midplane of these disks.

The circumstellar disk masses used in the state-of-the-art models are usually based on observational estimates, which are relying on measuring the dust mass in the outer parts of the disks and converting it to mass of gas by assuming the standard dust-to-gas ratio of 1%, or on the Minimum Mass Solar Nebula proposed by [Weidenschilling \(1977b\)](#) and [Hayashi \(1981a\)](#). The Minimum Mass Solar Nebula estimates are based on the amount of heavy elements that are present in the current Solar System. However, as we show in our models, the conversion rate of dust into planetesimals, and thus presumably planets, is certainly lower than 100%. Consequently, the primordial solar nebula was probably more massive than estimated by this model. Similar point may be made for the protoplanetary disks observations. It is only possible to measure the dust in the outer parts of the disks, but these are expected to be significantly depleted because of the radial drift barrier (see Sect. 1.3.3, in particular Fig. 1.9) and the possible existence of larger bodies. Thus, assuming the constant dust-to-gas ratio of 1% may lead to underestimating the mass of the disk. A similar point was made by [Birnstiel et al. \(2012\)](#).

Another conclusion that emerges from our results is that the formation of planetesimals is not possible in all the locations in the disk, because it is hindered by the growth barriers. Planetesimal formation via subsequent growth, discussed in Chapters 3 and 4, has to be supported by the mass transfer collisions, and some "lucky" particles have to be introduced by one process or another. Interplay between the growth and drift makes it difficult to grow planetesimals in the outer parts of the disk, where the drift barrier is more pronounced. Nevertheless, forming planetesimals via the sweep-up growth is possible in the inner part of the disk, where the growth timescale is shorter than the drift timescale, or in some privileged places, like a pressure bump. On the other hand, the streaming instability scenario discussed in Chapter 5 prefers the outer part of the disk, where existence of the icy aggregates facilitates growing sufficiently large pebbles. What is more, the streaming instability only works if a relatively dense midplane layer can be formed and the dust-to-gas ratio in the midplane exceeds unity. Thus, a moderately low turbulence is required to form planetesimals in this scenario. In contrast, the sweep-up growth scenario works better with a stronger turbulence because the turbulence contributes the impact velocity distribution that enables breaking through the growth barriers.

The work presented in this dissertation, besides the scientific content, includes many technical aspects. First of all, a new numerical method for dust evolution modeling was developed, which is described in Chapter 2. A significant improvement over the previous 1-D method presented by [Zsom et al. \(2011a\)](#) was made by introducing the adaptive grid approach (Sect. 2.2.4)

and by extending this method to 2-D. This code was already used in the work presented in Chapters 3 – 5, and there are still many possible projects that it can be used for. In Chapter 4, for the first time we have directly compared the two most popular dust coagulation modeling approaches: the Monte Carlo method and the Smoluchowski equation approach. This work gives a valuable insight into the limitations of these methods in the context of planetesimal formation modeling and reveals several pitfalls that can result in nonphysical results.

The work presented in this dissertation includes important steps towards a self-consistent planet formation model. Quantifying the amount of planetesimals and the timescale for their formation is important in the context of the late stages of planet formation modeling. Previous models of this kind were usually assuming that the planetesimals and planetary embryos can form anywhere in the disk with a high efficiency. These models were however not successful in reproducing at least some properties of both the Solar System and the extrasolar planets. In the Solar System, the low mass of Mars issue is a good example. As discussed in Sect. 4.6.3, the observed mass of Mars cannot be explained by the final assembly of terrestrial planets from a homogeneous planetesimal disk. Instead, it is possible to reproduce it if the planetesimals are located inside of 1 AU (Hansen 2009). A standard explanation for such cutoff is the Grand Tack scenario involving inwards migration of Jupiter, but the sweep-up and pile-up possibility presented in Sect. 4.6.3 may be a more natural solution. In the exoplanets case, there is the population of systems with tightly-packed inner planets that is hard to explain with the planet migration scenario (Lithwick & Wu 2012). The fact that the large bodies can only grow in the inner part of the protoplanetary disk implies an in situ formation of these systems.

Although the low efficiency of planetesimal formation implied by our results may seem disturbing in the context of the giant planet cores formation, which has to be sufficiently quick in order to allow accretion of the gaseous atmospheres, a way around this problem has been discovered recently. The classical scenario of runaway and oligarchic growth has been challenged by the pebble accretion scenario (Lambrechts & Johansen 2012, Sect. 1.3.5), which offers much faster growth of the embryos given a relatively large abundance of cm-sized pebbles. Recent work of Kretke & Levison (2014) shows that the pebble accretion is even too efficient to reproduce the formation of the Solar System. However, the pebble sizes used in that work are generally not consistent with dust coagulation models. A self-consistent model joining the dust evolution, planetesimal formation and pebble accretion is needed to get insight into this problem. We believe that the results presented in this dissertation may be developed to such model.

BIBLIOGRAPHY

- A'Hearn, M. F. 2008, *Space Sci. Rev.*, 138, 237
- A'Hearn, M. F., Belton, M. J. S., Delamere, W. A., et al. 2005, *Science*, 310, 258
- Albertsson, T., Semenov, D., & Henning, T. 2014, *ApJ*, 784, 39
- Alexander, C. M. O. ., Grossman, J. N., Ebel, D. S., & Ciesla, F. J. 2008, *Science*, 320, 1617
- Alexander, R. D. & Armitage, P. J. 2007, *MNRAS*, 375, 500
- Andrews, S. M. & Williams, J. P. 2007a, *ApJ*, 671, 1800
- Andrews, S. M. & Williams, J. P. 2007b, *ApJ*, 659, 705
- Aumatell, G. & Wurm, G. 2014, *MNRAS*, 437, 690
- Bai, X.-N. 2013, *ApJ*, 772, 96
- Bai, X.-N. 2014, *ApJ*, 791, 137
- Bai, X.-N. & Stone, J. M. 2010a, *ApJ*, 722, 1437
- Bai, X.-N. & Stone, J. M. 2010b, *ApJS*, 190, 297
- Bai, X.-N. & Stone, J. M. 2010c, *ApJ*, 722, L220
- Balbus, S. A. & Hawley, J. F. 1991, *ApJ*, 376, 214
- Balsara, D. S., Tilley, D. A., Rettig, T., & Brittain, S. D. 2009, *MNRAS*, 397, 24
- Barge, P. & Sommeria, J. 1995, *A&A*, 295, L1
- Barranco, J. A. 2009, *ApJ*, 691, 907
- Baruteau, C., Crida, A., Paardekooper, S.-J., et al. 2013, arXiv:1312.4293
- Beaugé, C. & Nesvorný, D. 2012, *ApJ*, 751, 119
- Beitz, E., Güttler, C., Blum, J., et al. 2011, *ApJ*, 736, 34
- Beitz, E., Güttler, C., Weidling, R., & Blum, J. 2012, *Icarus*, 218, 701
- Benz, W. & Asphaug, E. 1999, *Icarus*, 142, 5
- Binzel, R. P., Lupishko, D., di Martino, M., Whiteley, R. J., & Hahn, G. J. 2002, *Asteroids III*, 255
- Birnstiel, T., Dullemond, C. P., & Brauer, F. 2010, *A&A*, 513, A79
- Birnstiel, T., Klahr, H., & Ercolano, B. 2012, *A&A*, 539, A148
- Birnstiel, T., Ormel, C. W., & Dullemond, C. P. 2011, *A&A*, 525, A11
- Bitsch, B., Morbidelli, A., Lega, E., Kretke, K., & Crida, A. 2014, arXiv:1408.1016
- Blum, J. & Münch, M. 1993, *Icarus*, 106, 151
- Blum, J., Schräpler, R., Davidsson, B. J. R., & Trigo-Rodríguez, J. M. 2006, *ApJ*, 652, 1768

BIBLIOGRAPHY

- Blum, J. & Wurm, G. 2008, *ARA&A*, 46, 21
- Boss, A. P. 1997, *Science*, 276, 1836
- Boss, A. P. & Durisen, R. H. 2005, *ApJ*, 621, L137
- Bottke, W. F., Durda, D. D., Nesvorný, D., et al. 2005, *Icarus*, 175, 111
- Bracco, A., Chavanis, P. H., Provenzale, A., & Spiegel, E. A. 1999, *Physics of Fluids*, 11, 2280
- Brauer, F., Dullemond, C. P., & Henning, T. 2008a, *A&A*, 480, 859
- Brauer, F., Dullemond, C. P., Johansen, A., et al. 2007, *A&A*, 469, 1169
- Brauer, F., Henning, T., & Dullemond, C. P. 2008b, *A&A*, 487, L1
- Bromley, B. C. & Kenyon, S. J. 2006, *AJ*, 131, 2737
- Brownlee, D. E., Horz, F., Newburn, R. L., et al. 2004, *Science*, 304, 1764
- Brucker, M. J., Grundy, W. M., Stansberry, J. A., et al. 2009, *Icarus*, 201, 284
- Bryden, G., Chen, X., Lin, D. N. C., Nelson, R. P., & Papaloizou, J. C. B. 1999, *ApJ*, 514, 344
- Carballido, A., Bai, X.-N., & Cuzzi, J. N. 2011, *MNRAS*, 415, 93
- Carballido, A., Fromang, S., & Papaloizou, J. 2006, *MNRAS*, 373, 1633
- Cassan, A., Kubas, D., Beaulieu, J.-P., et al. 2012, *Nature*, 481, 167
- Chabrier, G., Johansen, A., Janson, M., & Rafikov, R. 2014, arXiv:1401.7559
- Chambers, J. 2006, *Icarus*, 180, 496
- Chambers, J. E. 2010, *Icarus*, 208, 505
- Chambers, J. E. 2014, *Icarus*, 233, 83
- Charnoz, S. & Taillifet, E. 2012, *ApJ*, 753, 119
- Chatterjee, S. & Tan, J. C. 2014, *ApJ*, 780, 53
- Chiang, E. & Laughlin, G. 2013, *MNRAS*, 431, 3444
- Chiang, E. & Youdin, A. N. 2010, *Annual Review of Earth and Planetary Sciences*, 38, 493
- Ciesla, F. J. 2010, *ApJ*, 723, 514
- Ciesla, F. J. & Hood, L. L. 2002, *Icarus*, 158, 281
- Cieza, L. A., Padgett, D. L., Allen, L. E., et al. 2009, *ApJ*, 696, L84
- Connelly, J. N., Bizzarro, M., Krot, A. N., et al. 2012, *Science*, 338, 651
- Correia, A. C. M., Udry, S., Mayor, M., et al. 2008, *A&A*, 479, 271
- Cuzzi, J. N., Dobrovolskis, A. R., & Champney, J. M. 1993, *Icarus*, 106, 102
- Cuzzi, J. N., Hogan, R. C., & Bottke, W. F. 2010, *Icarus*, 208, 518
- Cuzzi, J. N., Hogan, R. C., Paque, J. M., & Dobrovolskis, A. R. 2001, *ApJ*, 546, 496
- Cuzzi, J. N., Hogan, R. C., & Shariff, K. 2008, *ApJ*, 687, 1432
- Cuzzi, J. N. & Zahnle, K. J. 2004, *ApJ*, 614, 490

BIBLIOGRAPHY

- D'Angelo, G. & Lubow, S. H. 2008, *ApJ*, 685, 560
- Dauphas, N., Robert, F., & Marty, B. 2000, *Icarus*, 148, 508
- Davis, S. S. 2005, *ApJ*, 620, 994
- Delsemme, A. H. 1991, *Origins of Life and Evolution of the Biosphere*, 21, 279
- Desch, S. J. 2007, *ApJ*, 671, 878
- Desch, S. J. & Connolly, Jr., H. C. 2002, *Meteoritics and Planetary Science*, 37, 183
- Desidera, S. & Barbieri, M. 2007, *A&A*, 462, 345
- Dittrich, K., Klahr, H., & Johansen, A. 2013, *ApJ*, 763, 117
- Doyle, L. R., Carter, J. A., Fabrycky, D. C., et al. 2011, *Science*, 333, 1602
- Drażkowska, J., Windmark, F., & Dullemond, C. P. 2013, *A&A*, 556, A37
- Drażkowska, J., Windmark, F., & Dullemond, C. P. 2014, *A&A*, 567, A38
- Dubrulle, B., Morfill, G., & Sterzik, M. 1995, *Icarus*, 114, 237
- Duffell, P. C. & MacFadyen, A. I. 2013, *ApJ*, 769, 41
- Dullemond, C. P. & Dominik, C. 2004, *A&A*, 421, 1075
- Dullemond, C. P. & Dominik, C. 2005, *A&A*, 434, 971
- Dullemond, C. P., Stammer, S. M., & Johansen, A. 2014, *The Astrophysical Journal*, 794, 91
- Duquennoy, A. & Mayor, M. 1991, *A&A*, 248, 485
- Dzyurkevich, N., Flock, M., Turner, N. J., Klahr, H., & Henning, T. 2010, *A&A*, 515, A70
- Dzyurkevich, N., Turner, N. J., Henning, T., & Kley, W. 2013, *ApJ*, 765, 114
- Epstein, P. S. 1924, *Physical Review*, 23, 710
- Fang, J. & Margot, J.-L. 2012, *ApJ*, 761, 92
- Ferrière, K. M. 2001, *Reviews of Modern Physics*, 73, 1031
- Fessler, J. R., Kulick, J. D., & Eaton, J. K. 1994, *Physics of Fluids*, 6, 3742
- Flynn, G. J. 2008, *Earth Moon and Planets*, 102, 447
- Gail, H.-P., Tieloff, M., Breuer, D., & Spohn, T. 2013, arXiv:1312.3509
- Gammie, C. F. 1996, *ApJ*, 457, 355
- Garaud, P. 2007, *ApJ*, 671, 2091
- Garaud, P., Meru, F., Galvagni, M., & Olczak, C. 2013, *ApJ*, 764, 146
- Gaudi, B. S. 2012, *ARA&A*, 50, 411
- Giannini, E. & Lunine, J. I. 2013, *Reports on Progress in Physics*, 76, 056901
- Gillespie, D. T. 1975, *J. Atmos. Sci.*, 32, 1977
- Glaschke, P., Amaro-Seoane, P., & Spurzem, R. 2011, arXiv:1105.6094
- Goldreich, P. 1965, *Nature*, 208, 375
- Goldreich, P. & Ward, W. R. 1973, *ApJ*, 183, 1051

BIBLIOGRAPHY

- Gomes, R., Levison, H. F., Tsiganis, K., & Morbidelli, A. 2005, *Nature*, 435, 466
- Goodman, J. & Pindor, B. 2000, *Icarus*, 148, 537
- Gressel, O., Nelson, R. P., & Turner, N. J. 2011, *MNRAS*, 415, 3291
- Gressel, O., Nelson, R. P., & Turner, N. J. 2012, *MNRAS*, 422, 1140
- Güttler, C., Blum, J., Zsom, A., Ormel, C. W., & Dullemond, C. P. 2010, *A&A*, 513, A56
- Güttler, C., Poppe, T., Wasson, J. T., & Blum, J. 2008, *Icarus*, 195, 504
- Haghighipour, N. 2005, *MNRAS*, 362, 1015
- Haghighipour, N., ed. 2010, *Astrophysics and Space Science Library*, Vol. 366, *Planets in Binary Star Systems*
- Haghighipour, N. & Boss, A. P. 2003a, *ApJ*, 598, 1301
- Haghighipour, N. & Boss, A. P. 2003b, *ApJ*, 583, 996
- Hansen, B. M. S. 2009, *ApJ*, 703, 1131
- Hansen, B. M. S. 2014, *MNRAS*, 440, 3545
- Hayashi, C. 1981a, *Progress of Theoretical Physics Supplement*, 70, 35
- Hayashi, C. 1981b, *Progress of Theoretical Physics Supplement*, 70, 35
- Hernández, J., Hartmann, L., Megeath, T., et al. 2007, *ApJ*, 662, 1067
- Hewins, R. H., Connolly, H. C., Lofgren, G. E. J., & Libourel, G. 2005, in *Astronomical Society of the Pacific Conference Series*, Vol. 341, *Chondrites and the Protoplanetary Disk*, ed. A. N. Krot, E. R. D. Scott, & B. Reipurth, 286
- Holman, M. J. & Wisdom, J. 1993, *AJ*, 105, 1987
- Hood, L. L. 1998, *Meteoritics and Planetary Science*, 33, 97
- Horch, E. P., Howell, S. B., Everett, M. E., & Ciardi, D. R. 2014, arXiv:1409.1249
- Hubbard, A. & Ebel, D. S. 2014, *Icarus*, 237, 84
- Hubickyj, O., Bodenheimer, P., & Lissauer, J. J. 2005, *Icarus*, 179, 415
- Ilgner, M. & Nelson, R. P. 2006, *A&A*, 445, 205
- Ingrosso, G., Novati, S. C., de Paolis, F., et al. 2009, *MNRAS*, 399, 219
- Izidoro, A., de Souza Torres, K., Winter, O. C., & Haghighipour, N. 2013, *ApJ*, 767, 54
- Izidoro, A., Haghighipour, N., Winter, O. C., & Tsuchida, M. 2014, *ApJ*, 782, 31
- Jacquet, E. 2014, *Icarus*, 232, 176
- Jacquet, E., Balbus, S., & Latter, H. 2011, *MNRAS*, 415, 3591
- Jankowski, T., Wurm, G., Kelling, T., et al. 2012, *A&A*, 542, A80
- Johansen, A., Blum, J., Tanaka, H., et al. 2014, arXiv:1402.1344

BIBLIOGRAPHY

- Johansen, A., Henning, T., & Klahr, H. 2006, *ApJ*, 643, 1219
- Johansen, A., Klahr, H., & Henning, T. 2011, *A&A*, 529, A62
- Johansen, A., Oishi, J. S., Mac Low, M.-M., et al. 2007, *Nature*, 448, 1022
- Johansen, A., Youdin, A., & Klahr, H. 2009a, *ApJ*, 697, 1269
- Johansen, A., Youdin, A., & Mac Low, M.-M. 2009b, *ApJ*, 704, L75
- Johansen, A., Youdin, A. N., & Lithwick, Y. 2012, *A&A*, 537, A125
- Kataoka, A., Tanaka, H., Okuzumi, S., & Wada, K. 2013a, *A&A*, 557, L4
- Kataoka, A., Tanaka, H., Okuzumi, S., & Wada, K. 2013b, *A&A*, 554, A4
- Kelling, T., Wurm, G., & Köster, M. 2014, *ApJ*, 783, 111
- Kenyon, S. J. & Hartmann, L. 1987, *ApJ*, 323, 714
- Klahr, H. & Bodenheimer, P. 2006, *ApJ*, 639, 432
- Klahr, H. H. & Henning, T. 1997, *Icarus*, 128, 213
- Kley, W. & Nelson, R. P. 2012, *ARA&A*, 50, 211
- Kokubo, E. & Ida, S. 2000, *Icarus*, 143, 15
- Kolmogorov, A. 1941, *Akademiia Nauk SSSR Doklady*, 30, 301
- Kothe, S., Blum, J., Weidling, R., & Güttler, C. 2013, *Icarus*, 225, 75
- Kothe, S., Güttler, C., & Blum, J. 2010, *ApJ*, 725, 1242
- Kovetz, A. & Olund, B. 1969, *Journal of Atmospheric Sciences*, 26, 1060
- Kowalik, K., Hanasz, M., Wóltański, D., & Gawryszczak, A. 2013, *MNRAS*, 434, 1460
- Kretke, K. A. & Levison, H. F. 2014, arXiv:1409.4430
- Kretke, K. A. & Lin, D. N. C. 2007, *ApJ*, 664, L55
- Kuebler, K. E., McSween, H. Y., Carlson, W. D., & Hirsch, D. 1999, *Icarus*, 141, 96
- Kuroiwa, T. & Sirono, S.-i. 2011, *ApJ*, 739, 18
- Lada, C. J. 2006, *ApJ*, 640, L63
- Laibe, G. 2014, *MNRAS*, 437, 3037
- Laibe, G., Gonzalez, J.-F., & Maddison, S. T. 2012, *A&A*, 537, A61
- Laibe, G. & Price, D. J. 2014, *MNRAS*, 444, 1940
- Lambrechts, M. & Johansen, A. 2012, *A&A*, 544, A32
- Lammel, C. 2008, Bachelor's thesis, Technische Universität Carolo Wilhelmina Braunschweig
- Langkowski, D., Teiser, J., & Blum, J. 2008, *ApJ*, 675, 764
- Lee, J. W., Youn, J.-H., Lee, C.-U., Kim, S.-L., & Koch, R. H. 2009, *AJ*, 138, 478
- Lee, M. H. 2000, *Icarus*, 143, 74
- Lesur, G., Kunz, M. W., & Fromang, S. 2014, *A&A*, 566, A56
- Levison, H. F., Dones, L., Chapman, C. R., et al. 2001, *Icarus*, 151, 286

BIBLIOGRAPHY

- Levison, H. F., Morbidelli, A., Tsiganis, K., Nesvorný, D., & Gomes, R. 2011, *AJ*, 142, 152
- Levison, H. F., Thommes, E., & Duncan, M. J. 2010, *AJ*, 139, 1297
- Lithwick, Y. 2014, *ApJ*, 780, 22
- Lithwick, Y. & Wu, Y. 2012, *ApJ*, 756, L11
- Lyra, W., Johansen, A., Zsom, A., Klahr, H., & Piskunov, N. 2009, *A&A*, 497, 869
- Martin, R. G. & Livio, M. 2012, *MNRAS*, 425, L6
- Martin, R. G. & Livio, M. 2013, *MNRAS*, 428, L11
- Masset, F. S. & Papaloizou, J. C. B. 2003, *ApJ*, 588, 494
- Mathis, J. S., Rumpl, W., & Nordsieck, K. H. 1977, *ApJ*, 217, 425
- Matzel, J. E. P., Ishii, H. A., Joswiak, D., et al. 2010, *Science*, 328, 483
- Mayer, L., Quinn, T., Wadsley, J., & Stadel, J. 2002, *Science*, 298, 1756
- Mayor, M. & Queloz, D. 1995, *Nature*, 378, 355
- Meakin, P. & Donn, B. 1988, *ApJ*, 329, L39
- Meheut, H., Casse, F., Varniere, P., & Tagger, M. 2010, *A&A*, 516, A31
- Meisner, T., Wurm, G., Teiser, J., & Schywek, M. 2013, *A&A*, 559, A123
- Meru, F., Galvagni, M., & Olczak, C. 2013a, *ApJ*, 774, L4
- Meru, F., Geretshauser, R. J., Schäfer, C., Speith, R., & Kley, W. 2013b, *MNRAS*, 435, 2371
- Metropolis, N. & Ulam, S. 1949, *Journal of the American Statistical Association*, 44, pp. 335
- Michikoshi, S., Kokubo, E., & Inutsuka, S.-i. 2010, *ApJ*, 719, 1021
- Michikoshi, S., Kokubo, E., & Inutsuka, S.-i. 2012, *ApJ*, 746, 35
- Min, M., Dullemond, C. P., Kama, M., & Dominik, C. 2011, *Icarus*, 212, 416
- Morbidelli, A., Bottke, W. F., Nesvorný, D., & Levison, H. F. 2009, *Icarus*, 204, 558
- Morbidelli, A., Brasser, R., Gomes, R., Levison, H. F., & Tsiganis, K. 2010, *AJ*, 140, 1391
- Morris, M. A., Boley, A. C., Desch, S. J., & Athanassiadou, T. 2012, *ApJ*, 752, 27
- Mostefaoui, S., Kita, N. T., Togashi, S., et al. 2002, *Meteoritics and Planetary Science*, 37, 421
- Nakagawa, Y., Nakazawa, K., & Hayashi, C. 1981, *Icarus*, 45, 517
- Nakagawa, Y., Sekiya, M., & Hayashi, C. 1986, *Icarus*, 67, 375
- Nakamura, R. & Hidaka, Y. 1998, *A&A*, 340, 329
- Naoz, S., Farr, W. M., Lithwick, Y., Rasio, F. A., & Teyssandier, J. 2011, *Nature*, 473, 187

BIBLIOGRAPHY

- Nesvorný, D. & Morbidelli, A. 2008, *ApJ*, 688, 636
- Neuhäuser, R. & Schmidt, T. O. B. 2012, arXiv:1201.3537
- Nomura, H. & Nakagawa, Y. 2006, *ApJ*, 640, 1099
- O'Brien, D. P., Walsh, K. J., Morbidelli, A., Raymond, S. N., & Mandell, A. M. 2014, *Icarus*, 239, 74
- Ohtsuki, K., Nakagawa, Y., & Nakazawa, K. 1990, *Icarus*, 83, 205
- Okuzumi, S. 2009, *ApJ*, 698, 1122
- Okuzumi, S. & Hirose, S. 2012, *ApJ*, 753, L8
- Okuzumi, S., Tanaka, H., Kobayashi, H., & Wada, K. 2012, *ApJ*, 752, 106
- Okuzumi, S., Tanaka, H., & Sakagami, M.-a. 2009, *ApJ*, 707, 1247
- Okuzumi, S., Tanaka, H., Takeuchi, T., & Sakagami, M.-a. 2011a, *ApJ*, 731, 95
- Okuzumi, S., Tanaka, H., Takeuchi, T., & Sakagami, M.-a. 2011b, *ApJ*, 731, 95
- Ormel, C. W. & Cuzzi, J. N. 2007, *A&A*, 466, 413
- Ormel, C. W., Cuzzi, J. N., & Tielens, A. G. G. M. 2008, *ApJ*, 679, 1588
- Ormel, C. W., Dullemond, C. P., & Spaans, M. 2010, *Icarus*, 210, 507
- Ormel, C. W. & Klahr, H. H. 2010, *A&A*, 520, A43
- Ormel, C. W. & Kobayashi, H. 2012, *ApJ*, 747, 115
- Ormel, C. W. & Okuzumi, S. 2013, *ApJ*, 771, 44
- Ormel, C. W. & Spaans, M. 2008, *ApJ*, 684, 1291
- Ormel, C. W., Spaans, M., & Tielens, A. G. G. M. 2007, *A&A*, 461, 215
- Ossenkopf, V. 1993, *A&A*, 280, 617
- Ostriker, E. C. & Shu, F. H. 1995, *ApJ*, 447, 813
- Pagani, L., Steinacker, J., Bacmann, A., Stutz, A., & Henning, T. 2010, *Science*, 329, 1622
- Pan, L. & Padoan, P. 2013, *ApJ*, 776, 12
- Pan, L., Padoan, P., & Scalo, J. 2014a, *ApJ*, 791, 48
- Pan, L., Padoan, P., & Scalo, J. 2014b, *ApJ*, 792, 69
- Pilipp, W., Hartquist, T. W., Morfill, G. E., & Levy, E. H. 1998, *A&A*, 331, 121
- Pinilla, P., Benisty, M., & Birnstiel, T. 2012a, *A&A*, 545, A81
- Pinilla, P., Birnstiel, T., Benisty, M., et al. 2013, *A&A*, 554, A95
- Pinilla, P., Birnstiel, T., Ricci, L., et al. 2012b, *A&A*, 538, A114
- Pollack, J. B., Hubickyj, O., Bodenheimer, P., et al. 1996, *Icarus*, 124, 62
- Queloz, D., Mayor, M., Weber, L., et al. 2000, *A&A*, 354, 99
- Quintana, E. V., Adams, F. C., Lissauer, J. J., & Chambers, J. E. 2007, *ApJ*, 660, 807

BIBLIOGRAPHY

- Rafikov, R. R. 2001, *AJ*, 122, 2713
- Rafikov, R. R. 2005, *ApJ*, 621, L69
- Raymond, S. N. & Cossou, C. 2014, *MNRAS*, 440, L11
- Raymond, S. N., O'Brien, D. P., Morbidelli, A., & Kaib, N. A. 2009, *Icarus*, 203, 644
- Rein, H. 2012, *MNRAS*, 427, L21
- Richardson, J. E., Melosh, H. J., Lisse, C. M., & Carcich, B. 2007, *Icarus*, 191, 176
- Ros, K. & Johansen, A. 2013, *A&A*, 552, A137
- Sano, T., Miyama, S. M., Umebayashi, T., & Nakano, T. 2000, *ApJ*, 543, 486
- Schlaufman, K. C., Lin, D. N. C., & Ida, S. 2009, *ApJ*, 691, 1322
- Schlichting, H. E., Fuentes, C. I., & Trilling, D. E. 2013, *AJ*, 146, 36
- Schlichting, H. E., Ofek, E. O., Sari, R., et al. 2012, *ApJ*, 761, 150
- Schlichting, H. E. & Sari, R. 2011, *ApJ*, 728, 68
- Schräpler, R., Blum, J., Seizinger, A., & Kley, W. 2012, *ApJ*, 758, 35
- Seizinger, A. & Kley, W. 2013, *A&A*, 551, A65
- Shakura, N. I. & Sunyaev, R. A. 1973, *A&A*, 24, 337
- Silk, J. & Takahashi, T. 1979, *ApJ*, 229, 242
- Sirono, S.-i. 2011, *ApJ*, 735, 131
- Skorov, Y. & Blum, J. 2012, *Icarus*, 221, 1
- Smoluchowski, M. V. 1916, *Zeitschrift fur Physik*, 17, 557
- Spaute, D., Weidenschilling, S. J., Davis, D. R., & Marzari, F. 1991, *Icarus*, 92, 147
- Stammler, S. M. & Dullemond, C. P. 2014, *Icarus*, 242, 1
- Suyama, T., Wada, K., Tanaka, H., & Okuzumi, S. 2012, *ApJ*, 753, 115
- Takeuchi, T. & Ida, S. 2012, *ApJ*, 749, 89
- Takeuchi, T., Muto, T., Okuzumi, S., Ishitsu, N., & Ida, S. 2012, *ApJ*, 744, 101
- Tanaka, H., Himeno, Y., & Ida, S. 2005, *ApJ*, 625, 414
- Tanaka, H., Takeuchi, T., & Ward, W. R. 2002, *ApJ*, 565, 1257
- Tegler, S. C. & Romanishin, W. 1998, *Nature*, 392, 49
- Tegler, S. C. & Romanishin, W. 2003, *Icarus*, 161, 181
- Teiser, J. & Wurm, G. 2009, *MNRAS*, 393, 1584
- Tera, F., Papanastassiou, D. A., & Wasserburg, G. J. 1973, in Lunar and Planetary Science Conference, Vol. 4, Lunar and Planetary Science Conference, 723
- Terquem, C. & Papaloizou, J. C. B. 2007, *ApJ*, 654, 1110
- Thébault, P., Marzari, F., & Scholl, H. 2006, *Icarus*, 183, 193

BIBLIOGRAPHY

- Tilley, D. A., Balsara, D. S., Brittain, S. D., & Rettig, T. 2010, *MNRAS*, 403, 211
- Triaud, A. H. M. J., Collier Cameron, A., Queloz, D., et al. 2010, *A&A*, 524, A25
- Tsiganis, K., Gomes, R., Morbidelli, A., & Levison, H. F. 2005, *Nature*, 435, 459
- Turner, N. J., Sano, T., & Dziourkevitch, N. 2007, *ApJ*, 659, 729
- Uribe, A. L., Klahr, H., Flock, M., & Henning, T. 2011, *ApJ*, 736, 85
- Wada, K., Tanaka, H., Okuzumi, S., et al. 2013, *A&A*, 559, A62
- Wada, K., Tanaka, H., Suyama, T., Kimura, H., & Yamamoto, T. 2007, *ApJ*, 661, 320
- Wada, K., Tanaka, H., Suyama, T., Kimura, H., & Yamamoto, T. 2009, *ApJ*, 702, 1490
- Wada, K., Tanaka, H., Suyama, T., Kimura, H., & Yamamoto, T. 2011, *ApJ*, 737, 36
- Walsh, K. J., Morbidelli, A., Raymond, S. N., O'Brien, D. P., & Mandell, A. M. 2011, *Nature*, 475, 206
- Weidenschilling, S. J. 1977a, *MNRAS*, 180, 57
- Weidenschilling, S. J. 1977b, *Ap&SS*, 51, 153
- Weidenschilling, S. J. 1980, *Icarus*, 44, 172
- Weidenschilling, S. J. 1995, *Icarus*, 116, 433
- Weidenschilling, S. J. 2011, *Icarus*, 214, 671
- Weidling, R., Güttler, C., & Blum, J. 2012, *Icarus*, 218, 688
- Weidling, R., Güttler, C., Blum, J., & Brauer, F. 2009, *ApJ*, 696, 2036
- Welsh, W. F., Orosz, J. A., Carter, J. A., et al. 2012, *Nature*, 481, 475
- Wetherill, G. W. 1975, in Lunar and Planetary Science Conference Proceedings, Vol. 6, Lunar and Planetary Science Conference Proceedings, 1539–1561
- Wetherill, G. W. 1990, *Icarus*, 88, 336
- Wetherill, G. W. & Stewart, G. R. 1989, *Icarus*, 77, 330
- Whipple, F. L. 1972, in From Plasma to Planet, ed. A. Elvius, 211
- Williams, J. P. & Cieza, L. A. 2011, *ARA&A*, 49, 67
- Windmark, F., Birnstiel, T., Güttler, C., et al. 2012a, *A&A*, 540, A73
- Windmark, F., Birnstiel, T., Ormel, C. W., & Dullemond, C. P. 2012b, *A&A*, 544, L16
- Windmark, F., Birnstiel, T., Ormel, C. W., & Dullemond, C. P. 2012c, *A&A*, 548, C1
- Wolszczan, A. & Frail, D. A. 1992, *Nature*, 355, 145

BIBLIOGRAPHY

- Wurm, G. & Blum, J. 1998, *Icarus*, 132, 125
- Wurm, G., Paraskov, G., & Krauss, O. 2005, *Icarus*, 178, 253
- Wyatt, M. C. 2008, *ARA&A*, 46, 339
- Xie, J.-W., Payne, M. J., Thébault, P., Zhou, J.-L., & Ge, J. 2010, *ApJ*, 724, 1153
- Yamamoto, T., Kozasa, T., Honda, R., & Mizutani, H. 1991, in Lunar and Planetary Inst. Technical Report, Vol. 22, Lunar and Planetary Science Conference, 1533
- Yang, C.-C. & Johansen, A. 2014, *ApJ*, 792, 86
- Yang, C.-C. & Menou, K. 2010, *MNRAS*, 402, 2436
- Youdin, A. & Johansen, A. 2007, *ApJ*, 662, 613
- Youdin, A. N. 2011a, *ApJ*, 731, 99
- Youdin, A. N. 2011b, *ApJ*, 742, 38
- Youdin, A. N. & Chiang, E. I. 2004, *ApJ*, 601, 1109
- Youdin, A. N. & Goodman, J. 2005, *ApJ*, 620, 459
- Youdin, A. N. & Lithwick, Y. 2007, *Icarus*, 192, 588
- Youdin, A. N. & Shu, F. H. 2002, *ApJ*, 580, 494
- Zsom, A. & Dullemond, C. P. 2008, *A&A*, 489, 931
- Zsom, A., Ormel, C. W., Dullemond, C. P., & Henning, T. 2011a, *A&A*, 534, A73
- Zsom, A., Ormel, C. W., Güttler, C., Blum, J., & Dullemond, C. P. 2010, *A&A*, 513, A57
- Zsom, A., Sándor, Z., & Dullemond, C. P. 2011b, *A&A*, 527, A10
- Zuckerman, B., Fekel, F. C., Williamson, M. H., Henry, G. W., & Munro, M. P. 2008, *ApJ*, 688, 1345

ACKNOWLEDGMENTS

First of all, I would like to thank my supervisor, Kees Dullemond, for giving me the opportunity to enter the PhD program in such a great, lively center as Heidelberg, and for supporting me throughout the 3 years. It is very hard to quantify the knowledge and experience that I have acquired during this time and I am pretty sure it is more than written up in this dissertation.

I would like to thank my collaborator and group mate, Fredrik Windmark, for joining my projects and sharing his work and expertise with me. Without him, it would be much harder to accomplish this dissertation.

I would also like to thank my IMPRS thesis committee with Kees, Ralf Klessen, and Thomas Henning for their support, as well as my examination committee, with Kees, Thomas, Eva Grebel, and Mario Trieloff, who kindly agreed to referee this work, for their time.

It has been a great experience to be a member of the IMPRS-HD and thus I would like to thank the IMPRS coordinator, Christian Fendt, as well as all the 7th generation of IMPRS-HD students for building such a great atmosphere.

Thanks to all my group: Fredrik, Paola, Sebastian S., Jon, Volker, Laszlo, Sareh, Adriana, Sebastian L., Carsten, and Eduard for all the time spent together and discussion we have had. I would also like to thank my office mates: Paola, Faviola, Gustavo, Lukas, Jenny, Christian, Jayanta, and Juan, and the coffee team with Jon, Rahul, Sebastian, Laszlo, Mei, Volker, and Dan, as well as all the other people at ITA for creating a positive work environment. Particularly, I would like to thank Sebastian and Jenny for translating the dissertation abstract to German and Dan for correcting the English version.

To all the great people that I meet during the 3 years, particularly Satoshi Okuzumi, Carsten Dominik, Andras Zsom, Chris Ormel, Til Birnstiel, Anders Johansen, Xuening Bai, Melvyn Davies, and Ben Moore – thank you for the discussions and giving me faith in what I am doing.

I would like to take the opportunity to thank my parents for their support. Thanks to them, I had an interest in science since my early years and without them I couldn't be where I am now.

Last, but not least, I thank my beloved husband, Wieńczysław, for being with me, for his constant support in every aspect of my life, for organizing our free time, and being willing to adapt to whatever the life bring next.